VARIABILITY OF THE ATLANTIC MERIDIONAL OVERTURNING CIRCULATION AND ITS IMPACT ON THE WEST AFRICAN MONSOON DURING THE LAST GLACIAL CYCLE

A Dissertation

by

ANDREW O. PARKER

Submitted to the Office of Graduate and Professional Studies of
Texas A&M University
in partial fulfillment of the requirements for the degree of

DOCTOR OF PHILOSOPHY

Chair of Committee,	Matthew W. Schmidt
Committee Members,	Ping Chang
	Niall C. Slowey
	Franco Marcantonio
	Brendan Roark
Head of Department,	Deborah J. Thomas

May 2016

Major Subject: Oceanography

ABSTRACT

The Atlantic Meridional Overturning Circulation is an important feature of Earth's climate system that regulates hemispheric heat distribution. This dissertation takes an in-depth look at how the strength of this circulation changed during the course of the last ice age and explores the effects these variations had on Tropical Atlantic climate variability.

First, variability of AMOC during abrupt glacial climate events called Dansgaard-Oeschger Events (DO) is investigated. Using an established relationship between AMOC slowdown and a warming of subsurface waters across the tropical North Atlantic, a Mg/Ca-based temperature record reconstructed from the deep-dwelling foraminifera *Globorotalia truncatulinoides* is used to reconstruct subsurface temperatures in the southern Caribbean sea. This record reveals that during the cold phases of most Dansgaard-Oeschger Events, the subsurface of the Caribbean warmed in a manner consistent with a reduced AMOC during this time.

Then, the variability of the West African Monsoon (WAM) system during Heinrich Event 1 (H1) and the Younger Dryas (YD), periods of know AMOC reductions that occurred during the deglacial, is studied. Using the surface-dwelling foraminifera *Globigerinoides ruber*, Ba/Ca ratios were measured to reconstruct the deglacial discharge history of the Niger River. Ba/Ca ratios do not point to increased drought-like conditions during either the H1 or YD as suggested by previous studies based on Saharan dust accumulation records. Instead, the Ba/Ca ratios gradually increase after H1,

reaching peak runoff conditions during the early Holocene. This gradual evolution of monsoonal rainfall across West Africa supports recent observations suggesting that deglacial reconstructions of dust from West Africa reflect changes in wind-strength rather than changes in aridity.

Modeling studies suggest that the subsurface around the Niger Delta is particularly sensitive to subsurface warming when AMOC slows. Thus, the deep-dwelling foraminifera *Globorotalia crassaformis* is used to reconstruct subsurface temperatures around the Niger Delta to compare with the deglacial Ba/Ca record of Niger River runoff from the same site. During H1 and the YD, the new Niger Delta subsurface temperature record suggests significant subsurface warming. These events are consistent with high-resolution model simulations that identify a strong negative correlation between AMOC strength and subsurface temperature around the Niger Delta. This subsurface warming may have reduced the land-sea thermal gradient, which is critical to monsoon development and significantly affected the strength of the monsoon during each event.

To my family

ACKNOWLEDGEMENTS

I would like to thank, above all, my advisor Dr. Matthew Schmidt for supporting me in every aspect of my dissertation. He always had great advice and never steered me in the wrong direction. I truly look up to him as a mentor and scientist. He is the standard to which I will always aim to achieve in my career.

I am also grateful to my committee member, Dr. Ping Chang, Dr. Niall Slowey, Dr. Franco Marcantonio and Dr. Brendan Roark, for their input and encouragement over the last five years. I am a better scientist and person because of it.

To my wife Megan, the words thank you does not do justice to the amount of love and patience you gave me during our years in College Station. You and me together, we can do anything. I can't wait for the next adventure life has in store for us.

Many, many thanks go out to my lab mate Jennifer Hertzberg, whose passion for Paleoceanography is contagious. You were a great friend throughout the years. I thoroughly enjoyed my discussions with Mitch Lyle and Zane Jobe. And Luz Romero spent countless hours maintaining the ICP-MS so I could make timely, quality measurements. I'd be lost without her assistance.

Many thanks to everyone in the Department of Oceanography, in particular, Wilf Gardner and Mary Jo Richardson whose NSF-STEM funding allowed me to spend my summers focused solely on research.

A final thank you goes out to my family, who from an early age instilled in me the importance of life-long learning and encouraged me to pursue my dreams.

Specific acknowledgements for Chapter II: This work was supported by a National Science foundation grant to M.W.S. and P.C (OCE-1102743). We thank Luz Romero for technical assistance with the ICP-MS and two undergraduate lab assistants for help with lab work. We also thank the Lamont Doherty Earth Observatory core repository for their sampling of sediment core material. A.O.P. was also supported by a National Science Foundation S-STEM grant. Reviews by two anonymous reviewers significantly improved this manuscript.

Specific acknowledgments for Chapter III: We thank L. Romero for assistance with geochemical analyses and lab instruments. We also thank S.E. Nicholson (Florida State) for useful discussions on West African meteorology. This work was funded by a National Science Foundation grant to M.W.S. (OCE-1102743) and Shell International Exploration and Production, Inc.

Specific acknowledgements for Chapter IV: We thank Mitch Lyle for proving $CaCO_3$ analyses and many useful discussions helping to calibrate the XRF data. Shell International Exploration and Production provided core material and supplemental funding of analyses. A.O.P. also acknowledges funding from an NSF-STEM scholarship. This work was funded by a National Science Foundation grant to M.W.S. (OCE-1102743) and Shell International Exploration and Production, Inc.

TABLE OF CONTENTS

LIST OF FIGURES

Page

LIST OF TABLES

CHAPTER I

INTRODUCTION

The oceans cover 71% of Earth's surface; so it is not surprising that they play a fundamental role in the climate system [*Rahmstorf*, 2002]. Incoming solar radiation is absorbed by surface waters and quickly redistributed throughout the globe by a complex network of ocean currents called the "Global Ocean Conveyer" [*Broecker et al*. 1991]. Arguably, the most important component of this system is the Atlantic Meridional Overturning Circulation, or AMOC. The AMOC consists of a series of warm surface currents that originate in the South Atlantic, eventually crossing the equator to form the Gulfstream. As Gulfstream waters flow north they cool, releasing large quantities of heat to the atmosphere prior to sinking and flowing back south at depth. The total inter-hemispheric northward heat transport by AMOC is around 1.2 PW (1 PW equals 10^{15} watts) [*Clark et al*. 2002], allowing locations across Europe and Scandinavia to remain relatively warm in spite of their high-latitude location. Thus, any change in the strength of AMOC is thought to have severe consequences for global climate.

The primary driver of AMOC involves the formation of deep-water masses in areas around the Labrador and Greenland Seas of the North Atlantic [*Kuhlbrodt et al*. 2007]. As the Gulfstream travels through the Western Atlantic it picks up high salinity waters and advects them north. On their northward transit these Gulfstream waters cool, and the combination of high salt content and cold temperature causes the water to

increase density. In isolated regions around Greenland where cooling is strongest (mainly the Labrador and Greenland Seas), water density becomes so great that the surface waters sink, forming a deep-water mass that flows back toward the south at depth. If the surface buoyancy of North Atlantic waters is reduced in any way, deep-water formation can be easily disrupted [*Clark et al*. 2001; *Clark et al.* 2002]. In light of recent observations that indicate increasing global temperatures are accelerating the melting of the Greenland Ice Sheet, it is important to understand how AMOC responded to various climate forcings in the past, in order to better constrain how it will behave in the future.

Beyond the very short period of modern instrumental observations, scientists rely on "proxies" to reconstruct past AMOC variability. Many proxy reconstructions involve the use of foraminifera, unicellular zooplankton that secrete a calcium carbonate ($CaCO_3$) shell. It was quickly realized that the chemistry of foraminiferal $CaCO_3$ reflects the water properties in which that organism grew, and could provide important information on oceanographic parameters related to AMOC [*Emiliani*, 1954]. Since then, numerous foraminiferal geochemical proxies have been developed. Perhaps one of the most important and widely used proxy is the Mg/Ca paleothermometer. The substitution of Mg^{2+} for Ca^{2+} in foraminiferal calcite is endothermic and thus, is favored at higher temperatures. Therefore, the measured Mg/Ca ratio in foraminiferal calcite should increase with increasing temperature [*Barker et al*. 2005]. Calibration equations relating the Mg/Ca ratios in foraminiferal calcite to seawater temperature have been derived using a number of methods including core-top, sediment trap and culturing

calibrations [*Anand et al*., 2003, *Dekens et al*., 2002*; Lea et al.,* 1999, *Lea et al*., 2000, *Regenberg et al*. , 2009]. Although subtle differences exist between calibration methods, these studies conclude that temperature exerts the primary control on shell Mg/Ca with most planktonic foraminifera exhibiting a temperature sensitivity of ~9% change in Mg/Ca per decree Celsius [*Anand et al*. 2003, *Dekens et al*. 2002; *Honisch et al.* 2013].

The most studied period of AMOC variability is that of the last deglacial, a period of time between 10-20 kyr in which continental ice sheets began to retreat from their glacial maximum in response to changing orbital parameters [*Denton et al*. 2010]. During this time, reconstructions have identified two major climate events that were characterized by a weakened AMOC [*Clark et al.* 2012]. The first event, Heinrich Event 1 (H1), occurred shortly after deglaciation began and was initially identified as a layer of coarse-grained deposits in sediment cores recovered from the open Atlantic [*Heinrich*, 1988]. This layer of ice-rafted debris (IRD) is the result of a sudden collapse of the Greenland ice sheet which sent iceberg armadas flowing into the North Atlantic where they eventually melted, freshening the waters enough to reduce deep water formation [*Bond et al*. 1992; *Broecker et al*. 1992]. In total, seven IRD deposits have been identified in North Atlantic sediments for the last glacial cycle, although not every layer can be definitively linked with a weakening of AMOC [*Bond et al.* 1992; *Hemming*, 2004]. In the case of H1, ample proxy evidence confidently associates this event with a significant reduction in AMOC strength [*Gherardi et al*. 2009; *Lynch-Stieglitz et al*. 2014; *McManus et al*. 2004], which surprisingly occurred in as little as a few centuries and lasted up to 2 kyr. The climate impacts during H1 were felt globally [*Broecker and*

Hemming, 2001], and included stronger trade winds throughout the tropics [*McIntyre and Molfino*, 1996] and dramatic changes to the global hydrologic cycle [*Leduc et al*. 2009; *Peterson et al*. 2000; *Wang et al*. 2001].

The second deglacial event associated with a weakened AMOC is the Younger Dryas (YD), which occurred between 11.2 and 12.9 kyr. Prior to this event, significant deglacial warming promoted substantial melting of the North American ice sheet, which collected across the upper Midwest and southern Canada to form glacial Lake Agassiz [*Teller and Clayton*, 1983]. Around 13 kyr, a large portion of the lake abruptly drained into the North Atlantic causing a significant freshening of North Atlantic salinities and a rapid disruption of deep-water formation [*Broecker et al*. 1998; *Condron et al.* 2012; *Peltier et al*. 2006; *Tarasov and Peltier*, 2005; *Teller et al*. 2002]. Based on proxy evidence, the magnitude of AMOC weakening during the YD was comparable to HI, although it is difficult to completely access due to the short and abrupt nature of the event [*Gherardi et al*. 2009; *Lynch-Stieglitz et al*. 2011; *McManus et al*. 2004]. Also, the YD occurred during a time when climate had significantly warmed relative to glacial maximum conditions, and thus the impacts on climate were equally as dramatic. During the YD a return to cold conditions is recorded in climate reconstructions from both high and low latitude Northern Hemisphere locations [*Anderson et al*. 2004]. Changes in the hydrologic cycle across South America, Africa and Asia, have also been documented during the YD [*Bard et al*. 2000; *Kanner et al*. 2012; *Partin et al*. 2007; *Wang et al*. 2004; *Weldeab et al*. 2007], providing ample evidence that AMOC plays a principal role in past climate variability.

Moving slightly farther back in time to the peak of the last glacial period between 20-80 kyr, the role of AMOC is far less certain. During this time, high frequency climate events called Dansgaard-Oscheger Events (DO) punctuate Greenland ice core records. These events are characterized by abrupt 8-16^{o}C warming of air temperatures over Greenland followed by a gradual cooling [*Dansgaard et al*. 1993]. Recent studies have suggested that destabilization of ice shelves in the Labrador and Nordic seas sent mini-iceberg armadas into the North Atlantic interfering with deep-water formation [*Alverez-Solas et al.* 2013; *Dokken et al*. 2013*; Menviel et al*. 2014; *Peterson et al*. 2013; *Zhang et al*. 2015]. AMOC has long been thought to play a role in this process, but the quick nature of these events has made it difficult to resolve DO events in many marine sediment cores. Therefore, only sparse paleoceanographic evidence exists supporting the link between DO events and AMOC changes.

The study in Chapter II of this dissertation uses an established relationship between subsurface temperatures in the tropical North Atlantic (TNA) and AMOC strength to reconstruct a record of AMOC variability during the last glacial using a high sedimentation rate core from the Bonaire Basin of the southern Caribbean. Based on water hosing experiments, *Zhang et al*. [2007] showed that the subsurface of the TNA warms when AMOC is weakened. The reason for this relationship is two-fold [*Chang et al*. 2008; *Schmidt et al*. 2012]. First, weakening of AMOC reduces the strength of the western boundary current. This causes a warming of the subsurface due to the reduced transport of cooler waters into the TNA. Then, after AMOC weakened beyond a threshold, the equatorward pathway of the North Atlantic subtropical cell opens,

allowing the salinity maximum waters of the subtropical North Atlantic gyre to flow south into the equatorial zone causing the subsurface to warm [*Fratanntoni et al*. 2000; *Hazeleger and Drifhout*, 2006; *Jochum and Malanotte-Rizzoli*, 2001; *Kirchner et al*. 2009]. To reconstruct past changes in subsurface temperature, the Mg/Ca ratios in a subsurface dwelling species of planktonic foraminifera were analyzed. At higher temperatures, Mg^{2+} substitutes into the calcium carbonate for Ca^{2+}, and thus the measured Mg/Ca ratios in a foraminifera's shell can be converted to temperature using empirical relationships derived from numerous culturing and core-top calibration studies [*Anand et al*. 2003; *Lea et al*. 1999; *Nurnberg et al*. 1996]. If AMOC weakened during DO events, the foraminiferal Mg/Ca temperatures should record strong subsurface warming recorded during the cold phase of a DO event.

In Chapter III, the effects of a reduced AMOC during H1 and the YD on West African climate are reevaluated. Previous reconstructions of West Africa hydroclimate suggested that the West African Monsoon (WAM) system collapsed during H1, leading to widespread drought throughout the region. This observation is reflected in reconstructions of dust export and grain size analysis from the Senegalese and Mauritanian coasts [*Collins et al*. 2013; *Itambi et al*. 2009; *Multiza et al*. 2008; *Tjallingii et al*. 2008]. Nevertheless, paleoceanographic evidence from the Gulf of Guinea suggests otherwise. Here, the only high-resolution study in the region reconstructed sea surface salinity and river discharge, believed to be controlled by the intensity of WAM precipitation, and showed no weakening in monsoon strength during H1 [*Weldeab et al*. 2007]. There are two possible explanations for the discrepancy. First, the location of the

core used in the Gulf of Guinea study may lie in an area that is influenced by precipitation falling across Equatorial Africa, not West Africa. Secondly, recent observations have shown that changes in wind strength can produce significant dust emissions independent of changes in continental aridity [*Ridely et al*. 2014; *Rodriguez et al*. 2015], casting considerable uncertainty when interpreting these records [*McGee et al*. 2010].

This chapter addresses both possibilities by generating new records of salinity and river discharge from a core located at the mouth of the Niger River in the western Gulf of Guinea. The core location is ideal for reconstructing changes in monsoon strength because the magnitude of Niger River discharge is directly related to the strength of WAM precipitation that falls across the river basin to the north. In order to reconstruct Niger River discharge, Ba/Ca ratios in planktonic foraminifera are evaluated. Ba^{2+} concentrations are enriched in freshwater, and conservatively mix with seawater to produce a linear inverse relationship. Ba^{2+} incorporation into the foraminiferal shell is linearly dependent on Ba^{2+} concentrations in the water making it a useful proxy to reconstruct river discharge [*Coffey* et al. 1997; *Honisch et al.* 2011. Foraminiferal $\delta^{18}O_c$ was also measured, which reflects the temperature and $\delta^{18}O_{seawater}$ ($\delta^{18}O_{sw}$) in which the organism grew. The $\delta^{18}O_{sw}$ component can be isolated by removing the temperature component with the Mg/Ca derived SST [*Bemis et al.* 1998], and because $\delta^{18}O_{sw}$ varies linearly with sea-surface salinity (SSS) it can be used to estimate past changes in SSS [*Charles and Fairbanks*, 1990]. These new records reveal that Niger River discharge and SSS remained low during the first half of the deglacial and only gradually began to

reflect wetter conditions at the start of the African Humid Period 14.8 kyr ago. When compared to previous studies from the region it, it is evident that the evolution of the West and Equatorial African monsoon systems where decoupled during the last deglaciation because the West African monsoon was stymied by low Northern Hemisphere summertime insolation. The lack of evidence for increased aridity across West Africa during H1 suggests that wind strength likely played a primary role in forcing dust emissions from this region, not drought.

Chapter IV aims to evaluate the direct relationship between WAM variability and subsurface temperature changes during the deglacial period. In describing the subsurface warming mechanism introduced in Chapter II, *Chang et al*. [2008] theorized that once the subsurface warming entered the equatorial zone, in would become entrained in the upwelling of the Eastern Equatorial Atlantic (EEA) cold tongue. The warming this would have on sea surface temperatures in the EEA would reduced the land-sea thermal gradient that is critical for monsoon development and lead to a reduction in WAM strength. Recent modeling studies showed that there is a high correlation between AMOC strength and EEA subsurface temperatures, including around the Niger Delta. Therefore, subsurface temperatures were reconstructed in the Niger Delta core from Chapter III. As the reconstructions were produced from the same core, this allows for direct comparison between the records of WAM and AMOC strength. When an existing WAM record from the Guinea Coast is included in the interpretation of Niger River records [*Shannahan et al*. 2015], a latitudinal perspective of WAM evolution during the deglacial is produced. The pattern of variability observed with respect to the generated

temperature records is then easily explained by the modern mechanics of the present day WAM system.

To summarize, the layout of this dissertation is as follows:

- Chapter II investigates AMOC variability using a high-resolution core from the Bonaire Basin in the southern Caribbean Sea. Foraminiferal Mg/Ca is measured to reconstruct a record of subsurface temperature variability, which is closely linked to AMOC in this region.
- Chapter III takes an in depth look at the evolution of hydroclimate across West and Central Africa during the AMOC slowdown events of H1 and the YD. Foraminiferal Ba/Ca and calculated IVF-$^{18}O_{sw}$ are used to reconstruct Niger River discharge and Niger Delta sea surface salinity, respectively.
- Chapter IV examines the direct relationship between AMOC and West African Monsoon strength. Subsurface temperatures during the deglacial are reconstructed using foraminifera Mg/Ca and compared with records of monsoon strength introduced in chapter III.
- Chapter V concludes this dissertation with a summary of the major findings in Chapters II-IV.

CHAPTER II

TROPICAL NORTH ATLANTIC SUBSURFACE WARMING EVENTS AS A FINGERPRINT FOR AMOC VARIABILITY DURING MARINE ISOTOPE STAGE 3*

II.1. Introduction

Understanding the role of Atlantic Meridional Overturning Circulation (AMOC) in abrupt climate change during the last glacial cycle has become a fundamental topic in Paleoceanography. Evidence suggests that a reduction of AMOC during the last deglacial played an important role in two large and abrupt cooling events on the long-term warming trend following the end of the last glacial period. These two cold periods in the North Atlantic, known as Heinrich Event 1 and the Younger Dryas, likely involved changes in the density of North Atlantic water due to increasing ice sheet melting [*Bond et al.*, 1999; *Clark et al.*, 2001; *Menviel et al.*, 2011; *Ritz et al.*, 2013]. Although internal feedbacks within the climate system may initiate cold stadials [*Barker et al.,* 2015], the reduced surface buoyancy of North Atlantic waters due to the flux of icebergs likely slowed the rate of deep-water formation resulting in a slowdown of AMOC and reduced northward oceanic heat transport. Considerable evidence from a

*Reprinted from *Paleoceanography* , 30, Andrew O. Parker, Matthew W. Schmidt and Ping Chang, Tropical North Atlantic subsurface warming events as a fingerprint for AMOC variability during Marine Isotope Stage 3, 2015, doi:10.1002/2015PA002832, with permission from Wiley.

number of proxies including radiocarbon, nutrient tracers and $^{231}Pa/^{230}Th$ support the hypothesis of a reduced AMOC during these deglacial reversals [*Curry and Oppo*, 2005; *McManus et al.*, 2004]. However, our understanding of the extent to which AMOC fluctuated during the glacial period across the abrupt Dansgaard-Oeschger (DO) events of Marine Isotope Stage 3 (MIS 3, 29-59 kyr) remains uncertain.

The idea that AMOC variability could be related to DO events has long been established [*Broecker et al.*, 1990; *Rahmstorf*, 2002; *Timmermann et al.*, 2003; *Zhang et al.*, 2015], but evidence remains limited by a lack of sufficient data from marine sediment archives. High-resolution records from MIS 3 can be a challenge to find and particularly difficult to date as the limits of radiocarbon are reached at ~40 kyr and other means of constructing absolute age models in marine sediment cores are rare.. Early studies successfully linked DO-like variability in Atlantic sediments to fluctuations in AMOC with varying success. For example, *Charles et al.* [1996] produced high-resolution isotope records from benthic foraminifera in the Southern Ocean to demonstrate a clear millennial scale pattern of change in Circumpolar Deep Water during the last glacial. This observation was later confirmed in the same core by *Piotrowski et al*. [2005] using Nd isotopes to track changes in northern vs. southern source waters in the Southern Ocean during MIS 3 and the last deglacial. Furthermore, *Keigwin and Boyle* [1999] measured $\delta^{13}C$ values of benthic foraminifera from a deep sediment core on the Bermuda Rise and found comparable changes in deep water formation during MIS 3. Using similar methods, *Elliot et al.* [2002] also showed changes in benthic foraminiferal $\delta^{13}C$ values corresponding to DO stadials, and *Vautravers et al.*

[2004] found millennial-scale variability of deep-water $\delta^{13}C$ from the Blake Ridge, albeit only during some DO stadials. Other methods including sediment magnetic susceptibility and trace metals have also traced DO-like variability in Atlantic sediments to deep ocean circulation. A benthic foraminiferal Mg/Ca record from the Iberian Margin published by *Skinner and Elderfield* [2007] showed a correlation between deep-water temperature change and Greenland climate during MIS 3. Recently, this warming has been hypothesized to have played a key role in ice sheet destabilization during MIS 3, allowing for minor perturbations arising from sea ice - ice sheet - ocean interactions to significantly affect AMOC [*Alvarez-Solas et al.*, 2013; *Dokken et al.*, 2013; *Marcott et al.*, 2011]. Furthermore, few proxies have the ability to directly monitor changes in AMOC strength. Kinematic proxies like sediment $^{231}Pa/^{230}Th$ ratios track the export of ^{231}Pa relative to ^{230}Th from the Atlantic as a proxy for deep-water export [*McManus et al.*, 2004], and nutrient proxies such as Cd/Ca and $\delta^{13}C$ measured in benthic foraminifera can be used to reconstruct changes in Atlantic water mass geometry associated with differing AMOC states [*Curry and Oppo*, 2005]. Yet, in spite of these recent advances, there is still only limited paleoceanographic evidence supporting a relationship between DO events and AMOC variability [*Clement and Peterson*, 2008].

In this study, we reconstruct past subsurface temperature changes in the Western Boundary Current in the Tropical North Atlantic (TNA) as a new proxy for AMOC variability during MIS 3. *Zhang* [2007] established the relationship between TNA subsurface warming and AMOC weakening based on water hosing experiments, and then used observed TNA subsurface anomalies to infer AMOC variations over the last

several decades. *Chang et al.* [2008] and *Schmidt et al.* [2012b] extended the investigation of the subsurface temperature response to AMOC changes by including the equatorial and south tropical Atlantic and identified a two-step ocean teleconnection mechanism linking the subsurface warming to a weakening in AMOC. The first step process primarily involves oceanic adjustment in response to the AMOC change, which causes a rapid weakening in the western boundary current, resulting in a subsurface warming in the TNA by reducing the transport of the cold and fresh subsurface tropical water into the Caribbean region. The second step process becomes effective when AMOC weakens beyond a threshold, at which the equatorward pathway of the North Atlantic subtropical cell opens, allowing the warm salinity maximum waters (SMW) of the subtropical North Atlantic gyre to flow south and warm the subsurface of the equatorial zone, causing warming the equatorial and south tropical Atlantic. Today, the warm salinity maximum waters (SMW) of the subtropical North Atlantic gyre remain separated from the cooler, fresher tropical subsurface waters because the equatorward pathway of the North Atlantic subtropical cell is blocked by the strong northward return flow of AMOC along the western boundary (Figure 2.1) [*Fratantoni et al.*, 2000; *Hazeleger and Drijfhout*, 2006; *Jochum and Malanotte-Rizzoli*, 2001; *Kirchner et al.*, 2009]. Modeling results in *Schmidt et al.* [2012b] showed that a major reduction in AMOC under Last Glacial Maximum (LGM) forcings and boundary conditions can produce a strong subsurface warming in the western TNA and equatorial Atlantic, providing evidence this mechanism could have operated under glacial conditions. *Schmidt et al.* [2012b] also analyzed Mg/Ca ratios in the subthermocline dwelling

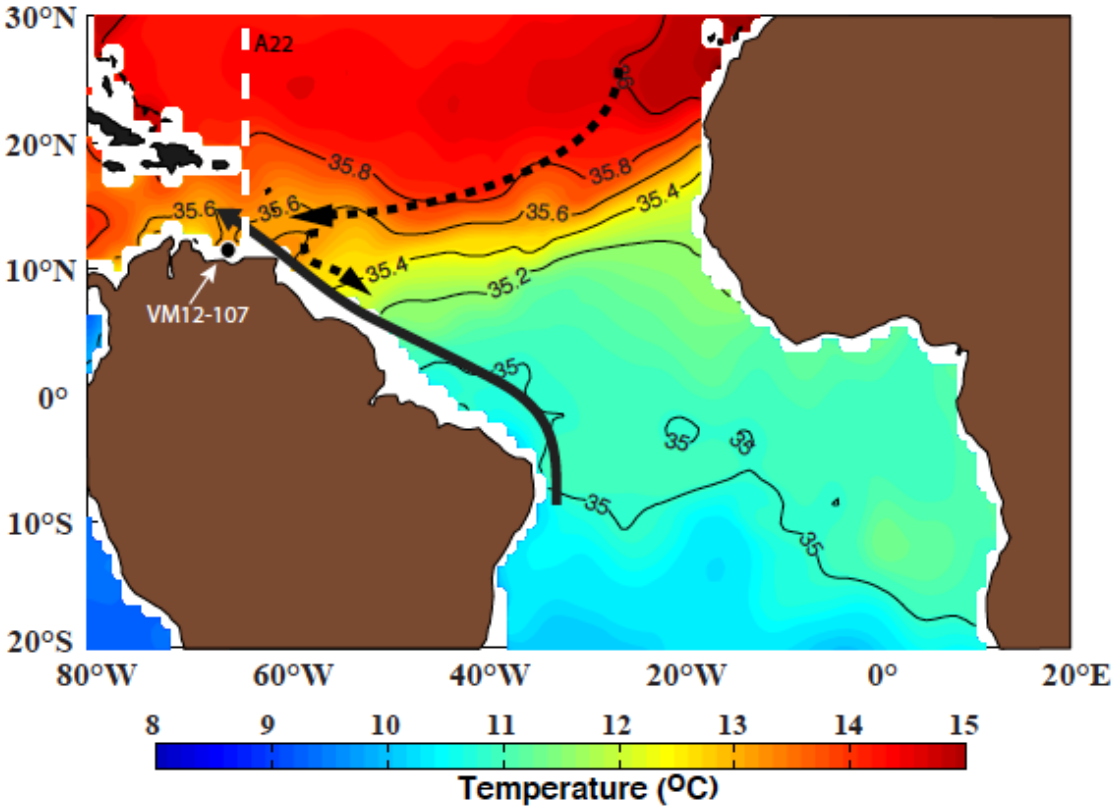

Figure 2.1 Hydrography of the Tropical Atlantic. Modern subsurface hydrography across the Tropical Atlantic along the density surface σ=1026.8 (~200-600 m depth). A sharp temperature (color) and salinity (contours) gradient exists in the subsurface between the subtropical gyre and the deep tropics. The warm subtropical gyre waters are blocked from flowing into the deep tropics by the northward return flow in the upper limb of the modern AMOC cell (North Brazil Current). Competition between this equatorward flow and northward AMOC return is a key element of the subsurface warming mechanism. White dashed line is cross section from WOCE line A22 in figure 2.

planktonic foraminifera *Globorotalia crassaformis* in core VM12-107 from the southern Caribbean to reconstruct a record of deglacial subsurface temperature change (see Figure 2.1 for core location). Their results showed significant subsurface warming at the start of the Younger Dryas and Heinrich Event 1 that covaried with changes in AMOC variability across the deglacial, demonstrating a link between AMOC weakening and subsurface warming in the TNA, likely through the first step of the proposed mechanism.

Here, we extend the record from core VM12-107 (11.33^{o}N, 66.63^{o}W, 1079m) from the Bonaire Basin in the Southern Caribbean to reconstruct high-resolution (90yr/sample) records of surface and subsurface temperature and $\delta^{18}O_{seawater}$ ($\delta^{18}O_{sw}$, a proxy for salinity) to determine if similar subsurface temperature variability is observed during the DO events of MIS 2 and 3 (22-52 kyr). We use the upper-mixed layer planktonic foraminifera *Globigerinoides ruber* to reconstruct near-surface conditions and the subthermocline dwelling planktonic foraminifera *Globorotalia truncatulinoides* to reconstruct temperature at intermediate depths (~200-400 m depth range). Our results show subsurface warming accompanies the transition from interstadial to stadial conditions during most DO events across this interval, suggesting AMOC did weaken during DO stadials.

II.2. Oceanographic Setting

VM12-107 (11.33^{o}N, 66.63^{o}W, 1079m) is located in the Bonaire Basin, just northwest of the Cariaco Basin in the Southern Caribbean Sea. The site lies in a region of seasonal coastal upwelling initiated by the seasonal migration of the Intertropical

Convergence Zone (ITCZ) from 15°N to 5°S [*Haug et al.*, 2001]. The mean annual SST at our site is 26.7°C. During January-March when the ITCZ is at its southern most position, northeast trade winds initiate a strong coastal upwelling cell, resulting in cooler SSTs of ~25.5°C [*Antonov et al.*, 2010]. SSTs peaks from June-September, reaching 27.2°C as the ITCZ migrates to just north of the Bonaire Basin. In this region, the ITCZ is the primary control of seasonal rainfalls and thus, when the ITCZ is at its southern most position during boreal winter, salinity peaks to ~36.7 and decreases to ~36.3 during summer when the ITCZ is located at its northern most position [*Antonov et al.*, 2010; *Haug et al.*, 2001; *Peterson et al.*, 2000].

In the subsurface, the SMW of the Caribbean are separated from the cooler and fresher subsurface waters of the Bonaire Basin. The SMW can be defined as a water mass in the open Caribbean centered between 150-300 m with an annual temperature and salinity of 18°C and 36.5, respectively (Figure 2.2). In contrast, the modern annual subsurface conditions in the Bonaire Basin range from 19 °C at 150 m to 13 °C at 300 m, and salinities of 36 and 35.5 respectively [*Antonov et al.*, 2010]. As these SMW are presently deflected away from our site due to the strong western boundary current flowing through the Caribbean (Figure 2.2), several deep-water channels (up to 1500 m) allow water in Bonaire Basin to freely exchange with the open Caribbean and therefore, intermediate depth water changes in the western boundary current will affect hydrographic conditions in the basin.

To reconstruct surface conditions, we use the near-surface dwelling planktonic foraminifera *G. ruber* (white). *G. ruber* lives between 0-30 m depth and does not migrate

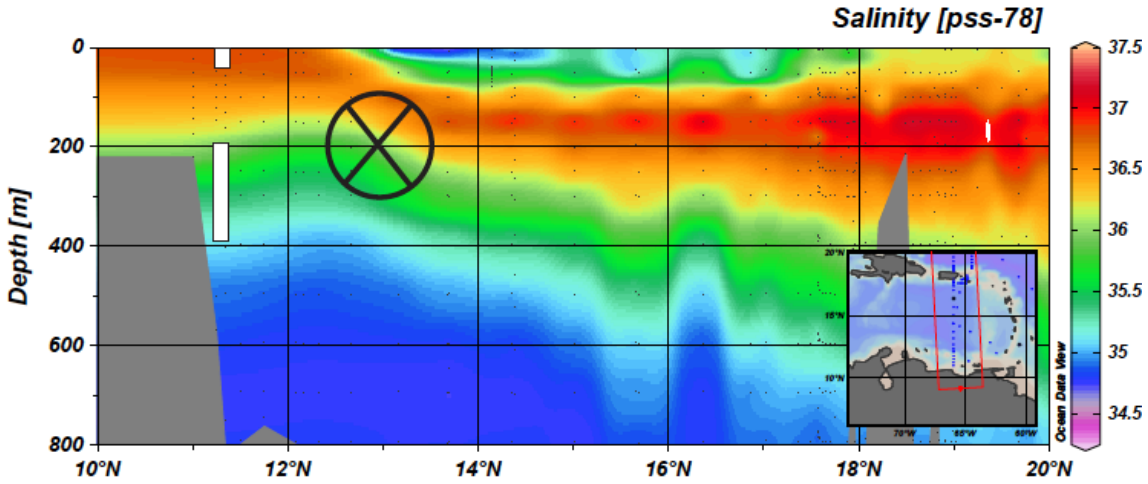

Figure 2.2 Caribbean Sea Cross Section. Vertical cross section across the Caribbean showing mean annual salinity along WOCE line A22 between 0-800 m. Salinity Maximum Waters are clearly defined as a salinity max at ~200 m. Sub surface conditions at the Bonaire Basin (11.33^{o}N) are considerably fresher as the western boundary current flows just north of the basin (black circle with X). White boxes at the core site correspond to the depth habitats of *G. ruber* (surface) and *G. truncatulinoides* (subsurface). *G. truncatulinoides* is well positioned to record changes in water masses as a result of western boundary current weakening. Figure made with Ocean Data View4.

to deeper waters to add a layer of gametogenic calcite at the end of its life cycle [*Bé*, 1980], so it is ideal for reconstructing tropical surface water conditions of the past [*Elderfield and Ganssen*, 2000; *Lea et al.*, 2000; *Lea et al.*, 2002]. Subsurface proxy records are generated using the deeper-dwelling planktonic foraminifera *G. truncatulinoides* (right coiling). Numerous studies from the Caribbean assign *G. truncatulinoides* a modern depth habitat of 200-400 m, ideally within the SMW depth range in the open Caribbean (Figure 2.2) [*Cleroux et al.*, 2009; *Steph et al.*, 2009]. Despite the tendency for *G. truncatulinoides* to have large vertical migrations within the water column, Mg/Ca and $\delta^{18}O_{calcite}$ ($\delta^{18}O_c$) values suggest calcification occurs in the lower thermocline in the tropical Atlantic [*Anand et al.*, 2003; *Cleroux et al.*, 2008; *McKenna and Prell*, 2004; *Sadekov et al.*, 2009]. Although *Cleroux et al.* [2009] found evidence that *G. truncatulinoides* may have migrated to a shallower depth range during the last deglacial in the Florida Straits, they hypothesized that this was the result of increased continental runoff and increased turbidity in the Florida Straits, forcing *G. truncatulinoides* to shallower depths for feeding [*Cleroux et al.*, 2009]. Because the Bonaire Basin would have remained far south of any significant deglacial or MIS 2 – 3 meltwater runoff, it expectedly did not experience similar changes in salinity and turbidity. Therefore, it is less likely that the depth habitat of *G. truncatulinoides* underwent significant changes in the past at the Bonaire Basin.

III.3. Materials and Methods

II.3.1 Age Model Development

The MIS 2 and 3 age model for VM12-107 is based on 9 monospecific planktonic foraminifera (*G. ruber*) samples analyzed for radiocarbon dates at the National Ocean Sciences Accelerator Mass Spectrometer facility at Woods Hole Oceanographic Institution. Radiocarbon ages were then converted to calendar ages using CALIB 7.1 using a standard marine reservoir age correction of 400 years (Table 2.1). Despite recent evidence from the Cariaco Basin suggesting this reservoir age may have varied by several hundred years during periods of AMOC slowdown during the deglacial [*Muscheler et al.*, 2008; *Southon et al.*, 2012], it is likely that these large changes were limited to localized areas such as the Cariaco Basin and did not affect the open Caribbean/Atlantic to a similar degree [*Southon et al.*, 2012].

Each radiocarbon date was converted to the most probable calendar age and plotted on Figure 3 with red error bars representing the 2-sigma error on the calibrated calendar age. Using linear interpolation between dates, our age model indicates a near constant MIS 2 and 3 sedimentation rate of 22 cm/kyr (Figure 2.3). This is very similar to the previously published deglacial age model (sedimentation rate of 18cm/kyr) based on ten calibrated ^{14}C dates from the deglacial and Holocene [*Schmidt et al.*, 2012b]. Although an age reversal in our radiocarbon dates occurs between the dates at 446.5 cm and 466.5 cm (Figure 2.3), the date for the 446.5 cm interval falls on a radiocarbon plateau, resulting in a large calibrated age range of more than +/- 450 years (Table 2.1). Given the smaller age range for the calibrated date for the 466.5 cm interval and the

visually out of sequence placement of the date at 446.5 cm (Figure 2.3), we decided to omit the radiocarbon date at 446.5 cm from our age model. However, it is important to

Depth (cm)	14C Age	Age error (y)	Calendar age (kyr)	(-) error (kyr)	(+) error (kyr)
2.5	1140	35	0.69	0.05	0.07
70.5	7900	55	8.37	0.13	0.13
82.5	9380	40	10.22	0.07	0.12
90.5	10050	65	11.05	0.26	0.14
104.5	10400	50	11.46	0.22	0.23
130.5	11200	50	12.67	0.1	0.16
160.5	12750	50	14.37	0.35	0.52
180.5	13450	60	15.74	0.56	0.64
220.5	15600	60	18.47	0.42	0.18
270.5	18500	90	21.59	0.26	0.47
318.5	19500	160	23	0.23	0.23
388.5	22300	220	26.14	0.23	0.2
416.5	23500	260	27.37	0.19	0.23
446.5	26000	360	29.77	0.45	0.49
466.5	25300	320	28.95	0.33	0.35
506.5	28400	470	31.96	0.62	0.47
548.5	29400	450	33.06	0.46	0.63
601.5	32200	170	35.69	0.21	0.23
688.5	35000	930	39.02	2.34	2.05

Table 2.1 VM12-107 Radiocarbon. VM12-107 raw AMS ^{14}C ages and calibrated calendar ages using the Calib 7.1 program and a standard marine reservoir age correction of 400 years. The red highlighted age reflects that age reversal which was omitted from our age model.

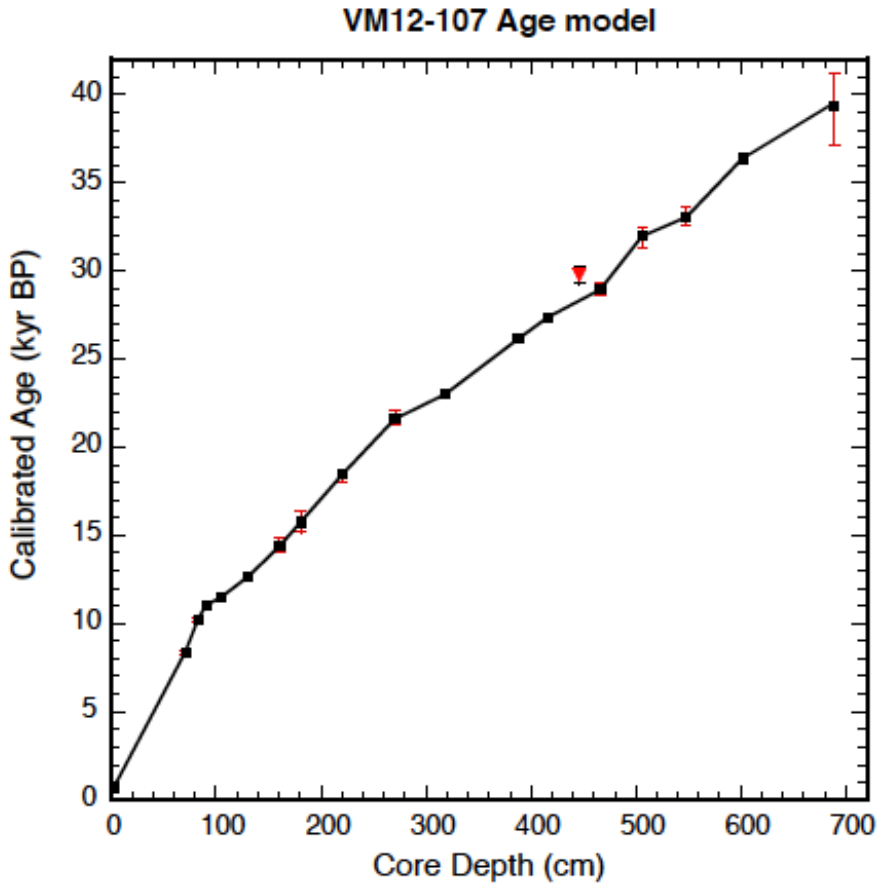

Figure 2.3 VM12-107 Age Model. The MIS 2 and 3 age model for VM12-107 is based on 9 calibrated radiocarbon dates between 300-688cm on the planktonic foraminifera *G. ruber,* in addition to 10 previously published radiocarbon dates spanning the deglacial interval. The resulting sedimentation rate based on linear interpolation was 22 cm/kyr. One out of sequence date at 446.5 cm was omitted from the age model (red triangle).

note that inclusion of the date at 446.5 cm does not significantly alter our age model or change the interpretation of our results. Beyond the final ^{14}C date at 40 kyr (689 cm core depth), we did not have a straightforward means to confidently assign ages for the final 120 cm of our record. We tried correlating the *G. ruber* $\delta^{18}O$ and Mg/Ca-SST records to NGRIP, but did not find a consistent relationship. This could be due, in part, to minor drying and cracking in this section of core that was noted during the collection of our samples by the technician at Lamont Doherty Earth Observatory. Therefore, to estimate ages in the last 120 cm of our core samples, we linearly extrapolated our MIS 2 and 3 average sedimentation rate. However, as a result of the uncertainties in dating this part of our record, we focus our interpretation and conclusions on the radiocarbon-constrained portion of our record ending at ~41 kyr.

II.3.2. Stable Isotope Analysis

The core was sampled at 2 cm resolution from 300-890 cm, corresponding to a MIS 2 and 3 temporal resolution of ~90 years/sample. First, sediment samples were disaggregated in ultra clean water for 4 hours on a shaker table and then wet sieved using a 63μm mesh. In order to limit ontogenetic and growth rate effects and to ensure an average population value, 15-20 *G. ruber* specimens where picked from the 250-355 um size fraction for each $\delta^{18}O$ measurement. Samples were then sonicated for 5-10 seconds in methanol and analyzed uncrushed on a Thermo Scientific MAT 253 IR-MS with Automated Kiel IV Carbonate Device at the Texas A&M College of Geoscience Stable Isotope Facility. The raw $\delta^{18}O$ values were standardized using NBS-19 and the long-term analytical precision on standards was less than ± 0.07 ‰.

II.3.3. Trace Metal Analysis

Trace metal analyses were performed on ~580 μg of *G. ruber* (35-40 shells, 250-355 μm size range) and *G. truncatulinoides* (7-10 shells, 355-425 μm size range) from each sample. Size fractions where chosen based on the shell sizes used in the Mg/Ca temperature calibration equations (see section II.3.4) and depth of habitat [*Steph et al.*, 2009]. Foraminifera were gently crushed between two glass slides, homogenized and then split into aliquots for duplicate analyses. We followed the cleaning procedure of *Schmidt et al.* [2012a], which includes sonication in ultra pure water and methanol to remove clays, a hot water bath in reducing agents to remove metal oxides and a final hot bath in oxidizing agents to remove organic material. Samples where then transferred into new, acid-leached vials and leached with weak nitric acid. Finally, samples were analyzed in replicate on a Thermo Scientific Element XR High Resolution Inductively Coupled-Plasma Mass Spectrometer at Texas A&M using isotope dilution. Based on a synthetic, matrix-matched Mg/Ca standard analyzed throughout this study, the analytical reproducibility for Mg/Ca was 1.20%. The pooled standard deviation on *G. ruber* duplicates is ± 4.0% (df=272) based on 285 intervals and on *G. truncatulinoides* duplicates is ± 4.3% (df=203) based on 230 intervals. All data are archived at the NOAA National Climate Data Center (http://www.ncdc.noaa.gov/paleo/paleo.html).

II.3.4. Calibration Equations

Measurements of Mg/Ca ratios in planktonic foraminiferal shells are a widely used tool for reconstructing past ocean temperatures [*Koutavas and Lynch-Stieglitz*, 2003; *Lea et al.*, 2000; *Rosenthal et al.*, 2003]. Both culturing studies [*Honisch et al.*,

2013; *Lea*, 1999; *Mashiotta et al.*, 1999; *Russell et al.*, 2004] as well as sediment and core top studies [*Anand et al.*, 2003; *Dekens et al.*, 2002; *Elderfield and Ganssen*, 2000; *Hastings et al.*, 1998; *McConnell and Thunell*, 2005; *McKenna and Prell*, 2004; *Rosenthal et al.*, 1997] show that temperature is the primary control of Mg/Ca ratios in formainiferal calcite. Although one study of core-top sediments across an Atlantic meridional transect claimed that salinity had a much stronger control on foraminiferal Mg/Ca ratios than temperature [*Arbuszewski et al.*, 2010], a new study showed that this conclusion likely resulted from latitudinal differences in foraminiferal dissolution resulting from regional productivity variability in surface waters and the incorrect application of a single depth-corrected Mg/Ca:SST calibration across the entire Atlantic basin [*Hertzberg and Schmidt*, 2013]. *Regenberg et al.* [2014] recently confirmed the fact that it is critically important to consider the heterogeneous effects of dissolution across the Atlantic (even at a single depth horizon) when generating Mg/Ca-SST records, and endorsed the conclusions drawn by *Hertzberg and Schmidt [2013]*.

Given the shallow depth of VM12-107 and the well-preserved nature of foraminiferal tests in the core, we chose the following Mg/Ca:SST calibrations of *Anand et al.* [2003] to reconstruct surface and subsurface temperature changes using *G. ruber* and *G. truncatulinoides, respectively*:

(1) multi-planktonic foraminifera calibration: $Mg/Ca=0.38 \exp(0.09*T)$ (error ± 1.1°C),

(2) G. truncatulinoides $Mg/Ca =0.359 \exp(0.09*T)$ (error ± 1.1°C).

We chose to use the species specific Mg/Ca:SST equation for *G. truncatulinoides* because it calculates a modern temperature of 14.2 °C, a good match with this species' modern depth habitat in the Bonaire Basin (Figure 2.2).

The oxygen isotopic composition of foraminiferal calcite is a function of both temperature and the isotopic composition of seawater ($\delta^{18}O_{sw}$) in which an individual shell precipitates. Because $\delta^{18}O_{sw}$ covaries linearly with salinity [*Charles and Fairbanks*, 1990], shell $\delta^{18}O_c$ can be used to estimate past salinity change if the temperature component can be isolated. Therefore, researchers developed a multi-proxy geochemical approach for calculating past changes in $\delta^{18}O_{sw}$ based on Mg/Ca paleothermometry and $\delta^{18}O_c$ measurements [*Carlson et al.*, 2008; *Lea et al.*, 2000; *Schmidt and Lynch-Stieglitz*, 2011; *Schmidt et al.*, 2012a; *Weldeab et al.*, 2007]. Numerous studies have used the low-light temperature: $\delta^{18}O$ relationship of *Bemis et al.* [1998] determined in laboratory culture experiments on the planktonic foraminifera *Orbulina universa* to compute $\delta^{18}O_{sw}$ in the Caribbean [*Lea et al.*, 2000; *Schmidt et al.*, 2004]. We also use the relationship from *Bemis et al.* [1998] to calculate $\delta^{18}O_{sw}$ using *G. ruber* $\delta^{18}O_c$ and Mg/Ca derived SST.

$$(3)\ T(^{o}C) = 16.5 - 4.80\ (\delta\ ^{18}O_c - (\delta\ ^{18}O_{sw} - 0.27\%))\ (\text{error} \pm 0.7^{o}C)$$

II.4. Results

II.4.1. *G. ruber* $\delta^{18}O_c$

The *G. ruber* $\delta^{18}O_c$ shows a long-term enrichment of nearly 0.8‰ from 50-22 kyr which reflects the progressive global cooling and build up of continental ice volume leading up to the LGM around 21 kyr (Figure 2.4a). Overlain on the long-term trend, the *G. ruber* $\delta^{18}O_c$ record displays numerous millennial-scale events, the largest of which increases by 0.6‰ within 3 samples (or about 300 years) at the onset of the stadial after DO 8 (37 kyr). Abrupt increases in $\delta^{18}O_c$ are also seen for stadials after DO 5, 7, and 11.

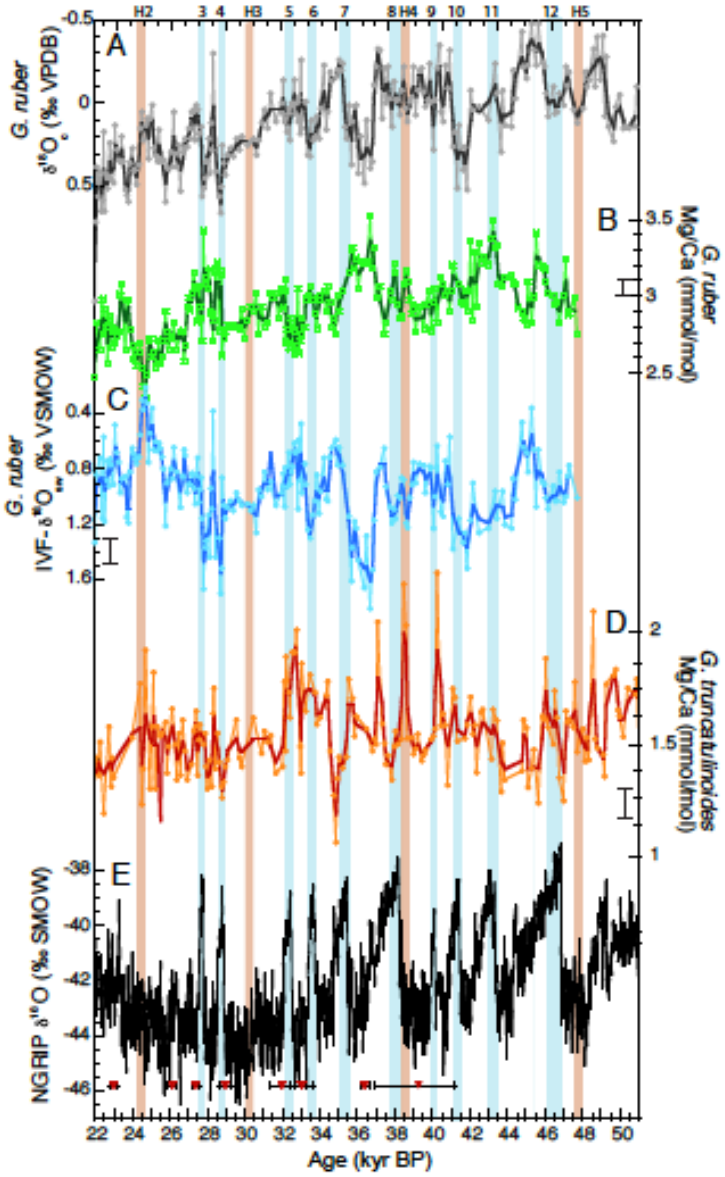

Figure 2.4 VM12-107 Results. *G. ruber* and *G. truncatulinoides* stable isotope and trace metal data. (A) G. *ruber* $\delta^{18}O_c$ (grey line: data; black line: 3pt weighted mean), (B) *G. ruber* Mg/Ca (light green line: data; dark green line: weighted 3pt mean), (C) *G. ruber* IVF-$\delta^{18}O_{sw}$ (light blue: data; dark blue: weighted 3pt mean), (D) *G. truncatulinoides* Mg/Ca (orange line: data; red line: weighted 3pt mean), (E) NGRIP $\delta^{18}O$ ice core record. Progressive cooling of glacial climate is seen in the $\delta^{18}O_c$ and Mg/Ca records as well as progressive freshening in the IVF-$\delta^{18}O_{sw}$. Superimposed on this trend are numerous millennial scale events that correlate with DO events in Greenland. Light blue boxes highlight peak interstadial conditions for each DO event. Orange boxes denote Heinrich events.

Because foraminiferal $\delta^{18}O_c$ values reflect both temperature and salinity, these positive excursions in the $\delta^{18}O_c$ record suggest either significant cooling and/or increased salinity of surface waters in the Bonaire Basin during stadials.

II.4.2. *G. ruber* Mg/Ca

G. ruber Mg/Ca ratios during MIS 2 and 3 range from 2.4-3.4 mmol/mol, with an average value of 2.92 mmol/mol. A correlation coefficient of -0.08 between shell weights and *G. ruber* Mg/Ca ratios provides evidence that dissolution did not significantly alter original Mg content. Overall, the *G. ruber* Mg/Ca record also shows a long-term decreasing trend of nearly 0.4 mmol/mol, equivalent to ~ 1.5°C, supporting the observation from $\delta^{18}O_c$ of progressive cooling leading up to the LGM (Figure 2.4b). Superimposed on the long-term cooling seen in the *G. ruber* Mg/Ca record are rapid increases in Mg/Ca ratios as large as 0.8 mmol/mol at DO 4, 5, 6, 8, 11, and 12. This equates to a change in temperature of ~3°C using Equation (1). Abrupt increases in SST are mostly associated with interstadials in the Greenland temperature record (Figure 2.4e). To explore this relationship, we calculated correlation coefficients between our *G. ruber* Mg/Ca record and NGRIP ice core $\delta^{18}O$ record for the section of the core constrained by radiocarbon dates (22 – 41 kyr) and for the section of the core possibly affected by shrinkage (42 – 48 kyr). An overall positive correlation of r=0.24 was found for the period between 22-41 kyr. In contrast, we calculate a correlation of only r=0.06 for the period from 42 – 48 kyr. This supports our earlier assumption that the final 6 kyr of the core was likely compromised by drying and cracking during storage. Therefore,

we limit our interpretation to the section of the core containing radiocarbon dates and not affected by core desiccation.

II.4.3. *G. ruber* $\delta^{18}O_{sw}$

Next, we calculate $\delta^{18}O_{sw}$ by combining the *G. ruber* Mg/Ca derived SST and the measured $\delta^{18}O_c$ using equation (3). We then corrected for continental ice volume change during this period using the sea-level record from *Waelbroeck et al.* [2002] to calculate the ice-volume free (IVF)-$\delta^{18}O_{sw}$ record (Figure 2.4c). Average MIS 2 & 3 was IVF-$\delta^{18}O_{sw}$ was 0.93‰ and remained more positive (saltier) than the modern IVF-$\delta^{18}O_{sw}$ values of 0.20‰. The most positive values in our record occur during H2. The largest oscillation is associated with the stadial after DO 8, suggesting a 0.9‰ increase in IVF-$\delta^{18}O_{sw}$ values at about 37.5 kyr. In addition, the stadials after DO 5 and 7 record similar magnitude increases in IVF-$\delta^{18}O_{sw}$ as large as 0.7‰. Nevertheless, there is not a significant correlation between our IVF-$\delta^{18}O_{sw}$ record and the NGRIP $\delta^{18}O$ record (correlation coefficient of -0.08).

II.4.4. *G. truncatulinoides* Mg/Ca and Mg/Ca-SST

Between 24-48kyr, Mg/Ca ratios in *G. truncatulinoides* range from 2.2 to 1.1 mmol/mol with an average value of 1.55 mmol/mol. The low correlation of -0.05 between *G. truncatulinoides* shell weights and Mg/Ca ratios rules out the possibility of a significant influence of dissolution on the *G. truncatulinoides* Mg/Ca record. A ~0.2 mmol/mol decrease characterizes the long-term variability of this record through MIS 2 and 3, consistent with the stable isotope data from *G. ruber*, indicating a prolonged cooling leading up the LGM. Superimposed on this gradual decrease are abrupt increases

in Mg/Ca (~0.6 mmol/mol) at the onset of stadial conditions after DO 4, 6, 7, 8 and 10, as well as during H4 (Figure 2.4). The average increase in Mg/Ca ratios across these events is about 0.43 mmol/mol. Using calibration equation (2), this equates to a warming of ~3.5^{o}C during most of these subsurface warming events. In general, these warm pulses occur at the initial onset of stadial conditions and appear to be a robust feature in five of the eight DO stadial transitions that are within the radiocarbon constrained portion of our record back to about 41 kyr (DO 4, 6, 7, 8, 10 and H4). However, the two stadials following DO 3 and 9 are not associated with subsurface warming events. Nevertheless, these are particularly short DO events in the Greenland record and it is therefore possible that either the change in AMOC was too weak, or our record may not have the resolution to resolve the subsurface warming associated with these brief events. It is also interesting to note that the subsurface warming does not appear to be sustained for the duration of the entire stadial event, but rather appears as a brief pulse at the onset of stadial conditions that lasts only a few hundred years. In addition, there is no increase in Mg/Ca at Heinrich Events 2 and 3.

II.5. Discussion

Our *G. ruber* stable isotope and trace metal data show clear, millennial scale variability during MIS 2 and 3. If both *G. ruber* and *G. truncatulinoides* were recording hydrographic conditions reflecting the propagation of SMW into the Bonaire Basin, we might expect that the *G. ruber* data would record an increase in salinity and temperature when the *G. truncatulinoides* warm. Indeed, this is the case during the stadial between DO 7 and 8 (36-38.5 kyr, 610-650cm) when the two records broadly support the

presence of SMW in the Bonaire Basin with a given correlation between *G. ruber* IVF-$\delta^{18}O_{sw}$ and *G. truncatulinoides* Mg/Ca equal to -0.77. However, this appears to be the only time where the two species are definitively recording similar conditions. Although the *G. truncatulinoides* Mg/Ca record suggests warming during several stadial events, the *G. ruber* data is less consistent. In many cases, the *G. ruber* Mg/Ca and IVF-$\delta^{18}O_{sw}$ data show cool/fresh or warm/fresh surface conditions in the Bonaire Basin during stadial events, for example at 29, 34.5 and 40 kyr. We suspect the inconsistency between the *G. ruber* and *G. truncatulinoides* records results from the fact that the *G. ruber* record is affected by the strong seasonality of surface waters in this region caused by the annual migration of the ITCZ [*Peterson et al.,* 2000; *Haug et al.,* 2001]. Today, the ITCZ sits north of the Bonaire Basin during summer, resulting in relatively warm, evaporative conditions in the basin. This seasonality is expressed in surface salinity, with 36.7 during summer and slightly lower at 36.3 during the wet winter. In addition, sea surface conditions in the Bonaire Basin are also influenced from the subsurface. During winter when the ITCZ is located south of the Bonaire Basin, the NE Trade winds cause upwelling to develop at the site (Figure 2.2). *Wan et al.* [2009] used a coupled ocean-atmosphere model to analyze how atmospheric and ocean circulation changes associated with a cooling of the North Atlantic affected the southern Caribbean. In their model, they found that the enhanced evaporative cooling due to the strengthened surface wind and the advection of cooler and drier air from the north led to a surface cooling, while ocean circulation changes caused a strong subsurface warming in this region. They concluded that this region is influenced by contrasting atmospheric changes from above

and ocean circulation changes from below the sea surface during cold periods in the North Atlantic. Therefore, it is likely that the Bonaire Basin *G. ruber* records integrate both oceanic and atmospheric signals, making them difficult to interpret, especially during periods of enhanced upwelling. We believe that is why it is difficult to identify a strong phase relationship between our *G. ruber* records and the Greenland ice core $\delta^{18}O$ record.

As discussed in Zhang [2007], *Chang et al.* [2008] and *Schmidt et al.* [2012b], a major reduction of AMOC can cause a significant weakening in the western boundary current through primarily oceanic wave adjustment, i.e., the first step process of the ocean teleconnection mechanism by *Chang et al.* [2008] and *Schmidt et al.* [2012b], resulting in strong subsurface warming in the western boundary current in the southern Caribbean and in the western tropical Atlantic. Warming pulses observed in our *G. truncatulinoides* Mg/Ca record are consistent with this mechanism during most DO cycles. Within the timespan of our reconstructions, we find evidence for subsurface warming during the stadials after DO 4, 6, 7, 8, and 10, as well as during H4 (Figure 2. 5). The pulse-like nature of these warmings also suggests that the second step process of the ocean teleconnection mechanism plays an important role for the termination of the events. As the AMOC continues to weaken, the equatorward pathway of the North Atlantic subtropical cell begins to open, allowing the warm SMW escapes the southern Caribbean Sea, terminating the TNA subsurface warming and eventually replacing the warm water by cooler water [*Chang et al.*, 2008]. Therefore, rather than a sustained

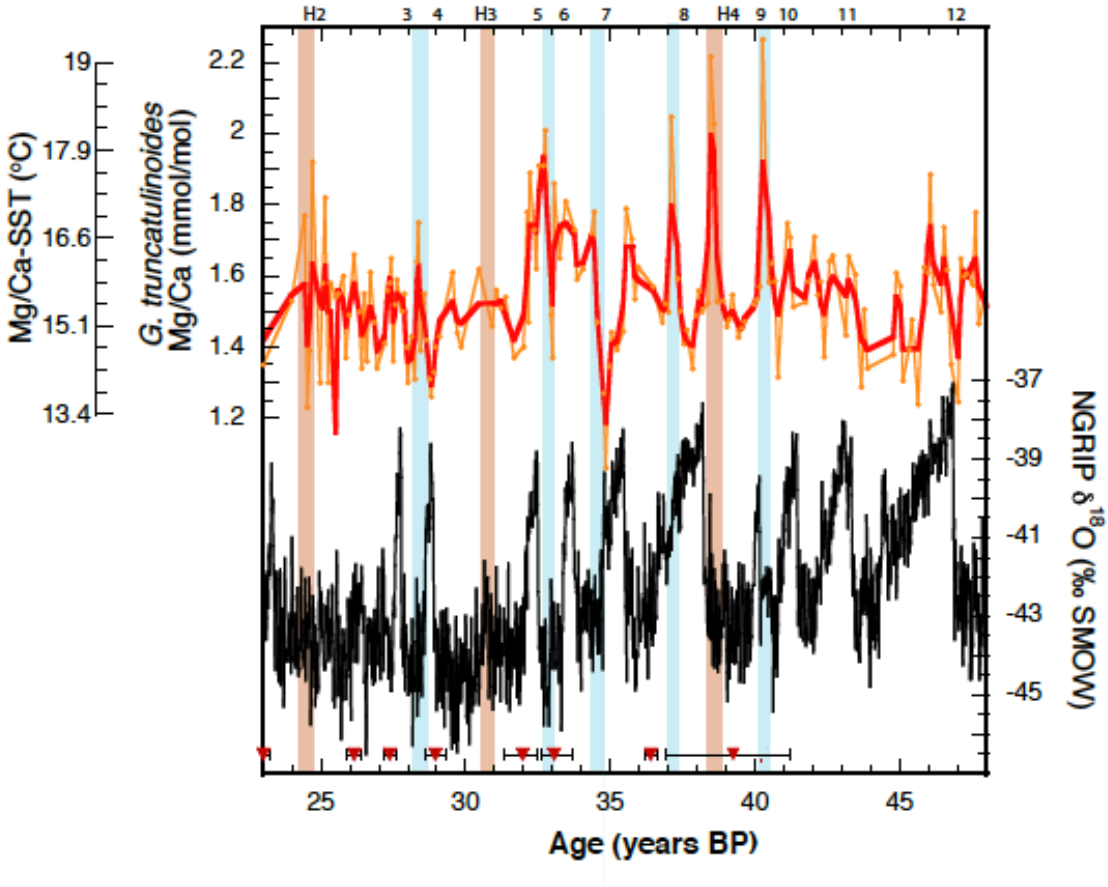

Figure 2.5 *G. truncatuloides* and NGRIP Comparison. *G. truncatulinoides* Mg/Ca data (orange line: data; red line: weighted 3 point mean) and NGRIP $\delta^{18}O$ ice core record (black line) for comparison. Light blue boxes represent DO intervals with apparent subsurface warming and are centered on the warming event. Orange boxes represent Heinrich events. Abrupt warmings of ~0.6 mmol/mol, or ~3.5°C characterize the onset of most DO stadials. Note that subsurface warming events are not associated with Heinrich events 2 and 3; however a large subsurface warming occurs at Heinrich event 4, possibly indicating Heinrich 2 and 3 were not associated with AMOC weakening.

warming for the duration of the stadial, cooler waters quickly follow the initial warming pulse. Interstadials are characterized by cooler subsurface conditions as AMOC strength increases and allows for the establishment of the steep subsurface gradient with warmer waters in the North Atlantic gyre and cooler waters in the deep Tropics (Figure 2.1). DO stadial 3 and 9 do not show a subsurface warming. These DO events are relatively small, short events compared to the much larger DO 7 and 8 where robust warming is recorded. It is possible that no subsurface warming is recorded for these events because they are too short for the temporal resolution of our record to resolve. Or, a second possible explanation could be that there was not a large enough slowdown of AMOC to permit SMW into the Caribbean during these stadials. In addition, there does not appear to be a relationship between the size and duration of a DO event and the magnitude of subsurface warming in the TNA; the shorter DO events 4, 6, and 10 show the same amount of subsurface warming of ~3 ^{o}C in the following stadials as does the larger DO 8 at 37.5 kyr.

Although modeling results indicate subsurface temperatures in the Bonaire Basin should be sensitive to AMOC variability [*Schmidt et al.,* 2012b], it is also possible that other oceanographic and atmospheric circulation changes affected the vertical temperature profile at our core site. High-resolution studies from the nearby Cariaco Basin showed that the ITCZ in the tropical Atlantic shifts south during cold periods in the North Atlantic, resulting in increased upwelling along the northern coast of South America [Peterson et al., 1991 and 2000]. As the ITCZ shifted southward away from the southern Caribbean, the Bonaire Basin would have been more influenced by the

Northeast Trades for longer periods of time, most likely resulting in enhanced coastal upwelling. During these times, we would expect the thermocline to shoal and the upper water column to cool. Nevertheless, during many of the DO stadials in our record, we find just the opposite, a warming of subsurface conditions at our site. Therefore, we believe subsurface changes associated with AMOC variability are the most likely driver of subsurface temperature change in the Bonaire Basin.

The observations of abrupt warmings in the *G. truncatulinoides* Mg/Ca data during the onset of stadial conditions in Greenland are also consistent with the subsurface warming observed in *Schmidt et al.* [2012b] across the last deglacial period. Using the same core and the subsurface dwelling species *G. crassaformis*, *Schmidt et al.* [2012b] identified subsurface warmings of 3^{o}C and 1.7^{o}C during the YD and H1, respectively. In this study, we use *G. truncatulinoides* rather than *G. crassaformis* due to the low abundance of *G. crassaformis* deeper in the core after the LGM. However, both species share considerable overlap in their habitat depth ranges and both live in the lower thermocline [*Steph et al.*, 2009], well within the 300-600 m depth over which maximum subsurface warming occurs according to models [*Chang et al.*, 2008; *Schmidt et al.*, 2012b; *Steph et al.*, 2009; Zhang, 2007]. Given these similarities, our new subsurface temperature record suggests that AMOC was in a reduced state during most of the DO stadial events of late MIS 3.

A new study by *Bohm et al.* [2015] used the water mass tracers $^{231}Pa/^{230}Th$ and ε_{Nd} to characterize Atlantic water mass export over the last full glacial-interglacial cycle. They concluded that AMOC was only slightly reduced overall during MIS 3 as

compared to AMOC strength during the Holocene. Our new subsurface record would suggest that this strong mode of interstadial AMOC strength during MIS 3 was periodically reduced during stadials, suggesting that AMOC played an important role in DO climate cycles. Given their study's lower sample resolution during MIS 3, we suspect they were unable to resolve the brief periods of weak AMOC during DO stadials.

Our data also supports a recent reconstruction of little or no AMOC change during Heinrich events 2 and 3. *Lynch-Stieglitz et al.* [2014] reconstructed past changes in the density gradient across the Florida Straits using benthic foraminiferal $\delta^{18}O_c$ as a proxy for AMOC variability over the past 35 kyr. Based on the geostrophic method, these researchers found no evidence for a reduction in AMOC across Heinrich events 2 and 3, and reasoned that AMOC was already in a weakened state and therefore did not experience any further reduction during these events. Similarly, our new subsurface temperature records show no warming across these two Heinrich events at 24.5 and 30.2 kyr (Figure 2.5). In contrast, Heinrich event 4 is recorded as a very large warming just prior to DO 8 at ~39 kyr. This Heinrich 4 - DO 8 sequence is the best-resolved event in our record and suggests a strong subsurface warming during Heinrich 4 within the stadial after DO 8. While the geostrophic flow reconstructions of *Lynch-Stieglitz et al.* [2014] do not extend back to H4, *Bohm et al.* [2015] also found evidence for a significant slowdown in AMOC during H4. It is important to note that we identified the age ranges for Heinrich Events as recorded in the absolute dated Hulu Cave speleothem records [*Wang et al.,* 2001]. Therefore, we believe our results provide additional

evidence that the mechanisms responsible for Heinrich Events varied under different climate states, as concluded in *Lynch-Stieglitz et al.* [2014].

The connection between subsurface warming events in the TNA and AMOC variability during MIS 3 are also consistent with the new modeling study of *Zhang et al.* [2015] who used the CCSM3 to model AMOC response to ocean temperature anomalies under MIS 3 boundary conditions. Their data suggest AMOC varied by ~9.2 Sv between stadial to interstadial conditions, with a net flow of ~11 Sv during stadials. Although our method cannot quantify the magnitude of AMOC change, based on the modeling experiments of *Chang et al.* [2008] and *Schmidt et al.* [2012b] for which the subsurface warming mechanism was identified, a 0.1 Sv water hosing applied to LGM boundary conditions resulted in a similar reduction of AMOC strength to ~9.5 Sv and produced a subsurface warming near our location between 2-3^{o}C. These modeling results are therefore consistent with the magnitude of *G. truncatulinoides* warming observed in our record associated with most DO stadials over the last 41 kyr.

II.6. Conclusions

We present new stable isotope and trace metal data from surface and subsurface dwelling planktonic foraminifera to investigate the role of AMOC during DO events. Although our new surface records of temperature and salinity change are difficult to correlate to high latitude climate change because they are influenced by both atmospheric and ocean circulation changes during MIS 2 and 3, our subsurface temperature record reveals distinct warmings at the onset of most cold DO stadials in the North Atlantic back to 41 kyr. This pattern of subsurface warming is consistent with a

subsurface warming mechanism linked to reduced northward transport in the western boundary current and the influx of SMWs into the deep tropics. This pattern of surface temperature change provides evidence for an anti-correlated relationship between subsurface TNA temperatures and AMOC strength during MIS 3 and suggests that AMOC was significantly reduced during DO stadials. Additionally, our results support recent conclusions reached by *Lynch-Stieglitz et al*. [2014] that glacial Heinrich events 2 and 3 saw little change in the strength of AMOC. Collectively, our new records provide insight into the dynamic processes that influenced glacial climate.

CHAPTER III

A NEW PERSPECTIVE ON WEST AFRICAN HYDROCLIMATE DURING THE LAST DEGLACIAITON

III.1. Introduction

Prolonged droughts across West Africa impart significant socio-economic hardships on developing nations. Complex interactions between the ocean, land, atmosphere, and local solar insolation result in non-linear feedbacks that make understanding past and future climate changes in this part of the world extremely difficult [*deMenocal et al.*, 2000]. These complexities are exemplified in paleo-hydrological reconstructions from West Africa, where the deglacial history of precipitation varies as a function of both proxy and location. Northwest African proxy reconstructions of continental aridity, including dust flux and grain size records from continental shelf sediment cores, point to a severe and widespread drought that characterized Heinrich Event 1 (H1, 16.7-15.1 kyr) [*Collins et al.*, 2013; *Mulitza et al.*, 2008; *Stager et al.*, 2011; *Tjallingii et al.*, 2008]. During this time, dust emissions from the Sahara and Sahel were on average five times higher compared to the early Holocene humid interval [*McGee et al.*, 2013]. In contrast, previously published records of sea surface salinity (SSS) and river discharge from the eastern Gulf of Guinea, which have been interpreted to reflect West African precipitation runoff, suggest little or no change

in West African runoff during H1 [*Weldeab et al.*, 2007]. A second discrepancy between regional precipitation proxies occurs during the deglacial cold reversal known as the Younger Dryas (YD, ~11.2-12.9 kyr). During this period, records from northwest Africa record much smaller increases in dust flux relative to H1, implying less intense drought conditions [*Mulitza et al.*, 2008; *Tjallingii et al.*, 2008], whereas SSS and river discharge records from the Gulf of Guinea suggest a severe reduction in riverine discharge during the YD [*Weldeab et al.*, 2007]. Clearly, questions surrounding the drought history of West Africa remain.

Another uncertainty in the interpretation of published dust records regards the extent to which wind speed versus aridity influences dust fluxes. During the H1 and YD cold reversals, steepened meridional temperature gradients in the North Atlantic resulted in stronger trade winds over West Africa [*McGee et al.*, 2010]. Intensified winds have the ability to increase dust mobilization, resulting in drought-like dust signals independent of hydroclimate change across the Sahara and Sahel during H1 and YD. Recently, observations linked wind strength, not aridity, as the most significant source of inter-annual to decadal variability of Saharan aerosol emissions [*Ridley et al.*, 2014; *Rodriguez et al.*, 2015], and modeling studies support the role of wind as a driver of enhanced deglacial dust flux [*Murphy et al.*, 2014]. Nevertheless, there is limited evidence of sub-Saharan hydroclimate change during the deglaciation to confirm aridity patterns, making it difficult to determine whether changes in continental aridity or wind strength played a more important role in driving deglacial dust emissions from the Sahara and Sahel.

In order to more accurately reconstruct temporal changes in the West African Monsoon (WAM) system across the last deglaciation, we present new records of hydrologic change in the Niger River drainage basin from sediment core Fan 17 (4.81^{o}N, 4.45^{o}E, 1178m water depth) over the last 21 kyr based on stable oxygen isotopes and trace metal analyses on the planktonic foraminifera *Globigerinoides ruber*. We combine Mg/Ca-sea surface temperature (SST) estimates with measured $\delta^{18}O_{calcite}$ ($\delta^{18}O_c$) values to calculate $\delta^{18}O_{sw}$ values, a proxy for SSS. In addition, we measure Ba/Ca ratios in *G. ruber* as a proxy for past discharge variability from the Niger River. We then compare our results with $\delta^{18}O_{sw}$ and Ba/Ca records from a core located in the Gulf of Guinea, MD03-2707 [*Weldeab et al*. 2007], to explore subtle differences in the timing of regional monsoon development during the deglaciation. Core MD03-2707 is located farther east of Fan 17 in the low salinity core of the Gulf of Guinea, very close to equatorial river runoff. Using the differences between the Fan 17 and MD03-2707 Ba/Ca records, we show that monsoon onset over West Africa and the Sahel was more gradual than previously thought, and has important implications for the interpretation of deglacial dust records from the northwest coast of Africa.

III.2. Oceanography around the Niger Delta

Sediment core Fan 17 was collected by Shell Oil in 2007 and donated to Texas A&M University for research purposes (Figure 3.1). An intraslope sandy turbidite lobe deposit exists to the northwest of Fan 17, but seismic data indicates that Fan 17 is not disturbed by mass wasting and turbidity currents depositing sand on the intraslope lobe. Mean annual SST at the core location is 27.8^{o}C with less than 1^{o}C of seasonal

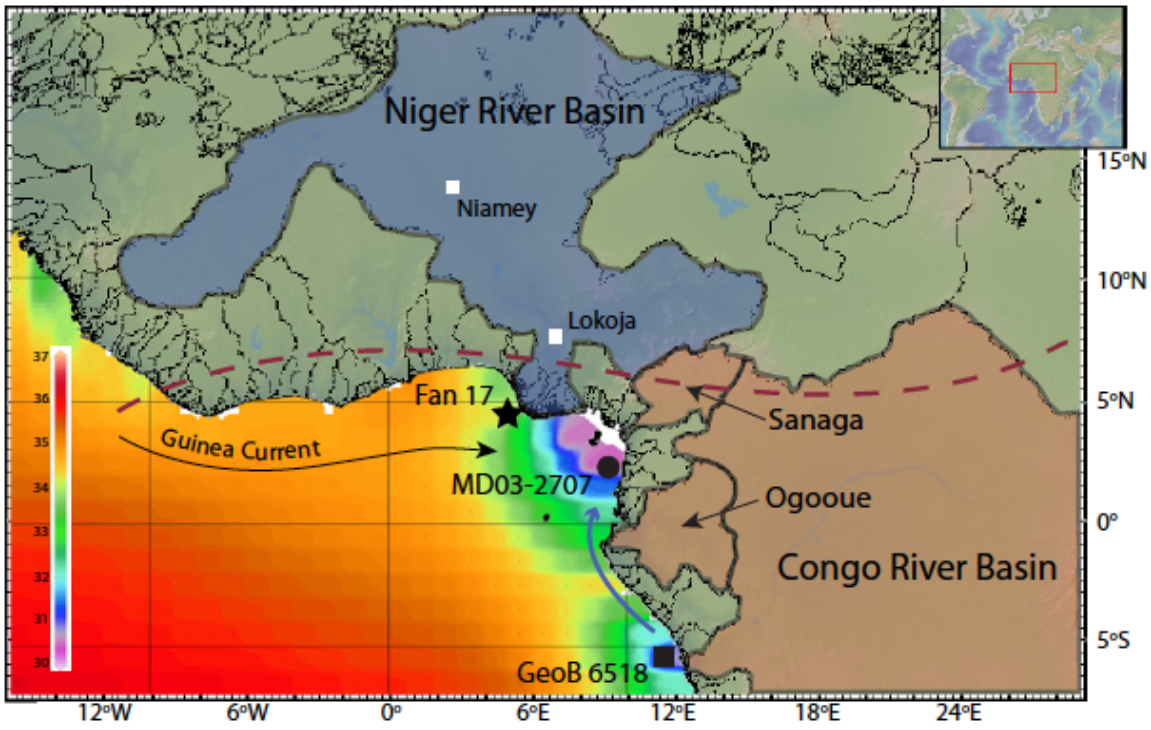

Figure 3.1 Gulf of Guinea Overview Map. Regional map of major West and Equatorial African river basins that drain into the Gulf of Guinea. Niger Delta core Fan 17 (black star) was recovered in 1178 m of water less than 100 km equidistant from the two major Niger River distributaries. MD03-2707 (black circle) is located 400 km southeast of the Niger River Delta in the low salinity core for the Gulf of Guinea, where freshwater from the Niger and other major Central Africa rivers including the Congo River (blue arrow) also contribute to the low SSS. Red dashed line represents the approximate position of surface wind convergence during boreal winter. The Niger and Congo River drainage basins are outlined by shaded blue and brown, respectively. GeoB-6508 (black square) is located near the mouth of the Congo River.

variability. SSS in the Niger Delta ranges from 32 during the wet summer months to 34.5 during the dry winters, with an annual average of 33.4. The low SSS during the summer months is a direct result of the monsoon that develops across West Africa (Figure 3.1). The Guinea Current running along the Guinea Coast moves discharge from the Niger River eastward. The location of Fan 17 close to the shelf break and roughly 100km equidistant from the two main distributaries of the Niger River make it ideal for continuously monitoring river runoff regardless of changes in sea level or delta lobe avulsion.

During boreal summer, differential heating between the land and ocean creates an onshore wind that transports moisture rich air from the Gulf of Guinea to a zone of ascent caused by the juxtaposition between the axes of two mid-level atmospheric jets [*Nicholson*, 2008]. The resultant tropical rainbelt sets up over the Niger River Basin and is responsible for producing most of the rains associated with the seasonal monsoon throughout much of sub-Saharan West Africa, including the Sahel. Hydrographic data along the Niger River show that precipitation falling in the Sahelian latitudes of the Niger River Basin (12-18^{o}N) is the main determinant of the magnitude of discharge at the Niger Delta, and riverine flow is therefore strongly related to the intensity of the rainbelt [*Itiveh and Bigg*, 2008]. This discharge contributes to the very low salinities of the modern Gulf of Guinea (Figure 3.1). However, the Niger River is not the only river that contributes to the low salinities in the Gulf of Guinea. Freshwater from the Ogooue and Congo rivers also contribute large amounts of runoff to the Gulf of Guinea along with other smaller equatorial rivers (Figure 3.1).

III.3. Methods

III.3.1. Age Model Development

The age model for Fan 17 is based 11 radiocarbon-dated intervals measured using accelerator mass spectrometry at Lawrence Livermore National Laboratory (6 of which constrain the deglacial interval of our record). The ^{14}C ages were converted to calendar ages using the CALIB 7.1 program and a standard marine reservoir age correction of 400 years [*Stuiver et al.*, 2013]. One out-of-sequence date at 285 cm was not included in this age model (Figure 3.2). The core is well preserved with no sedimentological evidence for turbidite layers disturbing the deglacial sequence. However, visual inspection of the core logs indicates evidence of enhanced bioturbation at around 285 cm in the core. This enhanced bioturbation could have mixed older sediments in this interval. Therefore, we omitted this sample from our age model. Assuming linear sedimentation rates between calibrated ages, the resulting age model yields a mean deglacial and Holocene sedimentation rate of ~16.9 cm/kyr (Figure 3.2). Fan 17 was subsequently sampled at 2 cm intervals, corresponding to a temporal resolution of ~120 years.

III.3.2. Isotope Measurements

Sediment samples from Fan 17 were disaggregated in ultra-pure deionized water and sieved with a 63 μm mesh. In order to limit ontogenetic and growth rate effects on shell geochemistry, *G. ruber* (pink) specimens were picked from the 250-355 μm size fraction. The pink variety of *G. ruber* was selected because its abundance was much higher than white *G. rubers* in the Fan 17 sediment samples and also used in other

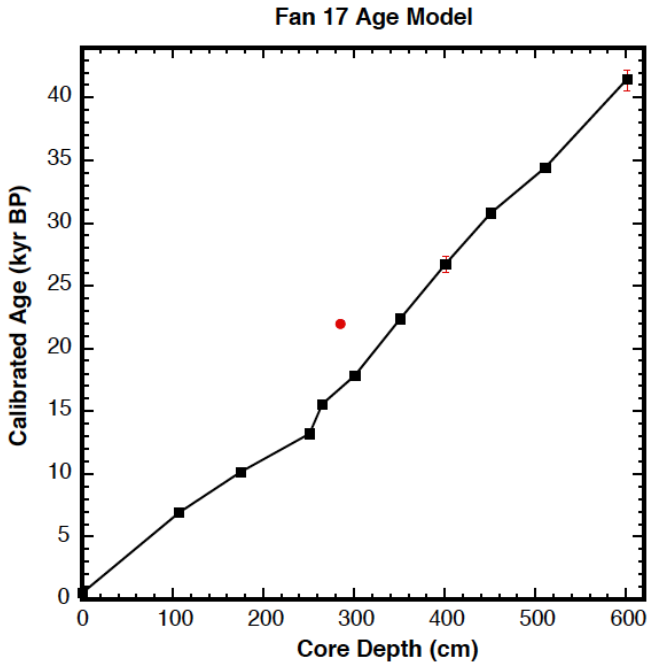

Fig 3.2 Fan 17 Age Model. Age model for Fan 17 is constrained by linear interpolation between 11 radiocarbon analyses converted to calendar years using CALIB 7.1. One out of sequence data was omitted at 285cm (red circle). All radiocarbon analysis was performed at Lawrence Livermore National Laboratory.

reconstructions from this region [*Weldeab et al*. 2007]. *G. ruber* tests were then sonicated for 5-10 seconds in methanol and analyzed whole on a Thermo Scientific MAT 253 IR-MS with Automated Kiel IV Carbonate Device at the Texas A&M College of Geoscience Stable Isotope Facility. 15-20 *G. ruber* tests per samples were analyzed in order to get a statistical average of the natural range in $\delta^{18}O$ variability within each population of foraminifera. Raw $\delta^{18}O$ values were standardized using NBS-19.

III.3.3. Trace Metal Measurements

We performed trace metal analyses on the same population and size fraction of *G. ruber* used for stable isotope analyses. Up to ~580 μg (~35-40 shells) of *G. ruber* (pink) were gently crushed between two glass slides, homogenized, and then split into duplicate samples for analysis. We followed established cleaning procedures of *Schmidt et al.* [2012], which includes sonication in methanol to remove clays, a hot water bath in reducing agents to remove metal oxides, and a final hot water bath in oxidizing agents to remove organic material. Samples were then transferred into acid cleaned vials and leached with weak nitric acid. All clean work was conducted in laminar flow benches under trace metal clean conditions. Lastly, samples were analyzed in replicate on a Thermo Scientific Element XR High Resolution Inductively Coupled Plasma Mass Spectrometer at Texas A&M using isotope dilution. A suite of elements was analyzed including Na, Mg, Ba, U, Al, Mn, Al, and Fe. We excluded analyses with anomalously high Al/Ca (>100 μmol/mol), Mn/Ca and Fe/Ca (>200 μmom/mol), which indicated samples where detrital clays and digenetic coats were not sufficiently removed during cleaning. We also rejected measurements with very low percent recovery (<10%) where

the loss of shell material during trace metal cleaning was likely the result of human error.

III.3.4. XRF Measurements

XRF data were obtained by scanning core Fan 17 at 1 cm intervals using the X-ray Fluorescence Avvatech core scanner at the International Ocean Discovery Program facility at Texas A&M University. Reduction of this data followed the procedures presented by *Lyle et al.* [2012]. Briefly, we scaled the data to average upper crustal compositions using values from *Taylor and Mclennan* [1995], which converts the elemental peak areas into typical ranges of sediment composition. To account for changes in sediment density arising from cracks and sediment porosity, we took the scaled XRF data and normalized the components to sum to 100%. The biogenic component of the sediment was calibrated using 20 samples measured for total carbonate content using an Automate Prep Device to react weighted aliquots of bulk sediment with acid and a Coulometrics CO_2 Coulometer to measure the resultant % $CaCO_3$ of the sediment. Using these data, we corrected the normalized XRF data to carbonate free in order to remove the impact of dilution due to variable carbonate composition in the sediments.

III.3.5. Calculations

We converted our Mg/Ca ratios to SST using the multi-species relationship of *Anand et al.* [2003]:

$$Mg/Ca = 0.38 \exp(0.09*SST) \text{ (error} = \pm 0.5\ ^{o}C). \quad \text{Eq. [1]}$$

Given the shallow water depth of Fan 17 and the lack of visual evidence for significant dissolution of foraminiferal calcite, this equation best suits our record because it does not include a dissolution-corrected term needed for deeper locations. Furthermore, *Hertzberg and Schmidt* [2013] showed there was only a minor salinity effect on *G. ruber* Mg/Ca ratios, and argued that calibration equation [1] worked well for calculating SSTs in the Atlantic when using well preserved shell material. Then, we combine the Mg/Ca derived SST with measured $\delta^{18}O_c$ values to compute $\delta^{18}O_{sw}$ using the low-light relationship from *Bemis et al.* [1998]:

$$SST(^oC) = 16.5 - 4.80(\delta^{18}O_c - (\delta^{18}O_{sw} - 0.27‰)). \quad \text{Eq. [2]}$$

Finally, during periods of enhanced continental ice storage, the oceans become enriched in ^{18}O relative to ^{16}O. We removed this effect of ice volume on our $\delta^{18}O_{sw}$ record using the sea-level record of *Waelbroeck et al.* [2002] where a maximum enrichment of $\delta^{18}O$ at the LGM was equal to 1.04‰ enrichment of the ocean. The resulting record of ice-volume free (IVF) $\delta^{18}O_{sw}$ provides a measure of regional surface water $\delta^{18}O$ variability.

III.3.6. Error Analysis

The long-term analytical precision for $\delta^{18}O$ measurements is less than ± 0.07‰, based on the NBS-19 standard. Based on a synthetic, matrix-matched standard analyzed throughout this study, the analytical reproducibility for Mg/Ca is 1.13%. The pooled standard deviation of all replicate *G. ruber* Mg/Ca analyses is ± 3.08% (1 SD, df=103) based on 110 measured intervals. Given the average *G. ruber* Mg/Ca ratio for this study of 3.46 mmol/mol, this error equates to ±0.11 mmol/mol or ± 0.71°C. Similarly for Ba/Ca, the long-term analytical precision based on a matrix-matched standard is 2.02%.

The pooled standard deviation is ±7.2% (1 SD, df=103) based on 110 intervals. Average Ba/Ca for this study is 1.14 μmol/mol equal to an error of ±0.08 μmol/mol.

We calculated the ± 1σ error of the calculated $\delta^{18}O_{sw}$ values by propagating the 1σ analytical error from the Mg/Ca and $\delta^{18}O_c$ analyses, as well as the errors reported for the Mg/Ca-SST and $\delta^{18}O_c$: SST calibrations. The estimated 1σ error for the $\delta^{18}O_{sw}$ is ± 0.24‰, which is consistent with reported error propagations from prior studies ranging between ±0.18‰ to ±0.26‰ [*Schmidt and Lynch-Stieglitz*, 2011; *Schmidt et al.*, 2012]. To calculate the error on the smoothed IVF- $\delta^{18}O_{sw}$ we used the following equation: $\sigma = \sigma_{propogated} / \sqrt{n}$ (where n is the number of points used in the smoothing function).

III.4. Results and Discussion

III.4.1. Mg/Ca-SST Record

The calculated core-top SST for *G. ruber* in Fan 17 was 25.6 ^{o}C using equation [1]. Modern mean annual SST at the Niger Delta is 27.8 ^{o}C with little seasonal variability. However, *G. ruber* does not live at the immediate water surface (0 m depth), but instead lives slightly deeper at depths between 10-40 m in the EEA [*Steph et al.*, 2009]. The mixed layer temperature at 30 m depth in the Niger Delta is 26.1 ^{o}C, making the calculated core top temperature within the calibration uncertainty and consistent with the depth habitat for *G. ruber*.

The Fan 17 *G. ruber* Mg/Ca derived SST record from the Niger Delta indicates a glacial-interglacial rise in EEA SST of 4^{o}C across the last deglacial (Figure 3.3b). Minimum temperatures of 22.1^{o}C characterized the LGM, with SST variability of ~1^{o}C between 17.5 – 20 kyr. By the start of H1, temperatures start to gradually increase from

Figure 3.3 Fan 17 Results. Fan 17 *G. ruber* (A) $\delta^{18}O_c$, (B) Mg/Ca SST (^oC) and calculated ±1σ error next to axis, (C) $\delta^{18}O_{sw}$ plotted as open purple squares with three-point weighted mean as purple line, and calculated ±1σ error for the smoothed record next to axis (D) IVF-$\delta^{18}O_{sw}$ plotted as grey circles with three point weighted mean pink line. Pink shading represents the ± 1σ error of the smoothed data (see text for details on how the error was calculated). (E) Ba/Ca ratios (μmmol/mol) plotted as blue line with blue shading denoting the ± 1σ error of the data and (F) NGRIP $\delta^{18}O$ for the last 21 kyr. Mg/Ca was converted to SST using Mg/Ca=0.38exp(0.09T) [*Anand et al*. 2003]. The $\delta^{18}O_{sw}$ was then calculated using the Mg/Ca-derived SST and $\delta^{18}O_c$ using $T(^oC)= 16.5 - 4.80 (\delta_c - (\delta_w - 0.27))$ [*Bemis et al*. 1998]. Red triangles show the calibrated radiocarbon ages used in the age model and associated 2 sigma error bars. The age model for Fan 17 is based on 11 radiocarbon dates converted to calendar age using CALIB 7.0, indicated by red triangles on the x-axis.

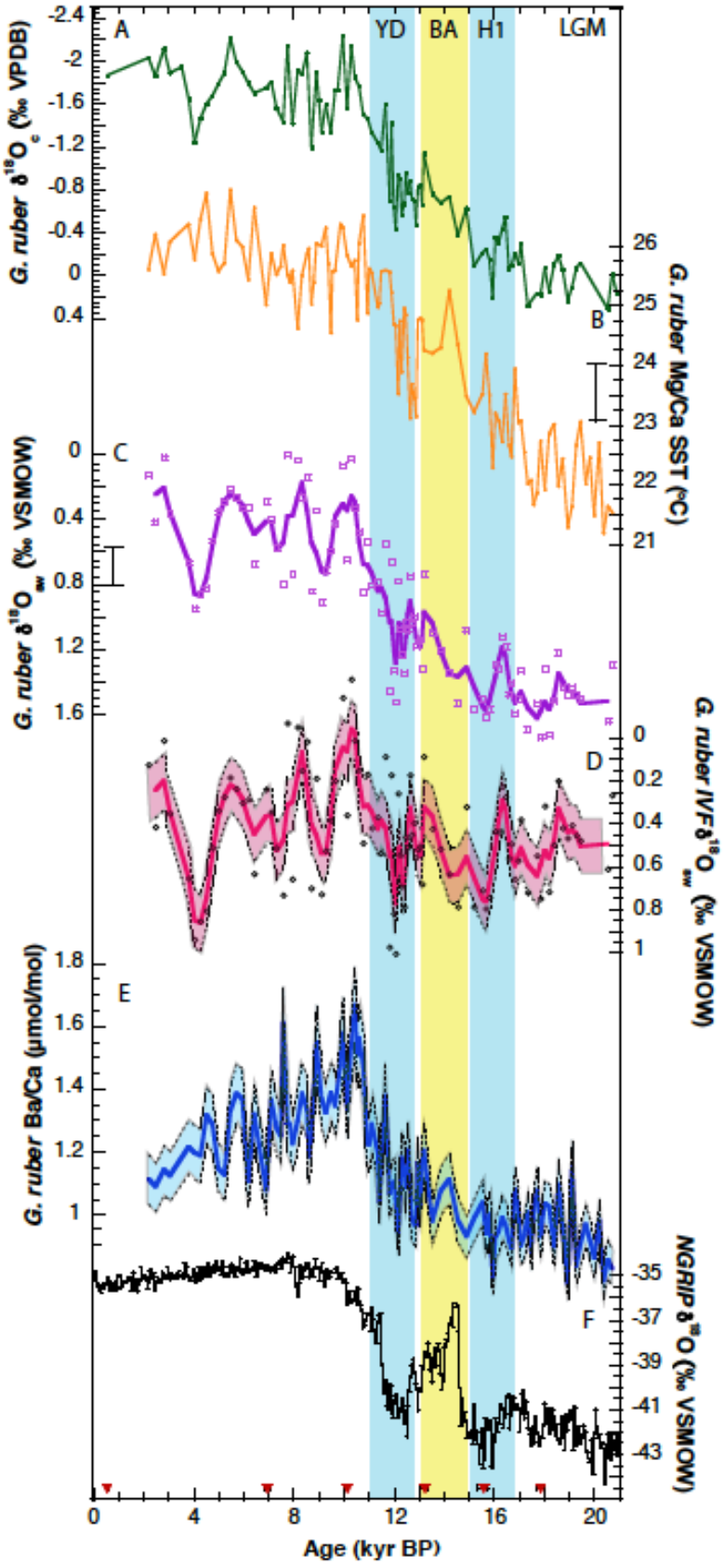
A
YD
BA
H1
LGM
G. ruber δ18Oc (‰ VPDB)
-2.4
-2
-1.6
-1.2
-0.8
-0.4
0
0.4
B
G. ruber Mg/Ca SST (°C)
26
25
24
23
22
21
C
G. ruber δ18Osw (‰ VSMOW)
0
0.4
0.8
1.2
1.6
D
G. ruber IVF δ18Osw (‰ VSMOW)
0
0.2
0.4
0.6
0.8
1
E
G. ruber Ba/Ca (µmol/mol)
1.8
1.6
1.4
1.2
1
F
NGRIP δ18O (‰ VSMOW)
-35
-37
-39
-41
-43
0
4
8
12
16
20
Age (kyr BP)

22.1 ^{o}C at 17.5 kyr to 23.6 ^{o}C by 15 kyr (Fig. 3B). The Fan 17 record suggests SST increases by another degree at the start of the Bølling Allerød (BA) to 24.6 ^{o}C. At the start of the YD around 12.9 kyr, temperatures abruptly decrease by 1.5 ^{o}C an then rebound by 2 ^{o}C during the middle and later half of the YD from 12 to 11 kyr. A near modern temperature of 25.7 ^{o}C is reached during the early Holocene (Figure 3.3). Temperatures during the Holocene vary between 24.4 and 26^{o}C for the duration of the Holocene.

H1 and the YD are thought to be associated with slowdowns of the Atlantic Meridional Overturning Circulation (AMOC) [*McManus et al.*, 2004]. Modeling studies have shown that the transmission of North Atlantic cooling to the tropical Atlantic during times of weak AMOC is transferred via both atmospheric and oceanic processes [*Chang et al.*, 2008]. In locations influenced by local upwelling, reorganizations of ocean circulation may also result in a warming of subsurface waters that is more significant than the cooling via the atmosphere during AMOC slowdown [*Wan et al.*, 2009], thus explaining why some locations across the tropical Atlantic record cooling during the YD, and others a warming. Modeling results suggest a warming of subsurface waters in the EEA during periods of reduced AMOC [*Chang et al.,* 2008; *Schmidt et al*., 2012]. Therefore, the influence of coastal upwelling around the Niger Delta likely resulted in a warming during H1 as subsurface temperatures increased in response to an AMOC shutdown. In contrast, the cooling of surface waters at the start of the YD suggests that the effect of atmospheric cooling may have been greater during this time. Finally, both the *G. ruber* $\delta^{18}O_c$ and Mg/Ca-SST records indicate a warming during the

second half of the YD (Figure 3.3). This warming may be related to the reduced northward heat transport out of the tropical Atlantic when AMOC was reduced, as observed in other tropical Atlantic locations including the eastern tropical Atlantic, the Caribbean, and the Florida Straits [*Schmidt and Spero*, 2011; *Schmidt and Lynch-Stieglitz*, 2011].

In addition, the deglacial portion of our Fan 17 Mg/Ca SST record resembles a nearby record of *G. ruber* (pink) Mg/Ca-SST from core MD03-2707 in the Gulf of Guinea (Figure 3.4a) [*Weldeab et al.*, 2007]. Consistent with a location east of Fan 17, the MD03-2707 Mg/Ca-SST record is roughly 1^{o}C warmer for the entire 0 to 20 kyr record, but shares the same magnitude of warming between the LGM and Holocene of ~4^{o}C. The MD03-2707 record also shows warming during H1 and indicates a slight warming across the YD. Similar trends in the deglacial temperature records in Fan 17 and the well-dated record of MD03-2707 also lend support to our age model.

III.4.2. IVF-$\delta^{18}O_{sw}$ Record

Because $\delta^{18}O_{sw}$ varies linearly with SSS [*Charles and Fairbanks*, 1990], our IVF- $\delta^{18}O_{sw}$ can be used to estimate past changes in SSS. The Fan 17 IVF-$\delta^{18}O_{sw}$ record (Figure 3.3d) shows that values during the LGM were close to the modern annual mean value of ~0.5‰. Nevertheless, our IVF-$\delta^{18}O_{sw}$ record suggests considerable variability during the period from the LGM until the start of the BA at 14.5 kyr, with a significant increase in IVF-$\delta^{18}O_{sw}$ values during H1. IFV-$\delta^{18}O_{sw}$ then steadily decreases from 0.8‰ to 0.4‰ during the BA (Figure 3.3d). After a brief increase toward more positive values during the early YD, IVF-$\delta^{18}O_{sw}$ values abruptly decrease to the lightest values of 0.0‰

Figure 3.4 Proxy Comparison Between Fan 17 and MD03-2707. Comparison of records from Fan 17 (blue) and MD03-2707 (red) in the eastern Gulf of Guinea [*Weldeab et al. 2007*]. (A) *G. ruber* Mg/Ca derived SST (^{o}C). (B) Calculated IVF-$\delta^{18}O_{sw}$. (C) *G. ruber* Ba/Ca (μmmol/mol). For both MD03-2707 and Fan 17 $\delta^{18}O_{sw}$ records we calculated ice-volume free $\delta^{18}O_{sw}$ (IVF- $\delta^{18}O_{sw}$) to account for any trend resulting from changes in continental ice volume. Increased deglacial wetness begins at 17 kyr in MD03-2707, and the nature of variability in this core is far more abrupt compared to the Niger Delta. MD03-2707 records are likely influenced mainly by Central African runoff, whereas Fan 17 records are influenced by WAM. The Holocene offset reflects the fresher conditions at MD03-2707 and the modern SSS gradient between sites. Light blue boxes mark H1 and the YD, and yellow box indicates the AHP.

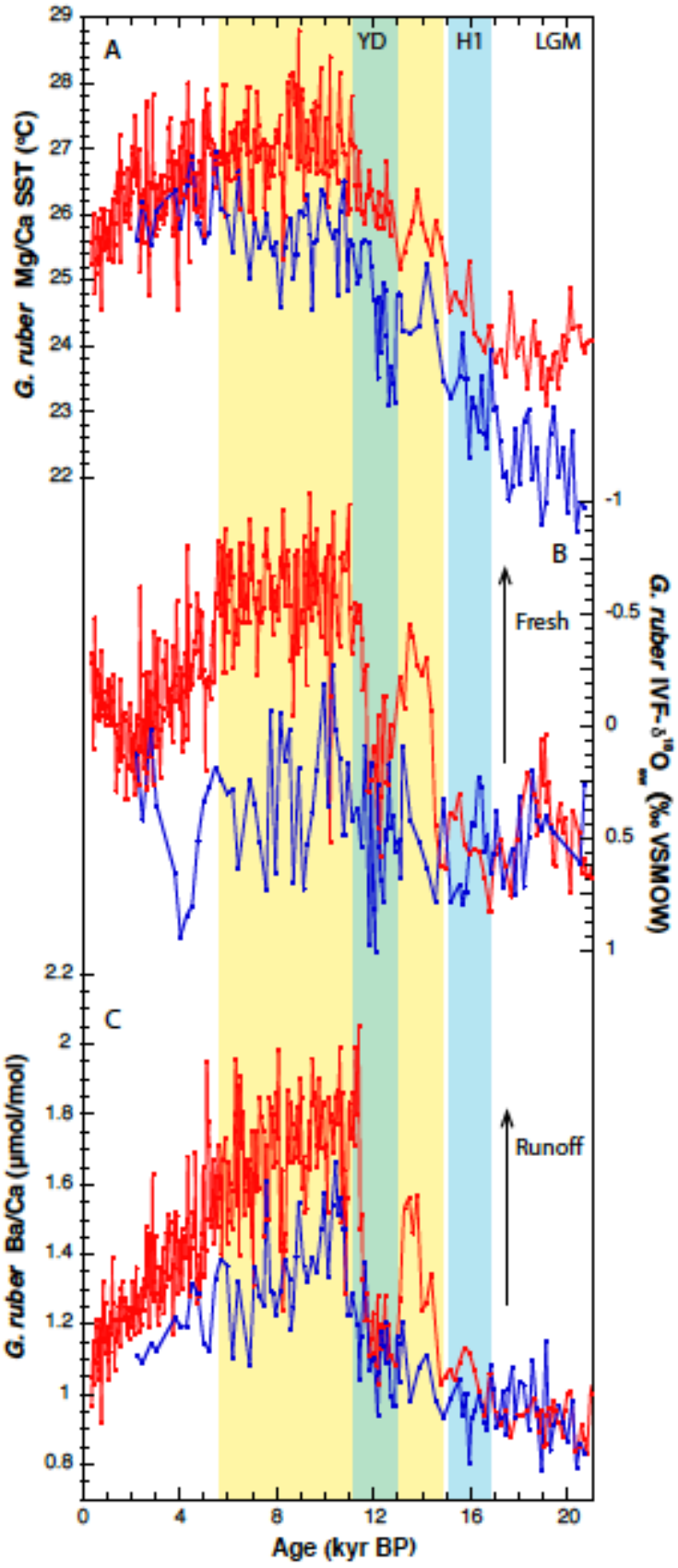
A
YD
H1
LGM
G. ruber Mg/Ca SST (°C)
29
28
27
26
25
24
23
22
B
Fresh
G. ruber IVF-δ18Osw (‰ VSMOW)
-1
-0.5
0
0.5
1
C
Runoff
G. ruber Ba/Ca (µmol/mol)
2.2
2
1.8
1.6
1.4
1.2
1
0.8
0
4
8
12
16
20
Age (kyr BP)

at 10 kyr. The Holocene record is characterized by several large oscillations of IVF-$\delta^{18}O_{sw}$ of about 1‰ (Figure 3.3d).

Next, we removed the effects of continental ice volume from the published MD03-2707 $\delta^{18}O_{sw}$ record from *Weldeab et al.* [2007] using the same deglacial record of sea level change from *Waelbroeck et al*. [2002] (Figure 3.4b). A comparison of the two records shows similar IVF-$\delta^{18}O_{sw}$ values from the LGM until H1. During H1, IVF-$\delta^{18}O_{sw}$ values in the Gulf of Guinea decrease, in contrast to the IVF-$\delta^{18}O_{sw}$ increase in the Niger Delta. At the onset of the BA, calculated IVF- $\delta^{18}O_{sw}$ values in both records become lighter, indicating fresher conditions at both sites, but the magnitude and abruptness of this freshening is far greater in MD03-2707 (Figure 3.4b). During the YD, both records once again record more positive IVF- $\delta^{18}O_{sw}$ values, suggesting an increase in regional salinity during this event. The largest offset between the two records occurs during the Holocene, where the Niger Delta values are considerably more positive than those in the Gulf of Guinea, likely due to the location of MD03-2707 in an area of lower salinity (Figure 3.1).

Although the Fan 17 IVF- $\delta^{18}O_{sw}$ record shares some similarities with the nearby record of MD03-2707, significant variability in the Fan 17 IVF- $\delta^{18}O_{sw}$ record makes it difficult to interpret with confidence. While *Charles and Fairbanks* [1990] established the linear relationship between $\delta^{18}O_{sw}$ and SSS, this relationship relies on knowledge of the regional $\delta^{18}O_{sw}$ end members. As the majority of freshwater reaching the Fan 17 site is sourced almost entirely from the Niger River, changing moisture trajectories in the past would have changed the $\delta^{18}O_{sw}$:SSS relationship. The $\delta^{18}O$ of Niger River runoff is

an integration of precipitation that falls across the large river basin with a significant latitudinal range (Figure 3.1). Moisture in this area today is sourced mainly from the EEA with moisture from temperate latitudes playing a lesser role [*Nicholson*, 2013]. However, changes in the relative contributions to rainfall from other regions, especially during cold events when northerly winds had more prominence across West Africa [*McGee et al.*, 2010], would have undoubtly changed the $\delta^{18}O$ value of Niger River runoff and thus the regional $\delta^{18}O_{sw}$:SSS relationship. In contrast, the MD03-2707 core is located near equatorial drainage basins and is also in the low salinity core of the Gulf of Guinea, thus reducing these effects. When the WAM was reduced, rainfall would have been concentrated in the southern regions of the Niger River catchment area, resulting in more positive freshwater $\delta^{18}O$ values relative to today. Also, changes in upwelling strength and duration have also been shown to cause significant deviations in local $\delta^{18}O_{sw}$:SSS relationships [*McConnell et al.*, 2009]. These complications likely contribute to the variability in our Niger Delta IVF- $\delta^{18}O_{sw}$ record, so we choose to limit interpretation of SSS change based on this record, and instead turn to the Fan 17 *G. ruber* Ba/Ca record.

III.4.3. Ba/Ca Record

In order to reconstruct the discharge history of the Niger River, we measured Ba/Ca ratios in *G. ruber* from Fan 17. The desorption of Ba^{2+} from suspended sediments in riverine water makes the $[Ba^{2+}]$ in river water much higher than in seawater. Dissolved Ba^{2+} in river water exhibits conservative mixing with seawater, resulting in a linear inverse correlation between salinity and $[Ba^{2+}]$. In addition, laboratory

experiments have shown that the incorporation of Ba^{2+} into foraminiferal calcite is linearly dependent on the [Ba^{2+}] of the water in which the shell precipitates [*Coffey et al.*, 1997]. Thus, Ba/Ca ratio in planktonic foraminifera can be used to estimate past changes of riverine input. Given the close proximity between Fan 17 and the Niger River Delta, and the river's large discharge volume, it is logical to assume that periods of elevated Ba/Ca ratios reflect increased rates of discharge from the Niger River.

The Fan 17 Ba/Ca record indicates the lowest Ba/Ca ratios of ~0.9 μmol/mol during the LGM (Figure 3.3e). Ba/Ca ratios remain relatively constant between 20 and 15 kyr (within error), oscillating around ~1.0 ± 0.1 μmol/mol. There is not a significant change in Ba/Ca values during the transition from the LGM into H1 in the Niger Delta (Figure 3.3e). At 14.8 kyr, Ba/Ca ratios begin to gradually increase from 1.0 to 1.2 μmol/mol throughout the duration of the BA. During the YD, Ba/Ca ratios show a minor decrease to ~1.1 μmol/mol (Figure 3.3e). Although previous reconstructions of paleohydrological changes in West Africa found evidence for a dramatic decrease in precipitation at the start of the YD [*Collins et al.*, 2013; *Mulitza et al.*, 2008; *Tjallingii et al.*, 2008], the Ba/Ca record from Fan 17 indicates only a minor reduction of Niger River discharge at the start of the YD. Finally, peak Ba/Ca ratios are recorded during the early Holocene at 10.5 kyr and then gradually decrease over the Holocene.

Weldeab et al. [2007] also generated a Ba/Ca record using *G. ruber* from the nearby Gulf of Guinea core MD03-2707 (Figure 3.4c). Despite being located over 400 km southeast of the nearest Niger River distributary, the MD03-2707 record was interpreted to reflect Niger River runoff and WAM variability. A detailed inspection of

modern Gulf of Guinea SSS, however, suggests that rivers draining Equatorial Africa such as the Sanaga, Ogooue, and Congo Rivers also contribute significantly to the very low salinities at MD03-2707 due to north-directed surface currents (Figure 3.1) [*Hopkins et al.*, 2013; *Jobe et al.*, 2011]. This additional freshwater causes the SSS at MD03-2707 to be fresher than at Fan 17 today. Although the Guinea Current carries a component of the Niger River plume east, it is likely that SSS in the area of MD03-2707 is influenced by a number of equatorial freshwater sources, and thus the signal reflects a combination of Equatorial African and West African Monsoon variability.

A comparison of our Ba/Ca record from the Niger Delta with the previously published Ba/Ca record from MD03-2707 (Figure 3.4c) shows both records are broadly similar, with an overall correlation coefficient of r = 0.79. As was the case with the IVF-$\delta^{18}O_{sw}$ comparison, Ba/Ca values in both records between 17-20 kyr are remarkably similar, indicating that low SSS and reduced river discharge conditions were widespread throughout the entire Gulf of Guinea and Niger Delta prior to H1 (Figure 3.4). However, the similarities break down particularly between 17.5 kyr and 13 kyr when the weakest correlation between records exists (r = 0.6; Fig. 4C). Prior to the start at H1 around 17.5 kyr, MD03-2707 Ba/Ca ratios gradually increase by +0.2 μmol/mol or ~15% of the LGM-Holocene amplitude, indicating an initial increase in riverine discharge at this location until ~ 13 kyr. In contrast, Ba/Ca ratios at Fan 17 continue to record dry, LGM-like values through H1 until 14.8 kyr (Figure 3.4). Then, beginning at the start of the AHP around 14.8 kyr and lasting until 13 kyr, Fan 17 Ba/Ca ratios steadily begin to record increased riverine discharge (+0.25 μmol/mol) across this interval. This increase

is more gradual than the transition in MD03-2707 over the same interval, where the magnitude of Ba/Ca ratio increase is twice that of Fan 17 and occurs in nearly half the time (Figure 3.4c). The responses between locations remain different during the YD as well. *G. ruber* Ba/Ca ratios in MD03-2707 abruptly decrease by 0.5 μmol/mol in less than a few centuries starting at 13 kyr, whereas Ba/Ca ratios in Fan 17 decrease only slightly at the start of the YD. Interestingly, both records once again record similar Ba/Ca values during the YD period. Following the end of the Younger Dryas, the Ba/Ca records in both cores record an abrupt increase in riverine discharge as the African Monsoon systems reached peak intensity at this time. Conditions remain fresher at site MD03-2707 for the duration of the Holocene, reflecting modern hydrographic conditions (Figures 3.1, 3.4c).

We interpret the deglacial differences between the Fan 17 and MD03-2707 Ba/Ca records as the result of riverine discharge from two different rainfall systems. We hypothesize that the Ba/Ca record from MD03-2707 does not solely reflect West African Monsoon processes. The influence of equatorial rainfall on MD03-2707 is illustrated by a comparison with the δD_{wax} humidity record from core GeoB-6518 [*Weijers et al.*, 2007] located at the Congo River outflow (Figure 3.5b). This record shows that moisture across the Equatorial African tropics, in particular the Congo Basin, began to gradually increase starting at 17 kyr [*Schefuß et al.*, 2005; *Weijers et al.*, 2007] and continued to increase until 13 kyr, when arid conditions abruptly interrupted the moisture increase (Figure 3.5b). A companion record of $\delta^{18}O_{sw}$ from the same core (GeoB-6518) also reveals a freshening of waters near the Congo River outlet starting at around 17 kyr

[*Schefuß et al.*, 2005]. Although drought conditions have been indicated across the Equatorial African tropics during H1, highlighted in particular by the desiccation of East African rift lakes [*Gasse et al.*, 2008; *Stager et al.*, 2011], these lakes lie in the region east of the Rwenzori Mountains that border The Congo and Uganda rivers. The Rwenzori Mountains constrain the location of the Congo Air Boundary where unstable air from the Congo Basin and Indian Ocean converge to produce much of the seasonal rainfall across the African Rift Valley [*Tierney et al.*, 2011]. This uniquely different set of precipitation dynamics, combined with significantly different forcing influences including Indian Ocean SST [*Tierney et al.*, 2013], most likely resulted in different rainfall patterns between the East Africa, Equatorial Congo and West African regions during H1 (Figure 3.1).

III.4.4. Regional Response to Climate Forcings

The differences between our new Niger Delta records and the previously published MD03-2707 records reveal new insights into the evolution of precipitation throughout Western and Equatorial Africa during the last deglaciation. Today, annual to decadal variability results from changes in the intensity or latitudinal extent of the rainbelt, which produces two distinct rainfall patterns between West and Equatorial Africa [*Nicholson*, 2009]. A dipole pattern results from changes in the latitudinal excursion of the rainbelt causing West Africa to dry when Equatorial Africa becomes wet, and vice versa. In contrast, both regions vary in phase with one another during changes in rainbelt intensity [*Nicholson*, 2008; *Nicholson and Grist*, 2001]. Long-term variability of these patterns stems from their sensitivity with respect to varying climatic

forcings. While both regions are likely to be influenced to some degree by changes in high latitude Northern Hemisphere climate, a recent modeling study found that greenhouse gas concentrations are especially important for precipitation across Equatorial Africa, whereas West Africa is more sensitive to Northern Hemisphere summer insolation [*Otto-Bliesner et al.*, 2014].

Dry conditions at Fan 17, MD03-2707, and GeoB-6508 during the LGM indicates that the strength of the tropical rainbelt was significantly reduced region-wide, corresponding to low [CO_2] and precessional forcing at this time (Figure 3.5a). An increase in precipitation along coastal regions of Tropical Africa and continued aridity in the WAM region across H1 suggests a possible dipole response at this time. Increasingly wet conditions across Equatorial Africa, likely responding to rising CO_2 levels by the start of H1, imply a gradual strengthening of the rainbelt during this time [*Collins et al.*, 2011]. Meanwhile, in West Africa, continued low discharge at the Niger Delta suggests that the rainbelt had not yet reached latitudes far enough North to stimulate significant rainfall across the Sahel and in the Niger River drainage basin (Figure 3.1). Similar limitations of the northward extent of the global rainbelt during H1 have been documented [*Leduc et al.*, 2009; *Peterson et al.*, 2000]. Therefore, our data would suggest the Sahara and Sahel continued to experience dry conditions similar to the LGM for the duration of H1, in spite of increased dust fluxes during this time, suggesting an intensification of drought in West Africa [*McGee et al.*, 2013; *Mulitza et al.*, 2008] (Figure 3.5c). Given the absence of any major change in West African precipitation in our new records during H1, our Niger Delta records suggest that increased wind

strength, rather than intensified drought, most likely explains the increased dust emissions from the Sahara and Sahel during H1. It is only after H1, possibly in response to Northern Hemisphere warmth during the BA and increased precessional insolation, that our new records indicate the start of an intensification of rainfall across West Africa (Fig. 5A). The delayed response of our Niger Delta records compared to those in MD03-2707 likely reflects the steady northward progression of the rainbelt's seasonal extreme in response to gradually increasing summertime insolation across this interval.

This may explain the discrepancy between the Fan 17 Ba/Ca and a recent precipitation record of δD_{wax} from Lake Bosumtwi in Southern Ghana [*Shanahan et al.*, 2015]. Unlike the Fan 17 Ba/Ca record, the Lake Bosumtwi reconstruction records a strong H1 drying relative to the LGM. However, this is not surprising because the evolution of the monsoon can be summed up into three parts: an "oceanic phase" during winter when the rainbelt is situated just north of the equator, a "coastal phase" when the rainbelt migrates over the Guinea Coast in early spring where it remains through July until the monsoon jumps to a "Sahaelian phase" in mid-July [*Thorncroft et al.*, 2011]. This jump is the result of two processes. First, the northward shift is ultimately controlled by the latitudinal temperature gradient setup across West Africa in summer, and secondly, the rainbelt remains at the coast rather than migrating inland due to the persistence of warm water along the Guinea Coast. Thus, the location of Lake Bosumtwi at 6^{o}N means it receives nearly all of its precipitation during the "coastal phase". During H1, in response to cooler Northern Hemisphere conditions, the rainbelt was locked into the oceanic phase for longer, spending less time over the Guinea Coast relative to the

Figure 3.5 Regional Monsoon Proxies and Forcings. Evolution of West and Central African hydroclimate during the last deglacial. (A) Ba/Ca records from the Niger Delta (blue) and MD03-2707 (red) with 11^{o}N summer time insolation superimposed (black). (B) δD record of Congo River Basin humidity from GeoB 6518 *Weijers et al.* [2007]. (C) % dust in core GeoB 9508 (15.29^{o}N, 17.56^{o}W) from *Collins et al*. [2013]. (D) Fan 17 total carbonate and (E) Ba/Ti. (F) EPICA Dome CO_2 *Monnin et al.* [2004] and (G) NGRIP ice core $\delta^{18}O$. Black dashed line represents the initial intensification of rainfall in MD03-2707 and Congo River Basin at the onset of increasing CO_2 levels. At the onset of abrupt Northern Hemisphere warming around 14.8 kyr, the tropical rainbelt intensifies throughout West and Central Africa, but is slow to reach maximum strength across interior West Africa as the rainbelt gradually tracks northward with increasing insolation. During the H1 and YD events, large increases in dust flux from West Africa occur (C) despite no major change in hydroclimate across this region. Increased wind strength stimulated coastal upwelling enhancing primary productivity during the H1 and YD (D,E). Wind intensification also likely drove the concurrent dust emissions during H1 and the YD.

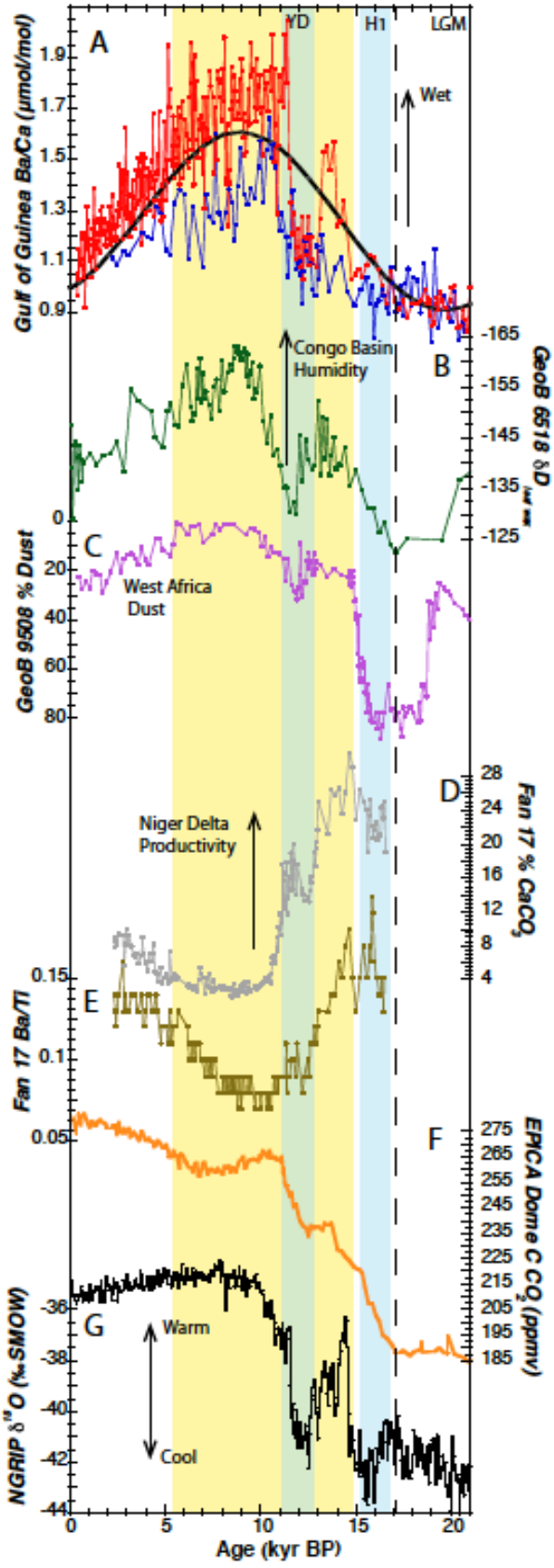
YD
H1
LGM
A
Gulf of Guinea Ba/Ca (µmol/mol)
1.9
1.7
1.5
1.3
1.1
0.9
Wet
B
Congo Basin Humidity
GeoB 6518 δD (‰ SMOW)
-165
-155
-145
-135
-125
0
C
West Africa Dust
GeoB 9508 % Dust
20
40
60
80
D
Niger Delta Productivity
Fan 17 % CaCO3
28
24
20
16
12
8
4
E
Fan 17 Ba/Ti
0.15
0.1
0.05
F
EPICA Dome C CO2 (ppmv)
275
265
255
245
235
225
215
205
195
185
G
Warm
Cool
NGRIP δ18O (‰ SMOW)
-36
-38
-40
-42
-44
0
5
10
15
20
Age (kyr BP)

LGM and causing a decrease in precipitation at Lake Bosumtwi. To the north across the Niger River Basin, the monsoon jump either failed to occur or had yet to penetrate far enough into interior West Africa that the difference in rainfall between the LGM and H1 was negligible.

III.4.5. Niger Delta Primary Productivity

At the beginning of the YD, Northern Hemisphere cooling helped to trigger a return to arid conditions and a large-scale weakening of rainbelt intensity in Equatorial Africa. While it appears that West Africa did experience some degree of drying during this time, our Niger Delta records do not suggest that the reduction in moisture was nearly as severe as it was in Equatorial Africa. Nevertheless, significant dust emissions are still associated with the YD [*McGee et al.*, 2013; *Mulitza et al.*, 2008] (Figure 3.5c). It is unlikely that the small change in aridity suggested by our Niger Delta Ba/Ca record would result in such a large change in dust flux. Instead, stronger winds during the YD likely caused the elevated dust emissions, but the magnitude of flux may have been limited by increased vegetation coverage at this time [*deMenocal et al.*, 2000].

Our elemental Ba/Ti and total carbonate data provide additional support to the role of wind-driven dust emissions during H1 and YD. Elevated Ba/Ti ratios in Fan 17 suggest increased surface productivity, as the excess rain of organic matter settling through the water column promotes the additional formation of barite in sediments relative to the terrigenous flux (inferred from Ti) [*Murray and Leinen*, 1996; *Murray et al.*, 2000]. Total carbonate content also tracks the increased rain of calcareous organisms to the seafloor during production blooms. Ba/Ti ratios and total carbonate values are

highest during H1 (Figure 3.5d and e) before decreasing during the BA. A second, albeit smaller increase occurs during the YD, followed by a second decrease to the lowest values during the early Holocene before gradually increasing at 7 kyr.

Although primary productivity around the Niger Delta is nearly constant throughout the year, productivity levels are generally low due to macronutrient limitations of phosphate and nitrate. Declining productivity corresponding to increasing river discharge starting at ~15 kyr in Fan 17 rule out Niger River discharge as a likely source of these nutrients. However, productivity does appear to correlate well with regional dust flux (Figure 3.5). Although dust alone could not provide the macronutrients necessary to stimulate excess productivity, the strong winds associated with increased dust emissions during H1 and the YD would have blown over the Niger Delta and enhanced coastal upwelling. Stronger upwelling would supply surface waters offshore of the Niger Delta with increased levels of phosphate and nitrate to fuel greater productivity. Interestingly, minimum productivity over the last 17 kyr occurs during the peak of the AHP (7-11 kyr) when conditions were the wettest, emphasizing the importance of wind-driven upwelling over river discharge in driving productivity in the Niger Delta. The gradual decline of productivity between 12.9-15 kyr relative to the abrupt decrease in dust at ~15 kyr can be likened to observations of modern dust plumes, where a cubic relationship between wind strength and dust emission demonstrates how the top wind strengths account for the majority of dust activation. Therefore, a minor change in wind strength can result in a large decrease in dust emission [*McGee et al.*, 2010].

This wind driven upwelling off the Niger Delta is likely driven by the intensification of the boreal winter Harmattan wind over the area during H1 and YD. Under modern climate conditions during boreal winter, the northeasterly Harmattan wind progressively replaces the southwesterly monsoon flow across the Sahel and Guinea coast as the rainbelt reaches its most southerly position [*Lyngsie et al.*, 2011]. The Harmattan largely contributes to the wintertime dust plume, sourcing dust mainly from the Bodele Depression, the single largest dust source in West Africa [*Washington et al.*, 2009]. Although the Bodele Depression remains active year round, maximum dust emissions occur during winter months in association with the Harmattan wind [*Washington et al.*, 2009]. Throughout H1, the intensified Harmattan wind would have lofted significantly more dust into the atmosphere while also producing longer and more vigorous upwelling, sustaining increased productivity in the Niger Delta. A similar scenario would have also characterized the YD, but vegetation reconstructions suggest that much of the Bodele Depression was largely vegetated by this time, and would not have produced similar volumes of dust [*Cockerton et al.*, 2014]. Following the YD, peak wetness and a northerly position of the rainbelt limited the influence of the Harmattan, resulting in low dust fluxes across West Africa and decreased productivity at the Niger Delta.

Upon the return of Northern Hemisphere warmth at ~11.5 kyr, peak rainbelt intensity was quickly reached in response to maximum insolation and greenhouse gas forcing, and persisted for several thousand years during the early Holocene. An abrupt decrease in Niger River discharge at ~5.7 kyr shown by Fan 17 (Figure 3.5a) is

consistent with the timing and abruptness of the AHP termination in other records from West Africa [*deMenocal et al.*, 2000; *Shanahan et al.*, 2015], whereas father to the south in MD07-2707 the end of the AHP occurs slightly later at 4.9 kyr. Furthermore, the gradual decrease in the SSS gradient between the Niger Delta and MD03-2707 during the Holocene may reflect a long-term decrease in the intensity of the rainbelt associated with decreasing insolation over this interval (Figure 3.5a).

III.5. Conclusions

Taken together with previous reconstructions of West African precipitation changes, our new deglacial records of SSS change in the Niger Delta and Niger River discharge variability suggest temporal and spatial offsets in the timing of the WAM and Equatorial monsoon systems in Central Africa. While atmospheric advection of moisture into the interior of Equatorial Africa seems to have begun at or near the start of H1, moisture delivery to the Sahel region did not initiate until after the start of the AHP at around 14.8 kyr. In addition, our findings help explain the large increase of dust emissions during H1 and the YD, suggesting that these changes were driven by elevated winds rather than intensification of drought. Therefore, this study places existing dust reconstructions in the context of changing wind and aridity conditions across West Africa and provides a new framework for interpreting dust records in West Africa. This framework decreases uncertainty in interpreting dust records that has limited climate modeling abilities to simulate the role of dust in past climate change, which often underestimates critical parameters required for forecasting the regional response of African dust to future climate change [*Evan et al.*, 2014]. Moreover, our results lend

support to the correlation between the WAM strength and summer insolation variability over longer time scales. In the future, precessional insolation will remain at near minimum values in the Northern Hemisphere tropics and thus prolonged droughts plaguing this region will likely persist or intensify. Despite this, further understanding of the causes for drought across West Africa will lead to better drought prediction and readiness for developing nations and improve the quality of life for those living in the region.

CHAPTER IV

EASTERN EQUATORIAL ATLANTIC SUBSURFACE WARMING DURING DEGLACIAL PERIODS OF REDUCED ATLANTIC MERIDIONAL OVERTURNING CIRUCLATION AND ITS RELATIONSHIP TO THE WEST AFRICAN MONSOON

IV.1. Introduction

As Earth began to warm after the Last Glacial Maximum (LGM) around 20 kyr ago, two sudden cold reversals interrupted the deglacial-warming trend. These events, known as Heinrich Event 1 and the Younger Dryas, are associated with a return to glacial conditions in many parts of the Northern Hemisphere, gustier winds, and increased dust in the atmosphere across the globe [*Mulitza et al.*, 2008; *Peterson et al.*, 2000; *Wang et al.*, 2001]. Central to understanding the cause of these cold reversals is the Atlantic Meridional Overturning Circulation (AMOC), which transports large amounts of heat between hemispheres [*Kuhlbrodt et al.*, 2007]. Evidence suggests that during the two cold events, melting ice sheets altered the density of waters in the North Atlantic leading to a reduction in the strength of AMOC and its associated northward heat transport [*Clark et al.*, 2001; *Menviel et al.*, 2011; *Rahmstorf*, 2002; *Thornalley et al.*, 2010]. The reduced heat transport into the Northern Hemisphere during Heinrich 1 and the Younger Dryas steepened meridional temperature gradients causing a southward

shift of the Intertropical Convergence Zone (ITCZ), leading to abrupt changes in the hydrologic cycle throughout South America, China, and the Indo-Pacific [*Kanner et al.*, 2012; *Partin et al.*, 2007; *Wang et al.*, 2001]. Across West Africa however, a breakdown in the land-sea thermal gradient in response to changing ocean circulation patterns likely contributed to a weaker monsoon in this region.

Based on water-hosing experiments, *Zhang* [2007] showed that the subsurface of the tropical North Atlantic (between 200-600m) warms when AMOC is weakened. The mechanism for this subsurface warming was later examined in a coupled GCM by *Chang et al.* [2008] and *Schmidt et al.* [2012b] who identified a two-step process involving reorganizations of upper and intermediation ocean circulation. First, weakening of AMOC causes a rapid reduction in the strength of the western boundary current as a wave adjustment process, producing warming of the subsurface due to the reduced transport of cooler subsurface tropical waters into the Caribbean. Then, after AMOC weakens beyond a threshold, the equatorward pathway of the North Atlantic subtropical cell (which today is blocked by the strong northward return flow along the western boundary) opens and allows the salinity maximum waters of the subtropical North Atlantic gyre to flow south into the equatorial zone [*Fratantoni et al.*, 2000; *Hazeleger and Drijfhout*, 2006; *Jochum and Malanotte-Rizzoli*, 2001; *Kirchner et al.*, 2009], intensifying the subsurface warming. *Chang et al.* [2008] theorized that once these waters enter the equatorial zone, they warm the Eastern Equatorial Atlantic (EEA) cold tongue, reducing the land-sea temperature gradient critical to West African Monsoon development.

Existing records of West African Monsoon variability during the last 20 kyr appear to support this hypothesis. Extreme drought conditions have been interpreted to be pervasive features of West African climate during Heinrich 1 and the Younger Dryas. An abrupt southward expansion of the Sahara has been documented during Heinrich Events [*J A Collins et al.*, 2013] and reconstructions of dust, pollen and grain size analysis from marine sediments all point to widespread droughts throughout the Sahara and Sahel during these events [*Itambi et al.*, 2009; *McGee et al.*, 2013; *Mulitza et al.*, 2008; *Tjallingii et al.*, 2008]. Yet records from the Gulf of Guinea, where low sea-surface salinity (SSS) is believed to be the result of large amounts of freshwater runoff from the WAM, do not provide evidence for drought-like conditions at Heinrich Event 1. For example, during Heinrich 1, reconstructed SSS based on planktonic foraminiferal Ba/Ca ratios does not show an increase of SSS relative to the LGM that would indicate an intensification of drought in West Africa during this time [*Weldeab et al.*, 2007]. Furthermore, a record of reconstructed Niger River discharge indicates no decrease in river runoff during Heinrich Event 1 relative to the LGM, suggesting similar conditions existed in the region until the onset of the Bölling-Alleröd at 14.5 kyr [*Parker et al*. 2016]. *Parker et al*. [2016] also found that following Heinrich Event 1, Niger River discharge steadily increased during the latter half of the deglacial suggesting that the onset of the WAM across the Sahel was far more gradual than previously thought. Given the influential role AMOC may have on EEA temperature gradients, further investigation of the AMOC-monsoon relationship is warranted.

In this paper, we present new proxy data and model simulations exploring the subsurface dynamics in the EEA during an AMOC slowdown and its relationship to the WAM. We first present high-resolution Mg/Ca records of subsurface temperature variability during the deglacial in core Fan 17 in the EEA using the deep-dwelling planktonic foraminifera *Globorotalia crassaformis*. This subsurface temperature record reveals large and abrupt increases in subsurface temperature coincident with the onset of Heinrich Event 1 and the Younger Dryas. Our new time slice simulations across the Younger Dryas using the CCSM3 also suggest that subsurface temperatures in the EEA can rapidly warm at the onset of an abrupt weakening of AMOC. We then compare this record of subsurface temperature with records of monsoon variability to evaluate the impact of subsurface temperatures on the WAM.

IV.2. Oceanographic Setting

Sediment core Fan 17 (4.81^{o}N, 4.45^{o}E, 1178m) was recovered equidistant (~100 km SW) from the two major distributaries of the Niger River Delta in the far EEA (Figure 4.1) along a SSS gradient set up between the low salinity waters in the Gulf of Guinea and higher salinity equatorial waters. Mean annual SSS is 33.4, ranging from a maximum of 34.5 during the dry winter season and a minimum of 32 during the wet summer months [*Antonov et al.*, 2010]. Fresh water at the Fan 17 site is sourced entirely from runoff of the Niger River, and the magnitude of this discharge has been show to directly correlate with the strength of the West African Monsoon [*Itiveh and Bigg*, 2008]. SSTs in this region are warm, with a mean annual of 27.8^{o}C and less than 1^{o}C of seasonal variability (Figure 4.1).

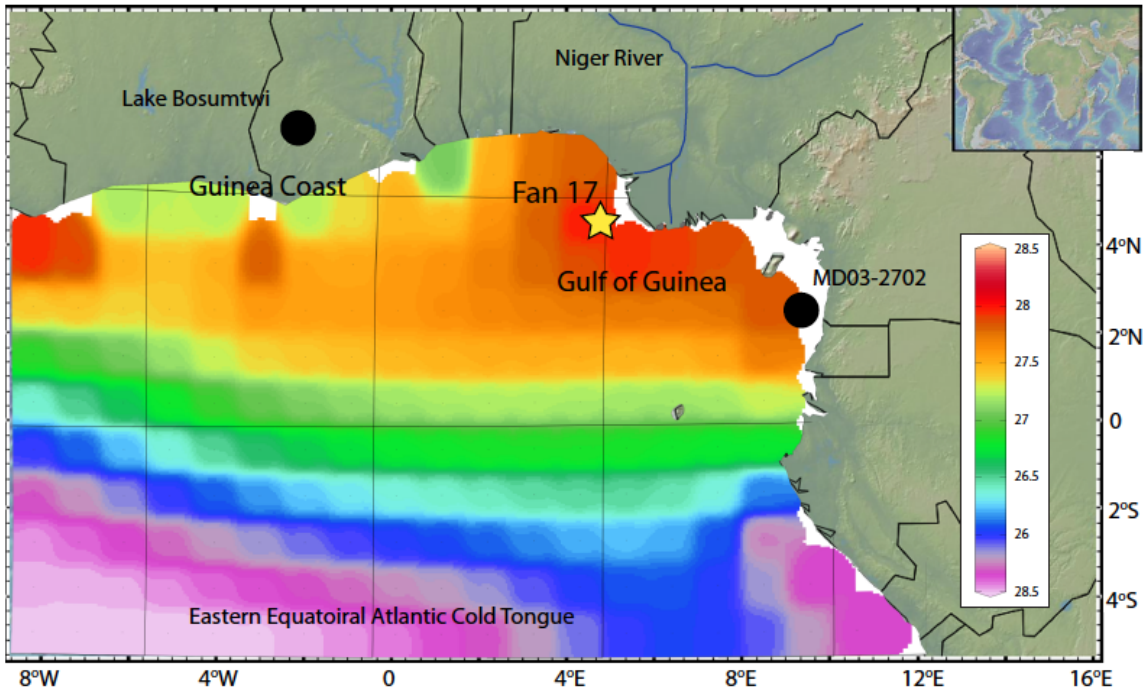

Figure 4.1 Gulf Of Guinea Hydrography: Regional map of the Eastern Equatorial Atlantic with locations of Fan 17 (yellow star) and the nearby core locations of MD03-2707 and Lake Bosumtwi (*Shannahan et al*. 2015; *Weldeab et al*. 2007; black dot). Shaded colors represent mean annual SST. South of the Equator cool SST's represent the EEA cold tongue caused by the northward migration of the SE trades during summer. Cool SST along the Guinea coast represent the associated coastal upwelling cell that extends east toward the Niger Delta. Surface waters in the Gulf of Guinea are exceptionally fresh and warm and therefore the surface expression seasonal coastal upwelling is not seen.

Today, subsurface conditions around the Niger Delta are characterized by a shallow thermocline, although very little modern observations of the subsurface are available from this region (Figure 4.2). Inter-annual variability affects the upper ~120 m of the water column with very little variability below this depth. Temperatures between 200-600 m, where our Younger Dryas time slice simulations that will be described in the following section suggest maximum subsurface warming occurs at the onset of AMOC weakening, ranges from 14 to 8.5^{o}C, respectively. During the summer months, the thermocline shoals when coastal upwelling is initiated. Upon the development of the monsoon flow, intense upwelling develops in the equatorial cold tongue as well as the Guinea Coast from Benin to western Nigeria [*Jouanno et al.*, 2011; *Kouadio et al.*, 2013]. Although remote sensing imagery and mean SST do not show a robust coastal upwelling cell along the Niger Delta (Figure 4.1), it is likely that the sharp halocline of the freshwater pool conceals the surface expression of upwelling in this region. A study by *Rider* [2004] looked at several vertical profiles of temperature taken over the course of one year around the Niger Delta and concluded that the thermocline shoals as expected during upwelling season.

To reconstruct subsurface conditions, we use the deep-dwelling planktonic foraminifera *G. crassaformis.* This species is usually regarded as a lower thermocline to sub-thermocline species living between 400-600m water depth in the Atlantic [*Regenberg et al.*, 2009; *Steph et al.*, 2009]. However, it has been shown to live significantly shallower in the EEA, around 200-350 m [*Schmuker and Schiebel*, 2002] (Figure 4.2). This is likely due to the influence of strong upwelling systems and shallow

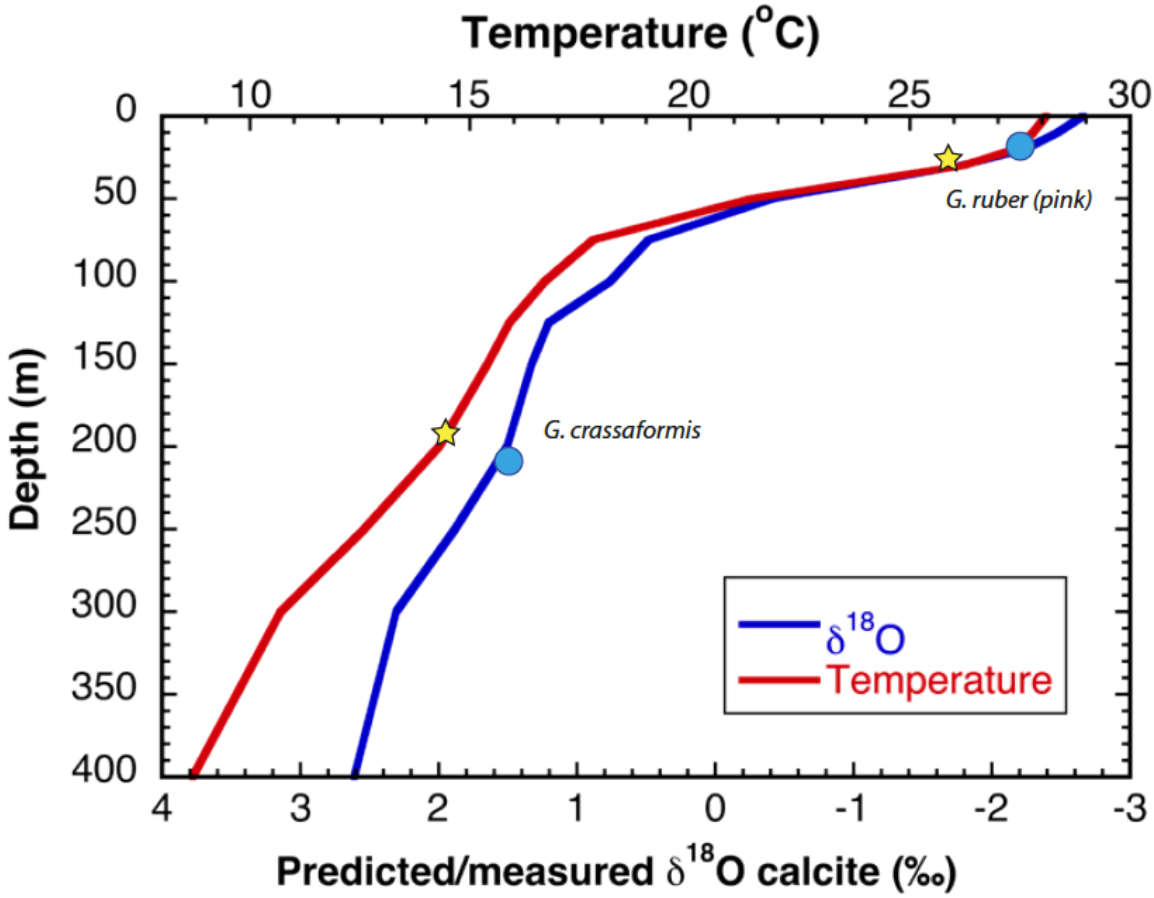

Figure 4.2 Niger Delta Thermocline: Modern thermocline at the Fan 17 location (red line) was constructing using WOCE data and ODV4. Predicated $\delta^{18}O_c$ (blue line) calculated following the steps outlined in *Steph et al*. [2009]. Plotted are the core top Mg/Ca temperature calculations for *G. ruber* and *G. crassaformis* (yellow star) as well as core top $\delta^{18}O_c$ values (blue dot). Core top SST for *G. ruber* is consistent with a habitat depth in the upper most mixed layer while *G. crassaformis* temperature is consistent with a habitat in the lower thermocline. Core top $\delta^{18}O$ is plotted against the predicted/measured $\delta^{18}O$ from *Steph et al.* [2009] for Eastern Atlantic locations. For both species, the $\delta^{18}O_c$ values are consistent with core top temperature estimates and habitat depths. The lower thermocline depth range of *G. crassaformis* is ideal for recording subsurface warming related to the weakened AMOC mechanism.

thermocline in this region. Furthermore, a study by *Tedesco et al.* [2007] showed a similar shoaling of *G. crassaformis's* habitat depth in a similar upwelling system in the Caribbean.

IV.3. Materials and Methods

IV.3.1. Core Collection and Chronology

TDI Brooks recovered Fan 17 in 2007 as part of a larger coring initiative for Shell International, and donated the core to the Department of Oceanography at Texas A&M University for research where it is stored in the Department's core repository. The age model for Fan 17 was previously published in Parker et al. (2016) and was developed using 11 radiocarbon-dated intervals of mono-specific *G. ruber* specimens. Radiocarbon ages were then converted to calendar years using the CALIB 7.1 program and a standard marine reservoir age correction of 400 years [*Stuiver et al.*, 2013]. The resulting ages spanned 1 - 39 kyr with 6 dates constraining the Holocene and deglacial section of our records (Figure 4.3). Using linear interpolation between calibrated dates, our age model yields a nearly linear sedimentation rate of 16.5cm/kyr during this time (Figure 4.3). Based on our age model, we sampled the upper 330 cm of core material corresponding to a 120 year/sample temporal resolution.

A record of *G. ruber* Mg/Ca SST from Fan 17 was recently published by *Parker et al*. [2016] and closely resembles a similar high-resolution record of SST from a nearby Gulf of Guinea core [*Weldeab et al.*, 2007]. Both SST records from the EEA gradually warm beginning after the LGM and continue to warm during Heinrich Event 1. In a similar manner to Greenland, warming accelerates at 14.5 kyr

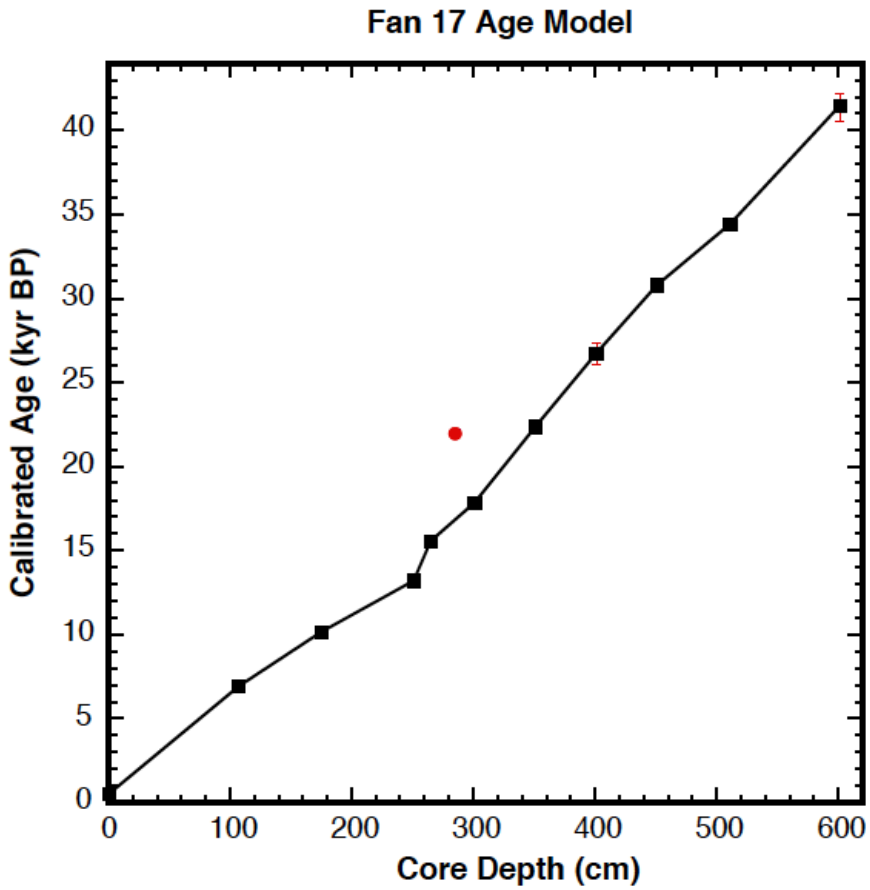

Figure 4.3 Age Model: 11 radiocarbon dates constrain the age model for Fan 17. Radiocarbon ages were converted to calendar age using CALIB 7.1 [*Stuvier et al*. 2013]. The calibrated ages span 1-39 kyr with 6 dates constraining the deglacial section of our record. An age reversal at 285 cm (red dot) was not used in the calculation of our age model.

until it is interrupted at the beginning of the Younger Dryas. At ~12.9 kyr, both records record a 1-1.5^{o}C SST decrease. Warmest temperatures occur during the early to middle Holocene when both records converge to record nearly identical temperatures during the late Holocene. The close similarity between our record, the well-dated record of *Weldeab et al.* [2007], and Greenland ice core records lends further confidence to the fidelity of our radiocarbon age model for Fan 17.

IV.3.2. Stable Isotopes

In order to better constrain the depth habitats of *G. ruber* and *G. crassaformis* in the Niger Delta region, we measured the oxygen isotope composition of *G. ruber* and *G. crassaformis* from the Fan 17 core top sample. We compared this data with predicted $\delta^{18}O_c$ for water depths between 0-1000 m in the EEA calculated using annual and seasonal hydrographic data from NODC 2001 [*Conkright et al.*, 2002; *Steph et al.*, 2009]. In order to limit ontogenetic and growth rate effects, 15-20 *G. ruber* (250-355 μm) and 7-10 *G. crassaformis* (355-425 μm) were sonicated in methanol and analyzed uncrushed using a Thermo Scientific MAT 253 IR-MS with Automated Kiel IV Carbonate Device at Georgia Institute of Technology. The raw $\delta^{18}O$ values were standardized using NBS-19.

IV.3.3. Mg/Ca Analysis and Calibrations

Trace metal analyses were performed on ~580 μg of *G. crassaformis* calcite (7-10 *G. crassaformis* shells) from each sample. We followed the cleaning procedures of *Schmidt et al.* [2012a], which involved crushing and homogenizing the samples, methanol sonication to remove clay particulates, a reduction step to remove metal oxides

and an oxidation step to remove organics. The samples were measured at Texas A&M on a Thermo Scientific Element XR Inductively Coupled Plasma Mass Spectrometer using isotope dilution methods.

Mg/Ca ratios are a well-studied and widely used tool for reconstructing past ocean temperatures. The substitution of Mg into foraminiferal calcite is endothermic and thus favored at higher temperatures [*Barker et al.*, 2005]. Calibration studies have consistently demonstrated that temperature is the primary control of Mg/Ca ratios in foraminiferal calcite [*Anand et al.*, 2003; *Dekens et al.*, 2002; *Honisch et al.*, 2013]. Despite a recent study that suggested salinity had a much largest effect than previously thought [*Arbuszewski et al.*, 2010], *Hertzberg and Schmidt* [2013] showed that this conclusion was likely based on an the incorrect application of a dissolution –corrected calibration equation to calculate Mg/Ca SSTs. This highlights the importance of carefully selecting an appropriate Mg/Ca-SST equation based on the preservation condition of foraminiferal samples [*Regenberg et al.*, 2014]. At Fan 17, visual inspection of the foraminifera and the measurement of nearly constant shell weights on all our samples suggest the shell material used in this study has not be subjected to significant dissolution. Therefore, we choose the species specific *G. crassaformis* equation from *Anand et al* [2003] to convert Mg/Ca ratios to calcification temperatures:

(1) *G. crassaformis:* $Mg/Ca = 0.339 \exp(0.09*T)$ (error $\pm 0.5^{o}C$).

For *G. crassaformis*, equation (1) gives a core top value of $13.7^{o}C$, which is consistent with modern temperatures at ~250 m depth (Figure 4.2).

The long-term analytical reproducibility based on a matrix-matched standard analyzed through the study was 1.13% for Mg/Ca. The pooled standard deviation for *G. crassaformis* sample replicates was 8.0% (df=101) based on 110 intervals. We combined the calibration error of the temperature equation (1) with the analytical error from the Mg/Ca measurements to calculate a 1σ error of the *G. crassaformis* temperature estimates of ± 1.9°C. To calculate the error on the smoothed temperature record we used the following equation: $\sigma_{combined} = \sigma_{analytical} + \sigma_{calibration} / \sqrt{n}$ where "n" equals the number of points used in the smoothing function. This yielded an error estimate on the smoothed *G. crassaformis* temperature record of ±1.09°C.

IV.3.4. YD Time Slice Simulation

Liu et al. [2009] conducted a transient climate simulation of the last deglaciation using a low-resolution version of CCSM3 [*W D Collins et al.*, 2006], comprised of a T31 (approximately 3.75° horizontal resolution) CAM3 with 26 hybrid coordinate levels in the vertical and a 3°x3° POP with 25 vertical z-coordinate levels. An examination of this simulation (Figure 4.4b) reveals no significant subsurface warming in the western Tropical North Atlantic and Southern Caribbean region during the Younger Dryas, which is at odds with the paleo proxy evidence [*Schmidt et al*., 2012b] supported by high-resolution water-hosing experiments [*Chang et al*., 2008; *Schmidt et al*., 2012b]. We argue that this discrepancy is partially attributable to the coarse resolution of the ocean model, which does not properly resolve western boundary current dynamics and thus does not accurately represent the regional ocean circulation changes that are

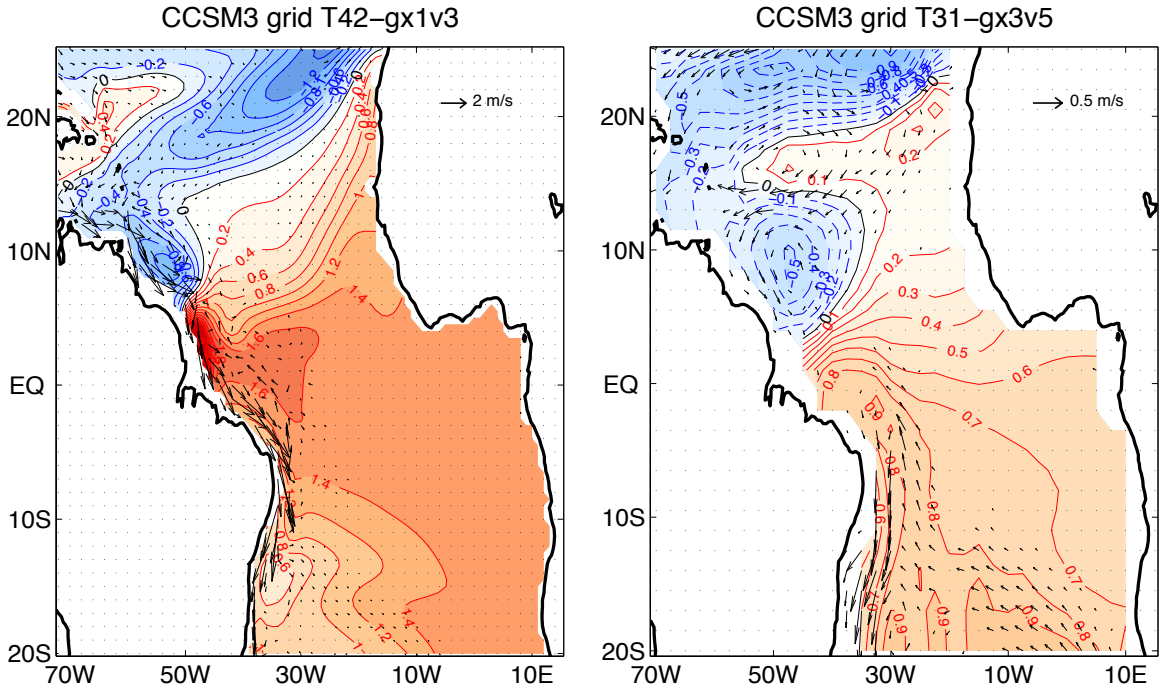

Figure 4.4 Difference between High and Low Resolution CCSM3 Simulations: Changes in Temperature and Velocity at 12. 6 kyr averaged between 200 and 275m relative to 12.9 kyr in the T42x1 CCSM3 simulation (this study) and the T31x3 CCSM3 [*Liu et al*., 2009] simulation. Changes in AMOC in the higher resolution T42x1 CCSM3 model produces a strong response between 200 and 275 m along the western boundary and equatorial zones consistent with the oceanic teleconnection mechanism proposed by Chang et al., [2008] and Schmidt et al., [2012b]. The lower resolution AMOC, T42x1 CCSM3 simulation reveals little warming in these critical areas.

crucially important for the subsurface warming mechanism as shown in *Chang et al*. [2008] and *Schmidt et al*. [2012b].

To remedy the problem, we conducted a time-slice simulation of the Younger Dryas using a relatively high-resolution version of CCSM3 that consists of T42 (approximately 2.8° horizontal resolution) CAM3 with the same vertical levels as the T31 version and 1°x1° POP with 40 vertical levels (hereafter referred to as T42x1 CCSM3). This version of CCSM3 has been used by *Otto-Bliesner and Brady* [2009] to conduct a set of water hosing experiments under LGM forcing boundary conditions. The results show a major reduction in Florida Straits transport of ~10 Sv accompanied by an AMOC reduction of ~11 Sv, which is consistent with the reconstructed Florida Current transport across the Florida Straits during the most recent Heinrich Event and the Younger Dryas [*Lynch-Stieglitz et al.*, 2011]. A similarly configured POP was also used as the ocean component of the NCAR CESM1 and CCSM4 model participated in the latest IPCC climate simulations. A recent study by *Danabasoglu et al.* [2014] shows that when forced with observationally based atmospheric surface fluxes the model reproduces well the observed mean AMOC depth profile at 26.5°N derived from the 4-year mean RAPID data. Collectively, these previous studies give us some confidence that the 1°x1° POP is able to significantly improve western boundary current dynamics and the AMOC over the low-resolution counterpart, making it more suitable for studying the oceanic teleconnection mechanism described by *Chang et al*. [2008] and *Schmidt et al*. [2012b].

The Younger Dryas time-slice simulation begins from a T42x1 CCSM3 paleo climate simulation forced by the climate boundary conditions of 15 kyr BP with a CO_2 concentration of 214 ppmv, CH_4 at 350 ppbv [*Loulergue et al.*, 2008; *Petit et al.*, 1999], and a reconstructed Laurentide Ice Sheet and closed Bering Strait (see *Hu et al.* [2015] for detail). The 15 kyr BP run is chosen as the initial condition because it is sufficiently close to the onset of the Younger Dryas. Initializing T42x1 CCSM3 with a restart file from the 15 kyr BP control run conducted by *Hu et al*. [2015], we first spin up the model for 180 years with the same climate boundary conditions used by *Hu et al*. [2015]. We then changed the climate boundary conditions to those corresponding to 13 kyr BP, including the orbital parameter, green house gas (GHG) concentrations and ice sheets with closed Bering Strait, and integrated the model for 240 years. This run was followed by another 200-year simulation with freshwater input in Weddell Sea vicinity between 60°S -80°S and 70°W-30°E and Ross Sea vicinity between 60°S-80°S and 140°E-140°W at a rate of 1.16m/200years. Our Younger Dryas transient simulation was based on these spin-up runs and integrated for 1,400 years from 12.9 kyr BP to 11.5 kyr BP with closed Bering Strait. During the transient run, the climate boundary conditions, including orbital parameters, GHG concentration, ice sheets, freshwater forcing, etc., were continuously adjusted in a manner that follows closely to the approach used by *Liu et al.* [2009] in their last deglaciation transient climate simulation. In particular, a freshwater forcing was added to the high-latitude North Atlantic between 30°N-60°N and 90°W-50°W to mimic the effect of melt water discharge from the St. Lawrence River during the Younger Dryas when the Laurentide Ice Sheet retreated northward out

of the Great Lakes. The rate of the freshwater input varies during the simulation in accordance with *Liu et al.* [2009] with a value of 14m/kyr from 12.9 to 12.5 kyr BP, 25m/kyr from 12.5 to 12.3 kyr BP, 6m/kyr from 12.3 to 11.9 kyr BP, and 12m/kyr from 11.9 kyr to 11.5 kyr (Figure 4.5b).

IV.4. Results

IV.4.1. Foraminifera Habitat Depth

In order to better constrain the depth habitat of *G. crassaformis* at Fan 17, we measured $\delta^{18}O_c$ of specimens from the core top sample with an estimated age of 2.23 kyr. We then combined this with the *G. crassaformis* core top Mg/Ca to calculate predicted water column $\delta^{18}O$ following the steps laid out by *Steph et al.* [2009]. For comparison, we also measured the core top $\delta^{18}O_c$ value of the near-surface dwelling planktonic foraminifera *G. ruber*. The core top $\delta^{18}O_c$ values of *G. ruber* and *G. crassaformis* were -2.25 ‰ and 1.33 ‰ respectively. For *G. ruber,* the predicted $\delta^{18}O$ at 0m is -2.65 ‰, which is significantly lighter than the *G. ruber* specimens analyzed in our study. This very light predicted $\delta^{18}O$ value is not all that surprising given the warm and fresh conditions that characterize the EEA. Instead, our measured $\delta^{18}O_c$ of -2.25 ‰ is nearly identical to the predicted $\delta^{18}O$ value of -2.24 ‰ at 30 m water depth. This is also consistent with the calculated core top Mg/Ca temperature of 25.6^{o}C at 30 m depth (Figure 4.2)

Comparison of our *G. crassaformis* $\delta^{18}O_c$ core top with the predicted/measured $\delta^{18}O$ places the depth habitat of this species at ~200 m in the Niger Delta region (Figure 4.2). Given the core top Mg/Ca temperature that places the habitat depth of

Figure 4.5 Niger Delta AMOC Regression: Younger Dryas time slice simulation averaged between 200-270 m. A) Regression map of simulated temperature against an AMOC index defined by the maximum value of overturning streamfucntion. Negative correlations south of ~10^{o}N indicate a warming response to weakening AMOC. Black box is the limits for the time series average in B. B) Temperature time series in blue, and AMOC index in red for entire simulation period between 12.9 and 11.6 kyr BP for the Niger Delta region. A strong negative correlation is seen between AMOC strength and the Niger Delta subsurface. Interestingly, the modeled increase in AMOC and decrease in subsurface temperature between 12.3 and 11.9 kyr is also recorded in the reconstructed *G. crassaformis* subsurface temperature record.

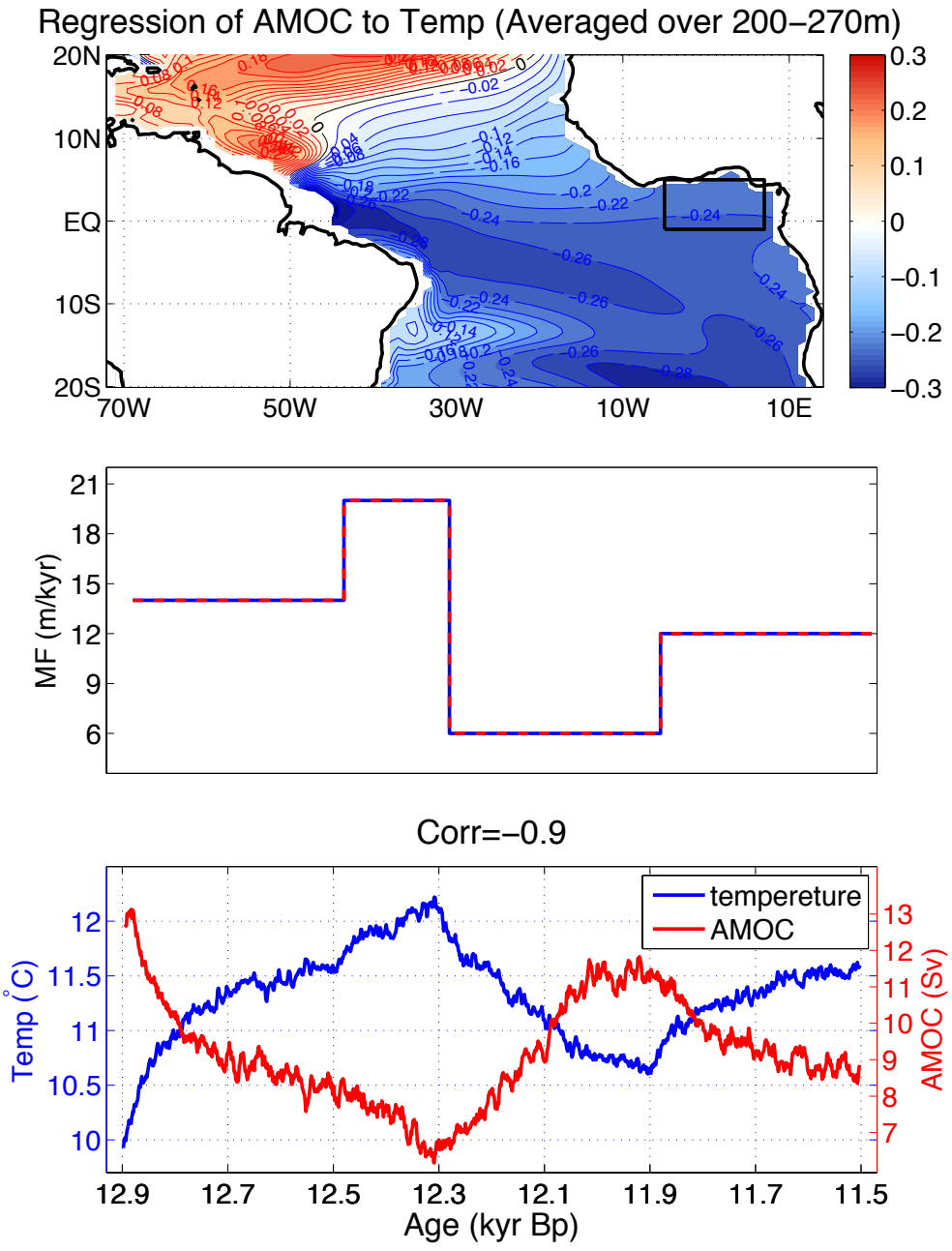
Regression of AMOC to Temp (Averaged over 200–270m)
20N
10N
EQ
10S
20S
70W
50W
30W
10W
10E
0.3
0.2
0.1
0
−0.1
−0.2
−0.3
MF (m/kyr)
21
18
15
12
9
6
Corr=−0.9
tempereture
AMOC
Temp (°C)
AMOC (Sv)
12
11.5
11
10.5
10
13
12
11
10
9
8
7
12.9
12.7
12.5
12.3
12.1
11.9
11.7
11.5
Age (kyr Bp)

G. crassaformis at 250 m with respect to the modern thermocline, we are confident that the *G. crassaformis* at our study site in the Niger Delta is living at a depth consistent with previously document depth preferences of the same species in upwelling systems at ~250 m, at least for the Holocene [*Tedasco et al*. 2007]. Nevertheless, deep dwelling foraminifera have been known to migrate vertically in the water column through time [*Cleroux et al.*, 2007; *Cleroux et al.*, 2009]. Even if *G. crassaformis* migrated to a deeper, more commonly cited depth of 400-600m [*Steph et al.*, 2009], it should still be within the range of subsurface warming in the EEA associated with an abrupt decrease in AMOC strength, according to the modeling results of the Younger Dryas time slice simulation (see modeling results below).

IV4.2. Subsurface Temperature Record

The *G. crassaformis* Mg/Ca record of subsurface temperature suggests numerous abrupt increases during the deglaciation. Throughout the record, there are significant increases in *C. crassaformis* Mg/Ca ratios at 17.5, 16.1, 12.9, and 11.9 kyr. The first abrupt warming at 17.5 kyr is indicated by an increase in Mg/Ca ratios from 0.9 to 1.2 mmol/mol, which equates to about 1.5^{o}C of warming based on equation (1). Then, the warming trend continues, reaching a maximum Mg/Ca ratio of 1.4 mmol/mol by the end of H1 at 15 kyr. The total warming over the period from 17.5-15 kyr period is equal to ~4^{o}C based on equation (1) (Figure 4.6b). At the start of the Bølling Allerød (BA) at 14.5 kyr, Mg/Ca ratios abruptly decrease by 0.4 mmol/mol , suggesting the BA was characterized by cooler subsurface conditions. These relatively cool subsurface conditions persist until another abrupt increase in Mg/Ca ratios of 0.5 mmol/mol (+3^{o}C)

Figure 4.6 G. Crassaformis Results: Fan 17 Mg/Ca records for the deglacial. (A) *G. ruber* Mg/Ca from *Parker et al*. [in review]. Dark and thick blue line represents the weighted 3-point mean of the data represented by the thin light blue line. (B) Fan 17 *G. crassaformis* Mg/Ca for the last 21 kyr. Purple dots represent the raw Mg/Ca data and grey shaded area represents the analytical error of the Mg/Ca measurements based on a smoothed three-point mean. Plotted on both Mg/Ca axes is the corresponding temperature scale for the given range of Mg/Ca calculated using Mg/Ca-temperature equations from *Anand et al*. [2003]. (C) NGRIP ice core record from Greenland [*Andersen et al*. 2004]. Over all warming in the *G. ruber* record is on the order of 4^{o}C and rises steadily throughout the deglacial accept for a brief cooling during the Younger Dryas. *G. crassaformis* however, records increased Mg/Ca (warming) during Heinrich Event 1, at the beginning of the Younger Dryas, and during the end of the Younger Dryas. Red triangles along the x-axis mark the calibrated radiocarbon dates used in the age model.

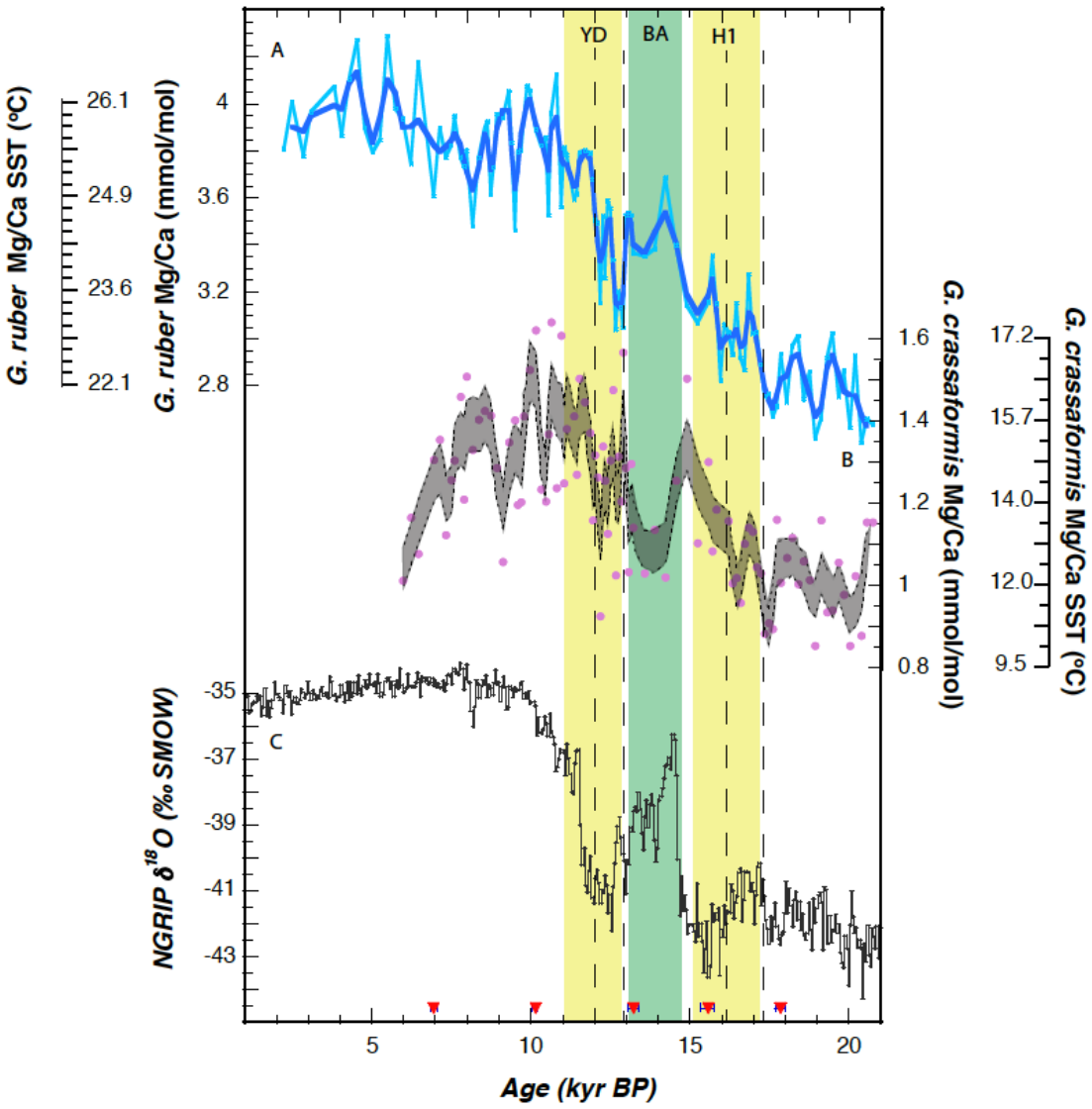
A
YD
BA
H1
B
C
G. ruber Mg/Ca SST (°C)
26.1
24.9
23.6
22.1
G. ruber Mg/Ca (mmol/mol)
4
3.6
3.2
2.8
G. crassaformis Mg/Ca (mmol/mol)
1.6
1.4
1.2
1
0.8
G. crassaformis Mg/Ca SST (°C)
17.2
15.7
14.0
12.0
9.5
NGRIP δ18O (‰ SMOW)
-35
-37
-39
-41
-43
5
10
15
20
Age (kyr BP)

occurs at the onset of the YD around 13 kyr. Interestingly, this warming begins to diminish relatively quickly during the first half of the YD, until a second abrupt warming occurs at 11.9 kyr , midway through the YD . The subsurface record then remains warm for the duration of the early Holocene before cooling again at ~7 kyr.

IV.4.3. Model Results

The simulated AMOC has a maximum of ~13 Sv at the start of the transient simulation (12.9 kyr BP) (Figure 4.5c). This value is considerably higher than the corresponding value of the coarse resolution CCSM3 last deglaciation transient climate simulation by *Liu et al.* [2009], which was around 8 Sv. The AMOC strength then decreases to a minimum value of ~ 6.5 Sv at 12.3 kyr BP, compared to the lowest value of ~4.5 Sv in Liu et al's simulation during the same period (not shown). Consistent with the stronger change in the AMOC, T42x1 CCSM3 also produces more extensive surface cooling in the North Atlantic sector than T31x3 CCSM3 run. The YD time slice run also produces a surface warming of ~0.2-0.4°C averaged over the entire YD period (in reference to 12.85 kyr BP) in the tropical Atlantic, while in the last deglaciation transient climate simulation no such surface warming was observed. Along with the surface warming, there is a more significant increase in precipitation over the Gulf of Guinea in the YD time slice run than in the last deglaciation transient climate simulation.

However, the most significant difference between the two simulations occurs in the subsurface temperature response. The YD time slice simulation produces a much more pronounced subsurface temperature response to AMOC changes than the coarse resolution CCSM3 last deglaciation transient climate simulation by *Liu et al.* [2009]. In

the YD time slice run, a strong subsurface warming of ~3°C averaged between 200m and 275 m is found along the western boundary near the gyre boundary of the tropical and northern subtropical gyres a few hundred years into the transient run (Figure 4a). Accompanied with the warming is a strong reduction in the North Brazil Current (NBC) and a broad subsurface warming of 1.2°C -1.4°C along the equatorial waveguide. This subsurface response pattern is consistent with the oceanic teleconnection mechanism by *Chang et al*. [2008] and *Schmidt et al*. [2012b]. In contrast, the coarse resolution CCSM last deglaciation transient climate simulation shows no evidence of the strong subsurface warming along the western boundary and the equatorial warming is considerably weaker than that in the YD time slice (Figure 4.4b). These findings point to the importance of resolving western boundary current dynamics in simulating AMOC-induced tropical climate response and suggest strongly that T42x1 CCSM3 is more suitable for simulating tropical response to AMOC slowdowns.

Figure 4.5a shows a regression map of the simulated temperature averaged between 200 - 270 m against an AMOC index defined by the maximum value of overturning streamfunction in the North Atlantic. It is evident that in the region south of 10°N, the subsurface temperature varies in opposite phase to the AMOC, i.e., a weakened AMOC leads to an increase in the subsurface temperature. The strongest surface temperature response occurs along the NBC and equatorial waveguide, as expected from the oceanic teleconnection mechanism described by *Chang et al*. [2008] and *Schmidt et al*. [2012b]. Along the northern Guinea coast where the proxy records are reconstructed, the regression coefficient has a value of ~0.2°C/Sv (see black box on

Figure 4.5a). To compare directly with the proxy records, we derived a subsurface temperature time series by averaging the simulated temperature from 200 m - 270 m over the region indicated by the rectangle in Figure 4.5a. Figure 4.5c shows the temperature time series (blue) along with the simulated AMOC index (red) during the entire transient simulation period. The anti-correlation between the two time series is clearly seen. As the AMOC strength decreases rapidly in the early stage of the YD from 12.9 kyr BP to 12.3 kyr BP, the subsurface temperature undergoes a rapid warming of ~2°C and reaches a maximum value of nearly 9°C at 12.3 kyr BP from its initial value of 7°C at 12.9 kyr BP. This initial warming at the onset of the YD is consistent with the reconstructed subsurface temperature record from Fan 17. Also consistent with the proxy record, there is a decrease in the subsurface temperature following the peak warming in response to a strengthening in the AMOC midway through the YD. The second warming begins at 11.9 kyr BP and lasts towards the end of the simulation. Although the phase of the second warming matches reasonably well with our new subsurface temperature record, the magnitude of the warming is only about 0.8°C in our model, which is considerably weaker than our new subsurface temperature record. Nevertheless, the overall YD time slice simulation seems to capture well the salient features of the reconstructed Niger Delta subsurface temperature record during the YD

IV.5. Discussion

IV.5.1. Niger Delta Surface

Today, the far eastern EEA is characterized by a pool of warm and fresh water that persists throughout the Gulf of Guinea with relatively little seasonal temperature variability (Figure 4.1). During an AMOC slowdown, the subsurface warming signal theoretically should propagate across the equatorial Atlantic as a Kelvin wave where upon reaching the west equatorial coast of Africa, it would be deflected north toward the Niger Delta and thus affecting conditions at our study site [*Brown et al.*, 2001; *Philander*, 1990]. In upwelling regions such as the EEA, it is possible, even expected, that the subsurface warming signal would propagate to the surface and manifest itself in the SST records of the region. Interestingly, both the Fan 17 *G. ruber* SST record, as well as the nearby SST record of *Weldeab et al.* [2007], both record a surface warming during Heinrich Event 1 (Figure 4.7A). Conversely, both SST reconstructions record a cooling during the Younger Dryas. To explain the opposite trends for these two cold periods, we propose the following hypothesis: the presence of a low-density freshwater cap in the EEA prevents upper thermocline temperature changes from mixing with the surface layer where *G. ruber* lives. During H1 when riverine discharge was greatly reduced in the region and there was no freshwater lid, seasonal upwelling allowed the subsurface warming to outcrop at the surface in the Niger Delta, resulting in a warming in our *G. ruber* record. However, by the time of the YD, increased precessional insolation had already increased the strength of the WAM and the resulting Niger River discharge, resulting in a freshwater cap that prevented the thermocline from outcropping

Figure 4.7 Comparison of Fan 17 Records with Regional Data: (A) Fan 17 *G. ruber* Mg/Ca SST (dark blue) plotted with the nearby record of *G. ruber* SST from MD03-2707 (light blue). (B) *G. crassaformis* subsurface temperature record from the Bonaire Basin in the southern Caribbean Sea [*Schmidt et al*. 2012] and (C) Fan 17 subsurface temperature from the Niger Delta. Note the 3 point weighted means are plotted for clarity and axes are inverted with weak AMOC reading down to be consistent with (D) the $^{231}Pa/^{230}Th$ record of AMOC variability from the Bermuda Rise [*McManus et al*. 2004]. (E) NGRIP ice core record [*Anderson et al*. 2004]. Subsurface temperature records record warming events coincident with decreasing values of $^{231}Pa/^{230}Th$ interpreted to to reflect a weakening AMOC during Heinrich Event 1 and the Younger Dryas.

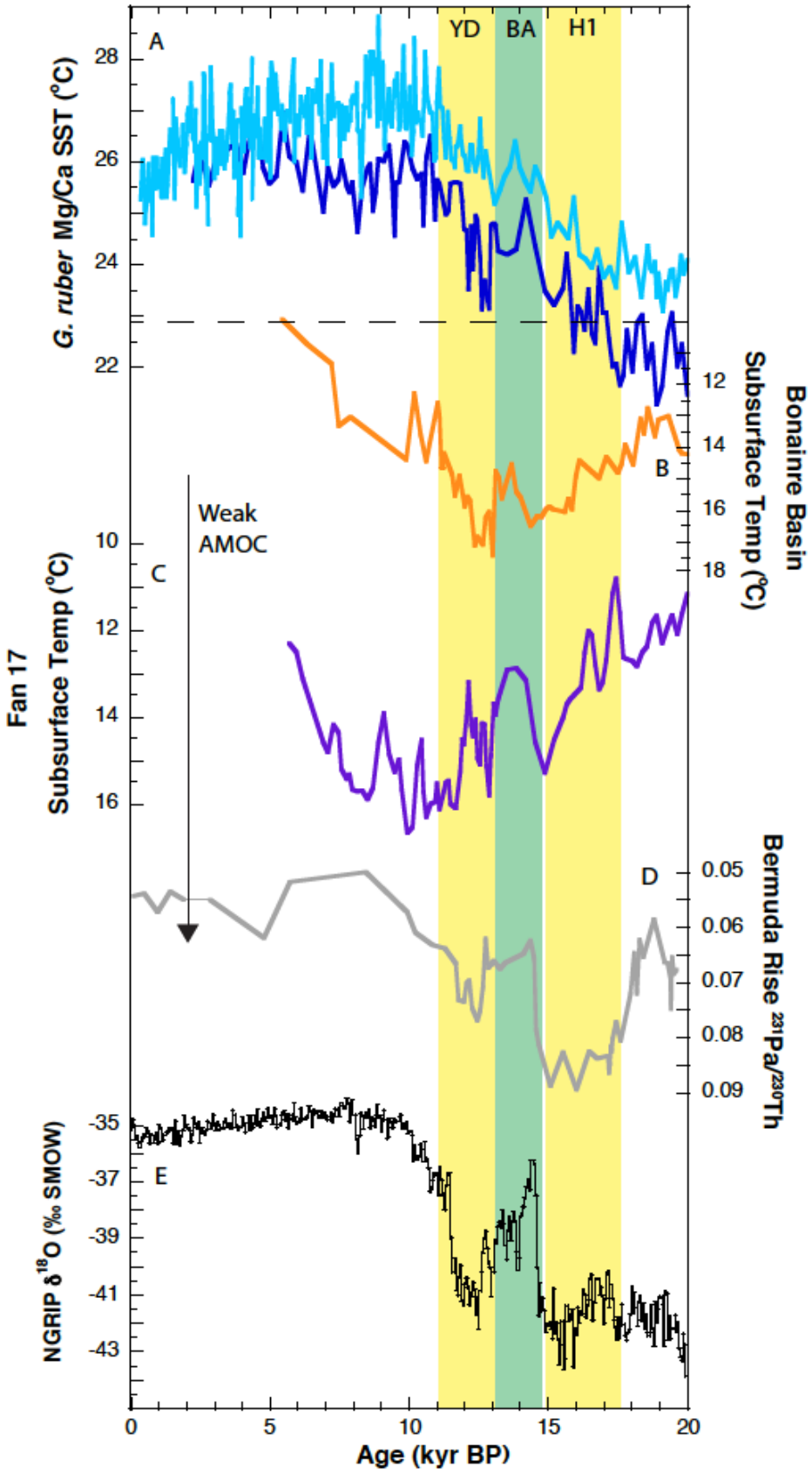
A
YD
BA
H1
G. ruber Mg/Ca SST (°C)
28
26
24
22
B
Bonainre Basin
Subsurface Temp (°C)
12
14
16
18
Weak
AMOC
C
Fan 17
Subsurface Temp (°C)
10
12
14
16
D
Bermuda Rise 231Pa/230Th
0.05
0.06
0.07
0.08
0.09
E
NGRIP δ18O (‰ SMOW)
-35
-37
-39
-41
-43
0
5
10
15
20
Age (kyr BP)

at the surface. During the YD, therefore, it is possible the SST records from the Gulf of Guinea reflect the cooling of the shallow freshwater cap in response to cooler Northern Hemisphere climate at this time. Due to the multiple factors that can affect the surface layer conditions in the Niger Delta and the Gulf of Guinea as a whole, the resulting SST records sometimes reflect ocean temperature changes from below and sometimes atmospheric cooling from above. Nevertheless, a regional subsurface warming is likely to affect SSTs in both the coastal and equatorial upwelling regions located farther to the south, and could therefore impact the land-sea temperature gradient and have an impact on the regional monsoon systems.

IV.5.2. Niger Delta Subsurface

Based on the subsurface warming mechanism discussed in section 1, a weakening of AMOC is predicted to allow the warm salinity maximum waters of the subtropical North Atlantic to enter the equatorial region and affect the Fan 17 site [*Chang et al.*, 2008; *Schmidt et al.*, 2012b; *Zhang*, 2007]. During H1, an abrupt warming is recorded by in the Niger Delta *G. crassaformis* record at ~16.1 kyr. Rising subsurface temperatures continue to increase until ~15 kyr. A similar record from *Schmidt et al.* [2012b], which reconstructed subsurface temperatures in the Bonaire Basin of the Southern Caribbean also using *G. crassaformis* Mg/Ca, displays remarkably similar variability (Figure 4.7b). During Heinrich 1 and nearly concurrent with the Niger Delta, the Bonaire Basin record records a ~1.5^{o}C warming of the subsurface. At this same time, ^{231}Pa/^{230}Th records from the Bermuda rise, thought to reflect changes in glacial AMOC, record conditions indicative of a significantly reduced AMOC state [*Bradtmiller et al.*,

2014; *McManus et al.*, 2004](Figure 4.7d). Immediately following H1, *G. crassaformis* Mg/Ca ratios then decrease, indicating a cooling in the Niger Delta at the start of the BA. This subsurface cooling is consistent with a strengthening of AMOC, which shuts down the delivery of warm, salinity maximum waters from the tropical North Atlantic allowing the EEA subsurface to cool. Remarkably, subsurface temperatures in the Bonaire Basin also cool simultaneously (Figure 4.7b). In addition, Bermuda Rise $^{231}Pa/^{230}Th$ ratios support the observation for an abrupt resumption of AMOC at the start of the BA. Following this period of relatively cool subsurface temperatures at the Niger Delta, subsurface temperature abruptly increases again near the start of the YD (Figure 4.7c). The magnitude of this warming is substantially larger than during the Heinrich Event 1, suggesting a warming as much as 3^{o}C at this time. Similar warming is recorded in the Bonaire Basin and changes in Bermuda Rise $^{231}Pa/^{230}Th$ ratios also shift toward values characteristic of reduced AMOC (Figure 4.7d). Thus, the abrupt subsurface warmings during H1 and at the start of the YD in our *G. crassaformis* record from the Niger Delta are consistent with the predicted subsurface temperature changes associated with a significant reduction in AMOC strength at these times.

It is not surprising that the magnitude of subsurface warming is greater at the onset of the YD than at the beginning of H1, given the different boundary conditions. $^{231}Pa/^{230}Th$ ratios in sediments from the Bermuda Rise [*McManus et al.*, 2004] suggest AMOC began to weaken as early as 17.5-18 kyr, or 1 kyr before the extreme H1 conditions developed in the North Atlantic (Figure 4.7d). Therefore, a long-term subsurface warming trend from 17.5 to 14.8 kyr in the Niger Delta may be consistent

with a gradual weakening of AMOC across this this time period. Conversely, leading up to the YD, subsurface temperatures are relatively cool, as AMOC strength was considerably stronger before the onset of the YD. Therefore, the magnitude of AMOC change at the start of the YD was likely larger than at the onset of H1, resulting in a larger, more abrupt subsurface temperature change in the Niger Delta.

Nevertheless, our new Niger Delta subsurface temperature record suggests an abrupt warming of several degrees at the beginning of the YD, followed by a cooling from 12.3 to 12.0 kyr (Figure 4.7c). A second subsurface warming in the Niger Delta then occurs during the transition to the early Holocene starting at ~11.9 kyr. This same pattern is also observed in our time slice modeling results (Figure 4.5c) that show and initial subsurface warming at 12.9 kyr, followed by a subsurface cooling from 12.3 to 12.0 kyr related to a strengthening of AMOC. This increase in AMOC strength in our modeling simulation is caused by a decrease in freshwater input into the North Atlantic from 12.3 to 11.9 kyr, based on the reconstructed sea level record in *Carlson et al.* [2007].

Although the warming events in our *G. crassaformis* subsurface temperature record during H1 and the YD are consistent with a reduction in AMOC, it is also possible that changes in upwelling strength and thermocline structure in the Niger Delta affected subsurface temperatures. During H1 and the YD,, steepened meridional temperature gradients caused an intensification of the trade winds [*McGee et al.*, 2010]. In coastal upwelling systems, increased upwelling has been documented in response to stronger trade winds and a more southerly ITCZ [*Deplazes et al.*, 2013; *Haug et al.*, 2001;

Schmidt et al., 2012b]. In particular, *Foster and Sexton* [2014] reconstructed pH and CO_2 of EEA surface waters for the last 30 kyr and found that upwelling in the EEA cold tongue was as much as five times higher during the last glacial. Stronger upwelling in the Niger Delta would cause the thermocline to shoal to and cause the subsurface to cool. Nevertheless, the warming in our Niger Delta subsurface record during H1 and the YD, both thought to be times of stronger winds and increased upwelling in the EEA, lends further support to our interpretation that the subsurface warming results from changes in ocean circulation patterns.

IV.5.3. Monsoon Teleconnections

Chang et al. [2008] hypothesized that the warming of subsurface waters in the EEA would would also impact temperatures in the EEA cold tongue, which in turn would reduced the land-sea temperature gradient that is critical to monsoon initiation. To explore the impact subsurface warming may have on the monsoon of West Africa, we compare our *G. crassaformis* subsurface temperature reconstruction with the previously published record of *G. ruber* Ba/Ca also from sediment core Fan 17 in Parker et al. [in review] (Figure 4.8). As shown in *Parker et al*., [2016], Ba/Ca ratios in *G. ruber* can be used to reconstruct changes in Niger River discharge across the last deglaciation in Fan 17. Nevertheless, the Fan 17 Ba/Ca record of Niger River discharge does not appear to be strongly correlated with our new subsurface temperature record. During H1, when subsurface temperatures warm over the 17.5-14.8 kyr interval, there is no corresponding decrease in Ba/Ca ratios that would suggest decreased discharge and weakening of the WAM (Figure 4.8). In fact, the Ba/Ca record suggests there is very little change in Niger

Figure 4.8 Monsoon Proxies from West Africa: (A) Northern Hemisphere summertime insolation at 11^{o}N calculated from *Paillard et al*. [1996], (B) Fan 17 Ba/Ca (μmol/mol), (C) Lake Bosumtwi δD (‰ VSMOW), (D) Fan 17 subsurface temperature and (E) NGRIP ice core record *Anderson et al.* [2004]. Fan 17 Ba/Ca interpreted to reflect Niger River discharge closely correlates with Northern Hemisphere summer insolation at 11^{o}N insolation because summertime insolation affects the thermal gradient and the northward extent to which monsoon rains reach across the Sahara and Sahel. Whereas, Lake Bosumtwi δD is punctuated by abrupt decreases in precipitation coincident with subsurface warming. Subsurface warming likely caused a decrease in intensity of rainfall and changes in its seasonal cycle.

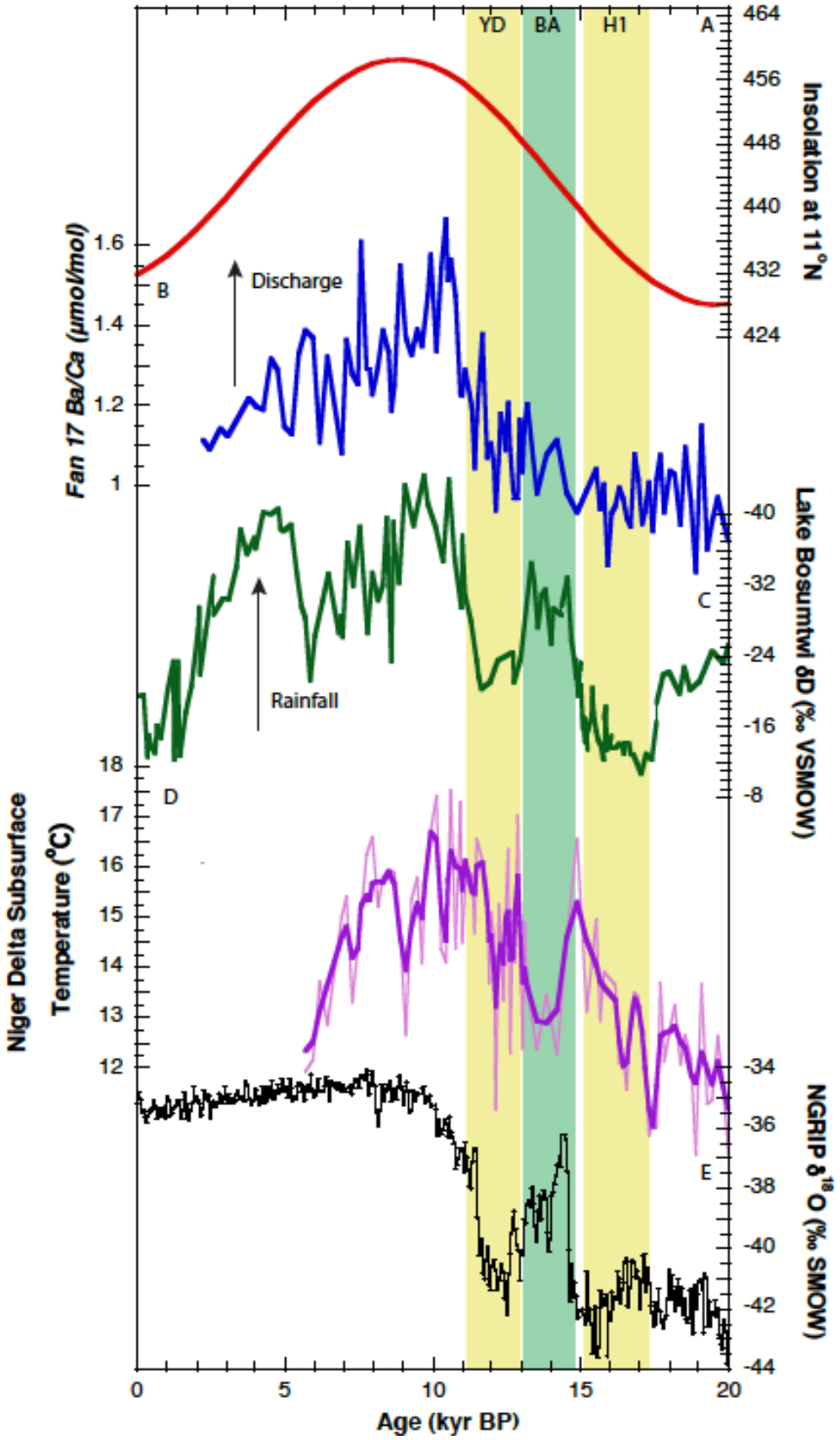
YD
BA
H1
A
B
C
D
E
Discharge
Rainfall
Insolation at 11°N
Fan 17 Ba/Ca (µmol/mol)
Lake Bosumtwi δD (‰ VSMOW)
Niger Delta Subsurface Temperature (°C)
NGRIP δ18O (‰ SMOW)
Age (kyr BP)
0
5
10
15
20
464
456
448
440
432
424
1.6
1.4
1.2
1
-40
-32
-24
-16
-8
18
17
16
15
14
13
12
-34
-36
-38
-40
-42
-44

River discharge from the LGM through H1. It is not until 14.8 kyr, upon cooling of subsurface temperatures that a gradual increase in Ba/Ca ratios is recorded. This gradual increase continues until the YD, when the Ba/Ca record suggest a pause at ~12.9kyr in the overall trend of increasing Niger River discharge. This is precisely when subsurface temperatures abruptly warm in our *G. crassaformis* record.

In contrast, a $\delta D_{leafwax}$ record interpreted to reflect changes in precipitation associated with monsoon intensity from Lake Bosumtwi in Ghana does record deglacial monsoon variability consistent with the idea that regional subsurface warming shown in our record may have impacted WAM strength along the Guinea Coast during H1 [*Shanahan et al.*, 2015]. During the entire period between 17.5 and 14.8 kyr when the Fan 17 subsurface record suggests warming, Lake Bosumtwi δD values become more positive relative to the LGM, indicating this period experienced considerably less precipitation during H1 (Figure 4.8). Then, coincident with our record of subsurface cooling from 14.8 to 13 kyr, Lake Bosumtwi δD values record a significant increase in precipitation at the start of the BA. Finally, at the start of the YD, the Lake Bosumtwi record suggests the onset of much drier conditions; just as our subsurface temperature record abruptly increases.

This dichotomy between subsurface temperature change in the EEA and our Ba/Ca record of Niger River discharge is likely the result of the complex dynamics driving the monsoon. During the winter months, the monsoonal convection is located over the relatively warm waters of the EEA. In early spring, convection follows the warmer waters north to the Guinea Coast upon initial development of the EEA cold

tongue. The monsoon stays over the warmer waters around the Guinea Coast through early summer, until the latitudinal temperature gradient becomes well developed and convection abruptly shifts to the latitudes of the Sahara and Sahel [*Thorncroft et al.*, 2011]. Ultimately, the northward extent to which the monsoon rainbelt reaches is controlled by the intensity of the meridional temperature gradient set up by the hot Sahara and cool EEA SSTs. To this extent, Northern Hemisphere solar insolation plays an important role in modulating the intensity of continental heating, and has been shown to be a significant contributor to the long-term intensity of rainfall across West Africa [*Otto-Bliesner et al.*, 2014]. Thus, solar radiative forcing of the WAM strongly contributes to the long-term variability of rainfall across West Africa, whereas oceanic forcing (via subsurface warming) provides the trigger for abrupt monsoon disruption.

During the LGM and H1, low Northern Hemisphere summertime insolation likely limited the northward extreme of the monsoon across interior West Africa, leading to persistent low Niger River discharge at this time. Because the rainfall had yet to begin across the Niger River catchment area, the change in precipitation and thus river discharge from LGM to H1 was negligible. However along the Guinea Coast, δD values suggest that Lake Bosumtwi (6^{o}N) was undoubtly experiencing a rainy season during the LGM [*Shannahan et al*. 2015]. As subsurface waters began to warm the EEA cold tongue around 17.5 kyr, the weakening of the thermal gradient likely shortened the length of the rainy season over the Guinea coast as the rainbelt became biased toward the warmer waters of the EEA, causing a drying at Lake Bosumtwi. At 14.8 kyr, cooling of the subsurface and increased Northern Hemisphere insolation steepened the thermal

land-sea contrast and as a result, the seasonal cycle of the rainbelt became more established at the coast. This lead to a dramatic increase in rainfall at Lake Bosumtwi, while to the north, the steepened thermal gradient allowed the monsoon to penetrate into the southern most latitudes of the Niger River Basin leading to a gradual increase in river discharge. After a brief period of increasing monsoon intensity, an abrupt warming of subsurface waters at the start of the YD at 12.9 kyr again weakened the northward progression of the monsoon leading to conditions similar to H1. Because rainfall was not yet widespread across the Niger River Basin prior to 12.9 kyr, the magnitude of change in rainfall was minor in comparison with Lake Bosumtwi, where a reduced seasonal cycle and monsoon intensity lead to a significant decrease in precipitation. Rainfall remained low for the first, most intense part of the YD until the thermal gradient reestablished itself at 11.9 kyr. Following the YD, peak precessional forcing allowed a robust monsoon to penetrate deep into West Africa resulting, in the wettest conditions at both sites around 10 kyr. Despite continued cooling of the subsurface during the Holocene, gradually decreasing Niger River discharge and precipitation at Lake Bosumtwi is likely the result of decreasing monsoon intensity and a steady southward progression of the rainbelt's northerly extreme in response to declining Northern Hemisphere summer insolation [*Paillard et al.*, 1996; *Shanahan et al.*, 2015].

IV.6. Conclusions

Here we present evidence of the effect reduced AMOC had on climate dynamics in the Eastern Equatorial Atlantic. Our *G. crassaformis* record of subsurface temperature change during the deglacial from the Niger Delta reveals two periods of subsurface

warming during H1 and the YD. During Heinrich 1, subsurface temperatures around the Niger Delta warmed by 1.5^{o}C. Then, following a period of cooler temperatures, subsurface temperature once again rose by 3^{o}C during the YD event. These warming events of the subsurface during documented periods of reduced AMOC are consistent with the oceanic teleconnection mechanism where a slowdown in the strength of AMOC allows warm salinity maximum waters from the subtropical North Atlantic to enter in to the Tropical Atlantic. To further evaluate the relationship between subsurface temperatures around the Niger Delta and a weakened AMOC, we performed water-hosing simulations for the Younger Dryas. Our new high-resolution time slice AOGCM experiments across the YD suggest a strong negative correlation of -0.95 between the Niger Delta subsurface temperature change and AMOC strength. Our modeling results also show a two-phased YD where the first half of the cold event was characterized by the strongest reduction in AMOC, when AMOC was reduced from 13 to 6.5 Sv between 12.9 and 12.3 kyr. This two-phased YD is also recorded in our *G. crassaformis* subsurface temperature record as a 3^{o}C warming during the same time, followed by a smaller warming between 11.9 and 11.5 kyr. The result of this subsurface warming during a weak AMOC likely caused SSTs across the EEA to warm, reducing the land-sea thermal gradient and weakening the West African Monsoon. Clearly, AMOC was intricately coupled with the tropical Atlantic subsurface during the deglacial and had significant impacts both regionally and globally.

CHAPTER V

CONCLUSIONS

This dissertation aimed to further expand the understanding of Atlantic Meridional Overturning Circulation (AMOC) variability during the last glacial cycle and it's impact of the monsoon of West Africa. The following is a summary of the research and major findings in this dissertation:

The goal of Chapter II was to investigate AMOC variability during Marine Isotope Stage 3 (MIS 3) between 22 and 60 kyr BP. Considerable evidence exists in support of large swings in AMOC strength during the last deglacial 10-20 kyr BP, however, far less is known during MIS 3. Large warming and cooling oscillations, known as Dansgaard-Oscheger events (DO), characterized MIS3 climate. While AMOC has always been suspected as a potential driver of these events, the rapid frequency in which they occur (some in less than 1,000 years) makes paleoceanographic reconstructions difficult because the necessary core would require exceptionally high sedimentations rates. In this study, a high sedimentation rate core from the Bonaire Basin in the Southern Caribbean Sea was used to reconstruct subsurface temperatures as a proxy for AMOC strength. Subsurface temperatures in this region are thought to be related to AMOC strength via the oceanic teleconnection in which a reduction in the strength of the western boundary current in response to weakened AMOC allows warm salinity maximum waters from the North Atlantic subtropical gyre to enter the tropical

North Atlantic. Using the subsurface dwelling species of planktonic foraminifera *G. truncatulinoides*, and measuring the Mg/Ca of the shell calcite (a proxy for ocean temperature), a record of subsurface thermal history was produced for the Bonaire Basin for most of MIS 3. The record reveals numerous subsurface warming events coincident with DO cooling. Of the 9 DO events covered by this record, 7 had evidence of subsurface warming. Only the two smallest DO events of the covered period had no associated warming pulse likely due to the short (>500 year) length of each event. In addition, Heinrich Events, large discharges of icebergs into the North Atlantic, are also associated with reduced AMOC. The *G. truncatulinoides* record of subsurface temperature in the Bonaire Basin shows a large warming pulse at Heinrich Event 4, however, no warming pulse is detected during Heinrich Events 2 and 3. This is in accordance with recent studies that suggested these events were not associated with large swing in AMOC strength [*Lynch-Stieglitz et al*. 2014]. The *G. truncatulinoides* subsurface temperature record is one of the first proxy-based records to confidently link AMOC and DO variability together during MIS 3.

Chapter III then aimed to evaluate the effect of reduced AMOC on the West African Monsoon (WAM). *Chang et al.* [2008] proposed that as part of the oceanic teleconnection mechanism, the warm salinity maximum waters would leak into the equatorial zone where they would become entrained in equatorial upwelling and warm the Eastern Equatorial Atlantic (EEA) cold tongue. The thermal gradient between the hot Saharan desert and cold sea-surface temperatures of the EEA is critical to the monsoon development. Thus, during periods of weak AMOC, warming to the EEA SST would

reduce the thermal gradient and impede monsoon development. Niger delta discharge is closely linked with the magnitude of monsoonal rainfall upstream, thus, a core from the Niger Delta was used to reconstruct the discharge history of the river during the deglacial using the surface dwelling planktonic foraminifer *G. ruber*. The *G. ruber* shell was measured for Ba/Ca, which is dissolved in river water and mixes linearly with seawater to provide a measure of freshwater discharge at the delta. The *G. ruber* Ba/Ca record reveals surprisingly little variability with low discharge conditions characterizing the delta between 15-20 kyr BP. Only after 15 kyr BP do Ba/Ca values gradually increase signifying enhanced discharge and monsoon rainfall across the river basin. This observation suggests that the WAM was not as susceptible to massive swings in intensity during climate reversals as previously thought. A similar record reconstructed to the east tracks rainfall variability associated with the equatorial monsoon. The differences between these records highlights 1) the "regionality" of rainfall across Africa and 2) the regionality is a result of the magnitude to which climate forcings effect the monsoons. For equatorial Africa, greenhouse gas forcing and North Atlantic SST play a critical role. Thus, rainfall across equatorial Africa was more variable earlier in the deglacial due to elevated atmospheric CO_2 levels and sudden cooling of North Atlantic SST's. Whereas, the WAM is highly dependent on the level of Northern Hemisphere summertime insolation. When insolation is low, such as during the first half of the deglacial, the monsoon is suppressed and therefore the magnitude of the effect abrupt climate change has on the WAM is much smaller than when insolation is high and the monsoon is strong.

Chapter IV focused on directly linking AMOC strength to WAM variability by developing a record of subsurface temperature variability for the Niger Delta using the deep dwelling planktonic foraminifera *G. crassaformis*. The subsurface temperature record reveals two periods of increased subsurface temperature coincidence with the Heinrich 1 and Younger Dryas events during the deglaciation. As a collaborative effort related to this research, Ping Chang performed a transient modeling simulation of the Younger Dryas using a high-resolution version of the CCSM3 model. The results clearly show a strong negative correlation ($r = -0.95$) between AMOC strength and Niger Delta subsurface temperature. Interestingly, the WAM record from Chapter III does not show any significant reduction in monsoon strength in response to subsurface warming during Heinrich Event 1, and only a small decrease during the Younger Dryas. This would suggest that a weak AMOC did not significantly affect WAM strength. However, a monsoon record from Lake Bosumtwi in Ghana does record a weak monsoon during Heinrich 1 and the Younger Dryas. While the Niger River record from Chapter III integrates a monsoon signal from the Niger River Basin (interior West Africa), the Lake Bosumtwi reconstruction records monsoon strength from a more southerly perspective along the Guinea coast. Thus, these spatial differences can be explained by the basic dynamics of the WAM. The northward penetration of the monsoon did not yet reach into the Niger River Basin during Heinrich Event 1 and therefore the change in rainfall was negligible, whereas, along the Guinea coast rainfall retreated in response to warmer EEA SST during H1. A similar picture emerged during the Younger Dryas, but a steadily increasing monsoon across the Niger River basin resulted in a small change in

precipitation during this time accompanying the large decrease seen in monsoonal rain at Lake Bosumtwi. Overall, this study establishes the response of the WAM across the deglaciation to reduced AMOC resulting in a reduced land-sea thermal gradient.

As it is becoming increasingly evident that the subsurface response of the Tropical Atlantic to AMOC not only provides a new means of reconstructing AMOC variability, but also plays a significant role in driving climatic teleconnections. This dissertation established the connection between subsurface warming in the western tropical Atlantic and Eastern Atlantic in response to AMOC weakening across the deglaciation. Future work should involve studies of locations in-between. Subsurface reconstructions from the equatorial Mid-Atlantic Ridge as well as along the western boundary would provide ample evidence that the subsurface warming signal in the east and west are related through the oceanic adjustment mechanism. In addition, reconstructions from other subsurface species of planktonic foraminifera would improve confidence that the warming signal is robust throughout the water column and not due to habitat migration. Also, given the local upwelling dynamics surrounding the Niger Delta, a subsurface reconstruction from a location closer to the Equator and more directly in the EEA upwelling zone would be useful in confirming the Niger Delta observations. To this end, due to the large freshwater cap around the Niger Delta the SST record from there did not correlate well with the subsurface. Thus, a SST record from a location directly within the equatorial upwelling zone is necessary to confirm the upwelling of warm subsurface waters indeed affects EEA SST. And lastly, new Ba/Ca

reconstructions from other major regional rivers like the Congo will continue to improve our understanding of the spatial-temporal evolution of rainfall in this region.

REFERENCES

Alvarez-Solas, J., A. Robinson, M. Montoya, and C. Ritz (2013), Iceberg discharges of the last glacial period driven by oceanic circulation changes, *P Natl Acad Sci USA*, 110(41), 16350-16354.

Anand, P., H. Elderfield, and M. H. Conte (2003), Calibration of Mg/Ca thermometry in planktonic foraminifera from a sediment trap time series, *Paleoceanography*, 18(2).

Andersen, K. K., et al. (2004), High-resolution record of Northern Hemisphere climate extending into the last interglacial period, *Nature*, *431*, 147-151.

Antonov, J. I., D. Seidov, T. P. Boyer, R. A. Locarnini, A. V. Mishonov, and H. E. Garcia (Eds.) (2010), World Ocean Atlas 2009, 184 pp., U.S. Government Printing Office, Washington, D.C.

Arbuszewski, J., P. deMenocal, A. Kaplan, and E. Farmer (2010), On the Fidelity of Shell-Derived δ18Oseawater Estimates, *Earth Planet Sc Lett*, 300, 185-196.

Barker, S., I. Cacho, H. Benway, and K. Tachikawa (2005), Planktonic foraminiferal Mg/Ca as a proxy for past oceanic temperatures: a methodological overview and data compilation for the Last Glacial Maximum, *Quaternary Sci Rev*, *24*(7-9), 821-834.

Barker, S., J. Chen, X. Gong, L. Jonkers, G. Knorr, D. Thornalley (2015), Icebergs not the trigger for North Atlantic cold events, *Nature*, 520, 333-336.

Bé, A. W. (1980), Gametogenic calcification in a spinose planktonic foraminifer, Globigerinoides sacculifer (Brady), *Mar. Micropaleontol*., 5, 283-310.

Bemis, B. E., H. J. Spero, J. Bijima, and D. W. Lea (1998), Reevaluation of the oxygen isotopic composition of planktonic foraminifera: Experimental results and revised paleotemperature equations, *Paleoceanography,* 13(2), 150-160.

Bohm, E., J. Lippold, M. Gutjahr, M. Frank, P. Blaser, B. Antz, J. Fohlmeister, N. Frank, M. B. Andersen, and M. Deininger (2015), Strong and deep Atlantic meridional overturning circulation during the last glacial cycle, *Nature*, 517(7532), 73-U170.

Bond, G., et al. (1992), Evidence for Massive Discharges of Icebergs into the North-Atlantic Ocean during the Last Glacial Period, *Nature*, *360*(6401), 245-249.

Bond, G., W. Showers, M. Elliot, M. Evans, R. Lotti, I. Hajdas, G. Bonani, and S. Johnson (1999), The North Atlantic's 1-2 kyr climate rhythm: Relation to Heinrich Events, Dansgaard/Oeschger Cycles and the Little Ice Age, in *Mechanisms of Global Climate Change at Millennial Timescales,* edited by P. U. Clark, R. S. Webb and L. D. Keigwin, pp. 35-58, American Geophysical Union, Washington DC.

Broecker, W. S., G. Bond, M. Klas, G. Bonani, and W. Wolfli (1990), A salt oscillator in the glacial Atlantic? The concept, *Paleoceanography*, 5(4), 469-478.

Broecker, W., G. Bond, M. Klas, E. Clark, and J. McManus (1992), Origin of the northern Atlantic's Heinrich events, *Clim Dynam*, *6*(3-4), 265-273.

Broecker, W. S. (1991), The great ocean conveyor, *Oceanography*, *4*, 79-89.

Brown, E., A. Colling, D. Park, J. Phillips, D. Rothery, and J. Wright (2001), *Ocean Circulation*, Butterworth-Heinemann, London.

Carlson, A. E., P. U. Clark, G. Raisbeck, and E. Brook (2007), Geochemical proxies of North American freshwater routing during the Younger Dryas cold event:, *P Natl Acad Sci USA*, *104*, 6556-6561.

Carlson, A. E., D. W. Oppo, R. E. Came, A. N. LeGrande, L. D. Keigwin, and W. B. Curry (2008), Subtropical Atlantic salinity variability and Atlantic meridional circulation during the last deglaciation, *Geology*, 36(12), 991-994.

Chang, P., R. Zhang, W. Hazeleger, C. Wen, X. Q. Wan, L. Ji, R. J. Haarsma, W. P. Breugem, and H. Seidel (2008), Oceanic link between abrupt changes in the North Atlantic Ocean and the African monsoon, *Nat Geosci*, 1(7), 444-448.

Charles, C. D., and R. G. Fairbanks (1990), Glacial to interglacial changes in the isotopic gradients of southern ocean surface water, in *Geological history of the Polar Oceans: Arctic versus Antarctic*, edited by U. Bleil and J. Thiede, pp. 519-538, Kluwer, Netherlands.

Charles, C.D., J. Lynch-Stieglitz, U.S. Ninnemann, R.G. Fairbanks (1996), Climate connections between the hemisphere revealed by deep sea sediment core/ice core correlations, *Earth Planet Sc Lett,* 192, 19-27.

Clark, P. U., S. J. Marshall, G. K. C. Clarke, S. W. Hostetler, J. M. Licciardi, and J. T. Teller (2001), Freshwater forcing of abrupt climate change during the last glaciation, *Science*, 293(5528), 283-287.

Clement, A. C., and L. C. Peterson (2008), Mechanisms of abrupt climate change of the last glacial period, *Rev Geophys*, 46(4).

Cleroux, C., J. Lynch-Stieglitz, M. W. Schmidt, E. Cortijo, and J. C. Duplessy (2009), Evidence for calcification depth change of Globorotalia truncatulinoides between deglaciation and Holocene in the Western Atlantic Ocean, *Mar Micropaleontol*, 73(1-2), 57-61.

Cleroux, C., E. Cortijo, J. C. Duplessy, and R. Zahn (2007), Deep-dwelling foraminifera as thermocline temperature recorders, *Geochem Geophy Geosy*, *8*.

Cleroux, C., E. Cortijo, P. Anand, L. Labeyrie, F. Bassinot, N. Caillon, and J. C. Duplessy (2008), Mg/Ca and Sr/Ca ratios in planktonic foraminifera: Proxies for upper water column temperature reconstruction, *Paleoceanography,* 23(3).

Cockerton, H. E., J. A. Holmes, F. A. Street-Perrott, and K. J. Ficken (2014), Holocene dust records from the West African Sahel and their implications for changes in climate and land surface conditions, *J Geophys Res-Atmos*, *119*(14), 8684-8694.

Coffey, M., F. Dehairs, O. Collette, G. Luther, T. Church, and T. Jickells (1997), The behaviour of dissolved barium in estuaries, *Estuarine Coastal and Shelf Science*, *45*(1), 113-121.

Collins, W. D., et al. (2006), The Community Climate System Model version 3 (CCSM3), *J Climate*, *19*(11), 2122-2143.

Collins, J. A., A. Govin, S. Mulitza, D. Heslop, M. Zabel, J. Hartmann, U. Rohl, and G. Wefer (2013), Abrupt shifts of the Sahara-Sahel boundary during Heinrich stadials, *Clim Past*, *9*(3), 1181-1191.

Collins, J. A., et al. (2011), Interhemispheric symmetry of the tropical African rainbelt over the past 23,000 years, *Nat Geosci*, *4*(1), 42-45.

Condron, A., and P. Winsor (2012), Meltwater routing and the Younger Dryas, *P Natl Acad Sci USA*, *109*(49), 19928-19933.

Conkright, M. E., S. Levitus, T. O'Brien, T. P. Boyer, J. Antonov, and C. Stephens (2002), World Ocean Atlas 2001: Objective Analyses, Data Statistics, and Figures, CD-ROM Documentation*Rep.*, 17 pp pp, National Oceanographic Data Center, Silver Spring, MD.

Curry, W. B., and D. W. Oppo (2005), Glacial water mass geometry and the distribution of delta C-13 of Sigma CO2 in the western Atlantic Ocean, *Paleoceanography*, 20(1), doi:10.1029/2004PA001021.

Danabasoglu, G., et al. (2014), North Atlantic simulations in Coordinated Ocean-ice Reference Experiments phase II (CORE-II). Part I: Mean states, *Ocean Model*, *73*, 76-107.

Dansgaard, W., et al. (1993), Evidence for General Instability of Past Climate from a 250-Kyr Ice-Core Record, *Nature*, *364*(6434), 218-220.

Dekens, P. S., D. W. Lea, D. K. Pak, and H. J. Spero (2002), Core top calibration of Mg/Ca in tropical foraminifera: refining paleotemperature estimation, *Geochem Geophy Geosy*, 4(6), doi:10/1029/2001GC000200.

deMenocal, P., J. Ortiz, T. Guilderson, J. Adkins, M. Sarnthein, L. Baker, and M. Yarusinsky (2000), Abrupt onset and termination of the African Humid Period: rapid climate responses to gradual insolation forcing, *Quaternary Sci Rev*, *19*(1-5), 347-361.

Deplazes, G., et al. (2013), Links between tropical rainfall and North Atlantic climate during the last glacial period, *Nat Geosci*, *6*(3), 213-217.

Dokken, T. M., K. H. Nisancioglu, C. Li, D. S. Battisti, and C. Kissel (2013), Dansgaard-Oeschger cycles: Interactions between ocean and sea ice intrinsic to the Nordic seas, *Paleoceanography*, 28(3), 491-502.

Elderfield, H., and G. Ganssen (2000), Past temperature and d18O of surface ocean waters inferred from foraminiferal Mg/Ca ratios, Nature, 405, 442-445.

Elliot, M., L. D. Labeyrie, and J. C. Duplessy (2002), Changes in North Atlantic deep-water formation associated with the Dansgaard-Oeschger temperature oscillations (60-10 ka), *Quaternary Sci Rev*, 21, 1153-1165.

Emiliani, C. (1954), Depth Habitats of Some Species of Pelagic Foraminifera as Indicated by Oxygen Isotope Ratios, *Am J Sci*, *252*(3), 149-158.

Evan, A. T., C. Flamant, S. Fiedler, and O. Doherty (2014), An analysis of aeolian dust in climate models, *Geophys Res Lett*, *41*(16), 5996-6001.

Foster, G. L., and P. F. Sexton (2014), Enhanced carbon dioxide outgassing from the eastern equatorial Atlantic during the last glacial, *Geology*.

Fratantoni, D. M., W. E. Johns, T. L. Townsend, and H. E. Hurlburt (2000), Low-latitude circulation and mass transport pathways in a model of the tropical Atlantic ocean, *J Phys Oceanogr*, 30(8), 1944-1966.

Gasse, F., F. Chalie, A. Vincens, M. A. J. Williams, and D. Williamson (2008), Climatic patterns in equatorial and southern Africa from 30,000 to 10,000 years ago reconstructed from terrestrial and near-shore proxy data, *Quaternary Sci Rev*, *27*(25-26), 2316-2340.

Gherardi, J. M., L. Labeyrie, S. Nave, R. Francois, J. F. McManus, and E. Cortijo (2009), Glacial-interglacial circulation changes inferred from Pa-231/Th-230 sedimentary record in the North Atlantic region, *Paleoceanography*, *24*.

Hastings, D. W., A. D. Russell, and S. R. Emerson (1998), Foraminiferal magnesium in Globigerinoides sacculifer as a paleotemperature proxy, *Paleoceanography*, 13(2), 161-169.

Haug, G. H., K. A. Hughen, D. M. Sigman, L. C. Peterson, and U. Rohl (2001), Southward migration of the intertropical convergence zone through the Holocene, *Science*, 293(5533), 1304-1308.

Hazeleger, W., and S. Drijfhout (2006), Subtropical cells and meridional overturning circulation pathways in the tropical Atlantic, *J Geophys Res-Oceans*, 111(C3).

Heinrich, H. (1988), Origin and Consequences of Cyclic Ice Rafting in the Northeast Atlantic-Ocean during the Past 130,000 Years, *Quaternary Res*, *29*(2), 142-152.

Hemming, S. R. (2004), Heinrich events: Massive late pleistocene detritus layers of the North Atlantic and their global climate imprint, *Rev Geophys*, *42*(1).

Hertzberg, J. E., and M. W. Schmidt (2013), Refining Globigerinoides ruber Mg/Ca paleothermometry in the Atlantic Ocean, *Earth Planet Sc Lett*, 383, 123-133.

Honisch, B., K. A. Allen, D. W. Lea, H. J. Spero, S. M. Eggins, J. Arbuszewski, P. deMenocal, Y. Rosenthal, A. D. Russell, and H. Elderfield (2013), The influence of salinity on Mg/Ca in planktic foraminifers - Evidence from cultures, core-top sediments and complementary delta O-18, *Geochim Cosmochim Ac*, 121, 196-213.

Hopkins, J., M. Lucas, C. Dufau, M. Sutton, J. Stum, O. Lauret, and C. Channelliere (2013), Detection and variability of the Congo River plume from satellite derived sea surface temperature, salinity, ocean colour and sea level, *Earth Planet Sc Lett*, *139*(0), 365-385

Hu, A. X., G. A. Meehl, W. Q. Han, B. Otto-Bliestner, A. Abe-Ouchi, and N. Rosenbloom (2015), Effects of the Bering Strait closure on AMOC and global climate under different background climates, *Prog Oceanogr*, *132*, 174-196.

Itambi, A. C., T. von Dobeneck, S. Mulitza, T. Bickert, and D. Heslop (2009), Millennial-scale northwest African droughts related to Heinrich events and Dansgaard-Oeschger cycles: Evidence in marine sediments from offshore Senegal, *Paleoceanography*, *24*.

Itiveh, K. O., and G. R. Bigg (2008), The variation of discharge entering the Niger Delta system, 1951-2000, and estimates of change under global warming, *Int J Climatol*, *28*(5), 659-666.

Jobe, Z. R., D. R. Lowe, and S. J. Uchytil (2011), Two fundamentally different types of submarine canyons along the continental margin of Equatorial Guinea, *Marine and Petroleum Geology*, *28*, 843-860.

Jochum, M., and P. Malanotte-Rizzoli (2001), Influence of the meridional overturning circulation on tropical-subtropical pathways, *J Phys Oceanogr*, 31(5), 1313-1323.

Jouanno, J., F. Marin, Y. du Penhoat, J. M. Molines, and J. Sheinbaum (2011), Seasonal Modes of Surface Cooling in the Gulf of Guinea, *J Phys Oceanogr*, *41*(7), 1408-1416.

Kanner, L. C., S. J. Burns, H. Cheng, and R. L. Edwards (2012), High-Latitude Forcing of the South American Summer Monsoon During the Last Glacial, *Science*, *335*(6068), 570-573.

Keigwin, L. D., and E. A. Boyle (1999), Surface and deep ocean variability in the northern Sargasso Sea during marine isotope stage 3, *Paleoceanography*, 14(2), 164-170.

Kirchner, K., M. Rhein, S. Huttl-Kabus, and C. W. Boning (2009), On the spreading of South Atlantic Water into the Northern Hemisphere, *J Geophys Res-Oceans*, 114.

Kouadio, Y. K., S. Djjakoure, A. Aman, K. E. Ali, V. Kone, and E. Toualy (2013), Characterization of the boreal summer upwelling at the northern coast of the Gulf og Guinea based on the PROPAO in situ measurements network and satellite data *International Journal of Oceanography 2013*, 11.

Koutavas, A., and J. Lynch-Stieglitz (2003), Glacial-interglacial dynamics of the eastern equatorial Pacific cold tongue Intertropical Convergence Zone system reconstructed from oxygen isotope records, *Paleoceanography*, 18(4).

Kuhlbrodt, T., A. Griesel, M. Montoya, A. Levermann, M. Hofmann, and S. Rahmstorf (2007), On the driving processes of the Atlantic meridional overturning circulation, *Rev Geophys*, *45*(1).

Lea, D. W. (1999), Trace elements in foraminiferal calcite, in *Modern Foraminifera*, edited by B. K. S. Gupta, pp. 259-277, Kluwer Academic Publishers, Great Britain.

Lea, D. W., D. K. Pak, and H. J. Spero (2000), Climate Impact of Late Quaternary Equatorial Pacific Sea Surface Temperature Variations, *Science*, 289, 1719-1724.

Lea, D. W., P. A. Martin, D. K. Pak, and H. J. Spero (2002), Reconstructing a 350 ky history of sea level using planktonic Mg/Ca and oxygen isotope records from a Cocos Ridge core, *Quaternary Sci Rev*, 21, 283-293.

Leduc, G., L. Vidal, K. Tachikawa, and E. Bard (2009), ITCZ rather than ENSO signature for abrupt climate changes across the tropical Pacific?, *Quaternary Res*, *72*(1), 123-131.

Liu, Z., et al. (2009), Transient Simulation of Last Deglaciation with a New Mechanism for Bolling-Allerod Warming, *Science*, *325*(5938), 310-314.

Loulergue, L., A. Schilt, R. Spahni, V. Masson-Delmotte, T. Blunier, B. Lemieux, J. M. Barnola, D. Raynaud, T. F. Stocker, and J. Chappellaz (2008), Orbital and millennial-scale features of atmospheric CH4 over the past 800,000 years, *Nature*, *453*(7193), 383-386.

Lyle, M., A. Olivarez Lyle, T. Gorgas, A. Holbourn, T. Westerhold, E. Hathorne, K. Kimoto, and G. Yamamoto (2012), Data report: raw and normalized elemenetal data along the site U1338 splice from x-ray flourescence scanning, *Proceedings of the International Ocean Drilling Program*, *320/321*.

Lynch-Stieglitz, J., M. W. Schmidt, and W. B. Curry (2011), Evidence from the Florida Straits for Younger Dryas Ocean Circulation Changes, *Paleoceanography*, *26*, PA1205.

Lynch-Stieglitz, J., M. W. Schmidt, L. G. Henry, W. B. Curry, L. C. Skinner, S. Mulitza, R. Zhang, and P. Chang (2014), Muted change in Atlantic overturning circulation over some glacial-aged Heinrich events, *Nat Geosci*, 7(2), 144-150.

Lyngsie, G., T. Awadzi, and H. Breuning-Madsen (2011), Origin of Harmattan dust settled in Northern Ghana - Long transported or local dust?, *Geoderma*, *167-68*, 351-359.

Marcott, S. A., et al. (2011), Ice-shelf collapse from subsurface warming as a trigger for Heinrich events, *P Natl Acad Sci USA*, 108(33), 13415-13419.

Mashiotta, T. A., L. D. W, and H. J. Spero (1999), Glacial-interglacial changes in Subantarctic sea surface temperature and d18O-water using foraminiferal Mg, *Earth Planet Sc Lett*, 170, 417-432.

McConnell, M. C., and R. C. Thunell (2005), Calibration of the planktonic foraminiferal Mg/Ca paleothermometer: sediment trap results from the Guaymas Basin, Gulf of California, *Paleoceanography*, 20(2).

McGee, D., W. S. Broecker, and G. Winckler (2010), Gustiness: The driver of glacial dustiness?, *Quaternary Sci Rev*, *29*(17-18), 2340-2350.

McGee, D., P. B. deMenocal, G. Winckler, J. B. W. Stuut, and L. I. Bradtmiller (2013), The magnitude, timing and abruptness of changes in North African dust deposition over the last 20,000 yr, *Earth Planet Sc Lett*, *371*, 163-176.

McIntyre, A., and B. Molfino (1996), Forcing of Atlantic equatorial and subpolar millennial cycles by precession, *Science*, *274*(5294), 1867-1870.

McKenna, V. S., and W. L. Prell (2004), Calibration of the Mg/Ca of Globorotalia truncatulinoides (R) for the reconstruction of marine temperature gradients, *Paleoceanography,* 19(2).

McManus, J. F., R. Francois, J.-M. Gherardi, L. D. Keigwin, and S. Brown-Leger (2004), Collapse and rapid resumption of Atlantic meridional circulation linked to deglacial climate changes, *Nature*, 428(22 April), 834-837.

Menviel, L., A. Timmermann, O. E. Timm, and A. Mouchet (2011), Deconstructing the Last Glacial termination: the role of millennial and orbital-scale forcings, *Quaternary Sci Rev*, 30(9-10), 1155-1172.

Menviel, L., A. Timmermann, T. Friedrich, and M. H. England (2014), Hindcasting the continuum of Dansgaard-Oeschger variability: mechanisms, patterns and timing, *Clim Past*, *10*(1), 63-77.

Mulitza, S., M. Prange, J. B. Stuut, M. Zabel, T. von Dobeneck, A. C. Itambi, J. Nizou, M. Schulz, and G. Wefer (2008), Sahel megadroughts triggered by glacial slowdowns of Atlantic meridional overturning, *Paleoceanography*, *23*(4).

Murphy, L. N., A. C. Clement, S. Albani, N. M. Mahowald, P. Swart, and M. M. Arienzo (2014), Simulated changes in atmospheric dust in response to a Heinrich stadial, *Paleoceanography*, *29*(1), 30-43.

Murray, R. W., and M. Leinen (1996), Scavenged excess aluminum and its relationship to bulk titanium in biogenic sediment from the central equatorial Pacific Ocean, *Geochim Cosmochim Ac*, *60*(20), 3869-3878.

Murray, R. W., C. Knowlton, M. Leinen, A. C. Mix, and C. H. Polsky (2000), Export production and terrigenous matter in the Central Equatorial Pacific Ocean during interglacial oxygen isotope Stage 11, *Global Planet Change*, *24*, 59-78.

Muscheler, R., B. Kromer, S. Bjorck, A. Svensson, M. Friedrich, K. F. Kaiser, and J. Southon (2008), Tree rings and ice cores reveal C-14 calibration uncertainties during the Younger Dryas, Nat Geosci, 1(4), 263-267.

Nicholson, S. E. (2008), The intensity, location and structure of the tropical rainbelt over west Africa as factors in interannual variability, *Int J Climatol*, *28*(13), 1775-1785.

Nicholson, S. E. (2009), A revised picture of the structure of the "monsoon" and land ITCZ over West Africa, *Clim Dynam*, *32*(7-8), 1155-1171.

Nicholson, S. E. (2013), The West African Sahel: A review of recent studies on the rainfall regime and its interannual variability, *ISRN Meteorology 2013*, 1-32.

Nicholson, S. E., and J. P. Grist (2001), A conceptual model for understanding rainfall variability in the West African Sahel on interannual and interdecadal timescales, *Int J Climatol*, *21*(14), 1733-1757.

Nurnberg, D., J. Bijma, and C. Hemleben (1996), Assessing the reliability of magnesium in foraminiferal calcite as a proxy for water mass temperatures, *Geochim Cosmochim Ac*, *60*(5), 803-814.

Otto-Bliesner, B. L., and E. C. Brady (2009), The sensitivity of the climate response to the magnitude and location of freshwater forcing: last glacial maximum experiments, *Quaternary Sci Rev*, *29*(1-2), 56-73.

Otto-Bliesner, B. L., J. M. Russell, P. U. Clark, Z. Y. Liu, J. T. Overpeck, B. Konecky, P. deMenocal, S. E. Nicholson, F. He, and Z. Y. Lu (2014), Coherent changes of southeastern equatorial and northern African rainfall during the last deglaciation, *Science*, *346*(6214), 1223-1227.

Paillard, D. L., L. Labeyrie, and P. Yiou (1996), Macintosh program performs time-series analysis, *Eos Trans. AGU*, *77*, 379.

Partin, J. W., K. M. Cobb, J. F. Adkins, B. Clark, and D. P. Fernandez (2007), Millennial-scale trends in west Pacific warm pool hydrology since the Last Glacial Maximum, *Nature*, *449*(7161), 452-U453.

Peltier, W. R., G. Vettoretti, and M. Stastna (2006), Atlantic meridional overturning and climate response to Arctic Ocean freshening, *Geophys Res Lett*, *33*(6).

Petersen, S. V., D. P. Schrag, and P. U. Clark (2013), A new mechanism for Dansgaard-Oeschger cycles, *Paleoceanography*, *28*(1).

Peterson, L.C., J.T. Overpeck, N.G. Kipp, J. Imbrie (1991), A high-resolution late Quaternary upwellinng record formt he anoxic Cariaco Basin, Venezuela, *Paleoceanography*, 6(1).

Peterson, L. C., G. H. Haug, K. A. Hughen, and U. Rohl (2000), Rapid changes in the hydrologic cycle of the Tropical Atlantic during the last Glacial, *Science*, 290, 1947-1951.

Petit, J. R., et al. (1999), Climate and atmospheric history of the last 420,000 years from the Vostok ice core, Antarctica, *Nature*, *399*, 429-436.

Philander, S. G. (1990), *El Nino, La Nina, and the Southern Oscillation* Academic Press San Diego.

Piotrowski, A.M., S.L. Goldstein, S.R. Hemming, R.G. Fairbanks (2005), Temporal relationships of carbon cycling and ocean circulation at glacial boundaries, *Science*, 307, 1933-1938.

Rahmstorf, S. (2002), Ocean circulation and climate during the past 120,000 years, *Nature*, 419(6903), 207-214.

Regenberg, M., S. Steph, D. Nurnberg, R. Tiedemann, and D. Garbe-Schonberg (2009), Calibrating Mg/Ca ratios of multiple planktonic foraminiferal species with delta O-18-calcification temperatures: Paleothermometry for the upper water column, *Earth Planet Sc Lett*, *278*(3-4), 324-336.

Regenberg, M., A. Regenberg, D. Garbe-Schonberg, and D. W. Lea (2014), Global dissolution effects on planktonic foraminiferal Mg/Ca ratios controlled by the calcite-saturation state of bottom waters, *Paleoceanography*, 27(3).

Rider, K. E. (2004), Shelf circulation patterns off Nigeria 181 pp, Texas A&M University

Ridley, D. A., C. L. Heald, and J. M. Prospero (2014), What controls the recent changes in African mineral dust aerosol across the Atlantic?, *Atmos. Chem. Phys.*, *14*, 5735-5747.

Ritz, S. P., T. F. Stocker, J. O. Grimalt, L. Menviel, and A. Timmermann (2013), Estimated strength of the Atlantic overturning circulation during the last deglaciation, *Nat Geosci*, 6(3), 208-212.

Rodriguez, S., E. Cuevas, J. M. Prospero, A. Alastuey, X. Querol, L. Lopez-Solano, M. I. Garcia, and S. Alonso-Perez (2015), Modulation of Saharan dust export by the North African dipole, *Atmos. Chem. Phys.*, *15*, 7471-7486.

Rosenthal, Y., E. A. Boyle, and N. Slowey (1997), Temperature control on the incorporation of magnesium, strontium, fluorine, and cadmium into benthic foraminiferal shells from Little Bahama Bank: Prospects for thermocline paleoceanography, *Geochim Cosmochim Ac*, 61(17), 3633-3643.

Rosenthal, Y., D. W. Oppo, and B. K. Linsley (2003), The amplitude and phasing of climate change during the last deglaciation in the Sulu Sea, western equatorial Pacific, *Geophys Res Lett*, 30(8).

Russell, A. D., B. Honisch, H. J. Spero, and D. W. Lea (2004), Effects of seawater carbonate ion concentration and temperature on shell U, Mg, and Sr in cultured planktonic foraminifera, *Geochim Cosmochim Ac*, 68(21), 4347-4361.

Sadekov, A., S. M. Eggins, P. De Deckker, U. Ninnemann, W. Kuhnt, and F. Bassinot (2009), Surface and subsurface seawater temperature reconstruction using Mg/Ca microanalysis of planktonic foraminifera Globigerinoides ruber, Globigerinoides sacculifer, and Pulleniatina obliquiloculata, *Paleoceanography*, 24.

Schefuß, E., S. Schouten, and R. R. Schneider (2005), Climatic controls on central African hydrology during the past 20,000 years, *Nature*, *437*(7061), 1003-1006.

Schmidt, M. W., and J. Lynch-Stieglitz (2011), Florida Straits deglacial temperature and salinity change: Implications for tropical hydrologic cycle variability during the Younger Dryas, *Paleoceanography*, 26.

Schmidt, M. W., and H. J. Spero (2011), Meridional shifts in the marine ITCZ and the tropical hydrologic cycle over the last three glacial cycles, *Paleoceanography*, *26*.

Schmidt, M. W., H. J. Spero, and D. W. Lea (2004), Links between salinity variation in the Caribbean and North Atlantic thermohaline circulation, *Nature*, 428, 160-163.

Schmidt, M. W., W. A. Weinlein, F. Marcantonio, and J. Lynch-Stieglitz (2012a), Solar forcing of Florida Straits surface salinity during the early Holocene, *Paleoceanography*, 27.

Schmidt, M. W., P. Chang, J. E. Hertzberg, T. R. Them, J. Link, and B. L. Otto-Bliesner (2012b), Impact of abrupt deglacial climate change on tropical Atlantic subsurface temperatures, *P Natl Acad Sci USA*, 109(36), 14348-14352.

Schmuker, B., and R. Schiebel (2002), Planktic foraminifers and hydrography of the eastern and northern Caribbean Sea, *Mar Micropaleontol*, *46*(3-4), 387-403.

Shanahan, T. M., N. P. McKay, K. A. Hughen, J. T. Overpeck, B. Otto-Bliesner, C. D. Heil, J. King, C. A. Scholz, and J. Peck (2015), The time-transgressive termination of the African Humid Period *Nat Geosci*.

Skinner, L. C., and H. Elderfield (2007), Rapid fluctuations in the deep North Atlantic heat budget during the last glacial period, *Paleoceanography*, 22(1).

Southon, J., A. L. Noronha, H. Cheng, R. L. Edwards, and Y. J. Wang (2012), A high-resolution record of atmospheric C-14 based on Hulu Cave speleothem H82, *Quaternary Sci Rev*, 33, 32-41.

Stager, J. C., D. B. Ryves, B. M. Chase, and F. S. R. Pausata (2011), Catastrophic Drought in the Afro-Asian Monsoon Region During Heinrich Event 1, *Science*, *331*(6022), 1299-1302.

Steph, S., M. Regenberg, R. Tiedemann, S. Mulitza, and D. Nurnberg (2009), Stable isotopes of planktonic foraminifera from tropical Atlantic/Caribbean core-tops: Implications for reconstructing upper ocean stratification, *Mar Micropaleontol*, 71(1-2), 1-19.

Stuiver, M., P. J. Reimer, and R. W. Reimer (2013), CALIB Radiocarbon Calibration Version 7.1.

Tarasov, L., and W. R. Peltier (2005), Arctic freshwater forcing of the Younger Dryas cold reversal, *Nature*, *435*(7042), 662-665.

Taylor, S. R., and S. M. Mclennan (1995), The Geochemical Evolution of the Continental-Crust, *Rev Geophys*, *33*(2), 241-265.

Tedesco, K., R. Thunell, Y. Astor, and F. Muller-Karger (2007), The oxygen isotope composition of planktonic foraminifera from the Cariaco Basin, Venezuela: Seasonal and interannual variations, *Mar Micropaleontol*, *62*(3), 180-193.

Teller, J. T., D. W. Leverington, and J. D. Mann (2002), Freshwater outbursts to the oceans from glacial Lake Agassiz and their role in climate change during the last deglaciation, *Quaternary Sci Rev*, *21*(8-9), 879-887.

Thornalley, D. J. R., I. N. McCave, and H. Elderfield (2010), Freshwater input and abrupt deglacial climate change in the North Atlantic, *Paleoceanography*, *25*.

Thorncroft, C. D., N. Hanh, C. D. Zhang, and P. Peyrille (2011), Annual cycle of the West African monsoon: regional circulations and associated water vapour transport, *Q J Roy Meteor Soc*, *137*(654), 129-147.

Tierney, J. E., J. E. Smerdon, K. J. Anchukaitis, and R. Seager (2013), Multidecadal variability in East African hydroclimate controlled by the Indian Ocean, *Nature*, *493*(7432), 389-392.

Tierney, J. E., S. C. Lewis, B. I. Cook, A. N. LeGrande, and G. A. Schmidt (2011), Model, proxy and isotopic perspectives on the East African Humid Period, *Earth Planet Sc Lett*, *307*(1-2), 103-112.

Timmermann, A., H. Gildor, M. Schulz, and E. Tziperman (2003), Coherent resonant millennial-scale climate oscillations triggered by massive meltwater pulses, *J Climate*, 16(15), 2569-2585.

Tjallingii, R., M. Claussen, J. B. W. Stuut, J. Fohlmeister, A. Jahn, T. Bickert, F. Lamy, and U. Rohl (2008), Coherent high- and low-latitude control of the northwest African hydrological balance, *Nat Geosci*, *1*(10), 670-675.

Vautravers, M. J., N. J. Shackleton, C. Lopez-Martinez, and J. O. Grimalt (2004), Gulf Stream variability during marine isotope stage 3*, Paleoceanography*, 19(2), PA2011, doi:2010.1029/2003PA000966.

Waelbroeck, C., L. D. Labeyrie, E. Michel, J. C. Duplessy, J. F. McManus, K. Lambeck, E. Balbon, and M. Labracherie (2002), Sea-level and deep water temperature changes derived from benthic foraminifera isotopic records, *Quaternary Sci Rev*, 21, 295-305.

Wan, X. Q., P. Chang, R. Saravanan, R. Zhang, and M. W. Schmidt (2009), On the interpretation of Caribbean paleo-temperature reconstructions during the Younger Dryas, *Geophys Res Lett*, 36.

Wang, Y.J., H. Cheng, R.L. Edwards, Z.S. An, J.Y. Wu, C.-C. Shen, J.A. Dorale (2001), A high-resolution absolute-dated late Pleistocene monsoon record from Hulu Cave, China, *Science,* 394, 2345-2348.

Wang, X. F., A. S. Auler, R. L. Edwards, H. Cheng, P. S. Cristalli, P. L. Smart, D. A. Richards, and C. C. Shen (2004), Wet periods in northeastern Brazil over the past 210 kyr linked to distant climate anomalies, *Nature*, *432*(7018), 740-743.

Washington, R., C. Bouet, G. Cautenet, E. Mackenzie, I. Ashpole, S. Engelstaedter, G. Lizcano, G. M. Henderson, K. Schepanski, and I. Tegen (2009), Dust as a tipping element: The Bodele Depression, Chad, *P Natl Acad Sci USA*, *106*(49), 20564-20571.

Weijers, J. W. H., E. Schefuss, S. Schouten, and J. S. S. Damste (2007), Coupled thermal and hydrological evolution of tropical Africa over the last deglaciation, *Science*, *315*(5819), 1701-1704.

Weldeab, S., D. W. Lea, R. R. Schneider, and N. Andersen (2007), Centennial scale climate instabilities in a wet early Holocene West African monsoon, *Geophys Res Lett,* 34(24).

Weldeab, S., D. W. Lea, R. R. Schneider, and N. Andersen (2007), 155,000 years of West African monsoon and ocean thermal evolution, *Science*, *316*(5829), 1303-1307.

Zhang (2007), Anticorrelated multidecadal variations between surface and subsurface tropical North Atlantic, *Geophys Res Lett*, 34(12).

Zhang, X., M. Prange. U. Merkel, and H. Schulz (2015), Spatial fingerprint and magnitude of changes in the Atlantic meridional overturning circulation during Marine Isotope Stage 3, *Geophys. Res. Lett*., 42, 1903-1911, doi:10.1002/2014GL063003.